Master's thesis

NTNU
Norwegian University of Science and Technology
Faculty of Information Technology and Electrical Engineering
Department of Electric Power Engineering

Ingvar Hinderaker Sunde

Design and Optimisation of Electrical Collectors for a Multi-Rotor Wind Turbine System

Master's thesis in Energy and Environmental Engineering
Supervisor: Olimpo Anaya-Lara
June 2019

NTNU
Kunnskap for en bedre verden

Ingvar Hinderaker Sunde

Design and Optimisation of Electrical Collectors for a Multi-Rotor Wind Turbine System

Master's thesis in Energy and Environmental Engineering
Supervisor: Olimpo Anaya-Lara
June 2019

Norwegian University of Science and Technology
Faculty of Information Technology and Electrical Engineering
Department of Electric Power Engineering

NTNU
Norwegian University of
Science and Technology

Preface

This master's thesis presents the work conducted during my master's course *Energy and Environmental Engineering* at the Department of Electric Power Engineering, Norwegian University of Science and Technology (NTNU). This thesis is a continuation of the specialisation project from the fall of 2018, titled *"Power Losses in Electrical Topologies for a Multi-Rotor Wind Turbine System"*, which also was the basis for a paper with the same name accepted for publication in the *Journal of Physics: Conference Series*.

This work has been performed in order to fill a knowledge gap in electrical collectors of the Multi-Rotor Wind Turbine System, which was extensively investigated in the Innwind.eu-project, Work Package 1 - Conceptual Design. To this aim, a multi-objective optimisation was found necessary to be performed.

Preliminary work on electrical collectors for the multi-rotor system has already started by a research group from Strathclyde University in Glasgow, Scotland, which has been used as a starting point and further developed in this master's project. Since a detailed analysis of the electrical design was still to be addressed, this research focused on that point within a reasonable scope given time limitation during an M.Sc. project. However, exciting results and new knowledge were generated, which enhance the understanding of this part of the technology and can be used for further research.

Trondheim, 06.06.2019

Ingvar Hinderaker Sunde

Acknowledgements

I would like to thank my supervisor, Prof. Olimpo Anaya-Lara for giving me the opportunity to work on this exciting topic, as well as research scientist Dr. Raymundo E. Torres-Olguin from SINTEF ER, who has given me input on almost daily basis. They have supported me during this last year and motivated me to complete this exciting work. In addition, they motivated and helped me to get a published paper related to my work. It has been a delight working with you.

In addition, I would like to thank Dr. René Alexander Barrera-Cárdenas from SINTEF ER, who helped me adapt some of his prior work to my study, which was essential for the study performed. It has been a big contribution to this study.

I would also like to thank the people involved in the *Energy and Environmental Engineering* study program, an especially to my class for a fantastic atmosphere during these five years. Besides, I would thank the people I have shared the office F312 with the last year. It has been a pleasure.

Abstract

The extensive use and fast development in wind power also introduce challenges as the wind turbines keep increasing in size and power rating. The high amount of material required to realise the massive turbine blades and other components makes it hard to keep reducing the Levelised Cost of Energy (LCOE). As a result, new and innovative designs are studied to find other methods to realise high energy density wind turbines.

As a way of realising a large producing unit with material savings, the old concept of multi-rotor wind turbines has been relaunched recently. In a multi-rotor system, several small rotors are connected with small spacing, which in total sweep a large area in order to produce a high amount of power. Since smaller rotors are used, this drastically reduces the material required to develop the system. Promising aerodynamic studies have been performed for the concept. However, thorough studies of the electrical design of the system are still lacking. This work, therefore, concentrates on researching this aspect and proposes different electrical design configurations for the multi-rotor system. The proposed configurations are compared under different scenarios. The proposed configurations are all cluster connections and have been identified in this work as AC cluster, DC cluster and hybrid cluster. It is important to emphasise that these configurations relate to the way in which the power output of the small rotors is collected.

It is noticed from prior work on this topic that to study only power losses is insufficient to compare different design options. In this study, a multi-objective optimisation method is used to obtain several key performance indicators, such as efficiency η, power density ρ, and power-to-mass ratio γ, to compare and to choose the optimal design for a multi-rotor system. Key indicator parameters are defined and studied extensively for the different configurations, as is shown in the thesis work. Moreover, Pareto analysis is performed to locate potential design points and reasonable trade-offs between several parameters and objectives that can be contradictory, such as maximising efficiency and minimising volume and mass.

Extensive analyses have also been performed to establish analytic expressions for the power losses, volume and mass of the components included in this study, as these are needed to evaluate η, ρ, and γ. The components considered include the power electronics, that is, the switch valves, DC-link, and phase reactors.

Various cases have been defined in order to perform solid comparisons. The two first cases use three turbines per cluster, with machines rated at 444 kW, but with changed modulation method. Further, case 3 and 4 study the behaviour of the configurations when the cluster size and the machine size are increased. Finally, case 5 studies a DC series-connection of wind turbines, different from a parallel-

connection which has been one of the configurations in the previous cases.

The results achieved have shown significant differences with different modulation methods, so this may influence the overall design. Also, the increase in the cluster size and machine size has been found in this work to be beneficial. However, this also provides challenges regarding control and can reduce the potential gain in aerodynamic behaviour as well as reduced material.

Overall, the DC and hybrid cluster connections perform the best. The hybrid configuration has the highest power density and the power-to-mass ratio at machine power of 444 kW but requires operation at non-optimum speed. The parallel-connected DC cluster performs close to the hybrid cluster, and its topology is worth investigating more. Besides, the series-connected DC configuration, reducing the need for transformers, was promising. However, DC collector grids evidently need more research.

Nonetheless, to make the system compete with conventional turbines, the substantial reduction of components in the DC and hybrid clusters may be necessary. The results obtained help discussing potential advantages for each configuration, but further research, including the control, must be performed to choose a proper design.

Samandrag

Den raske utviklinga i vindenergien skapar òg utfordingar medan storleiken og effekten på vindturbinane aukar. Mengda materialar som ein treng for å produsere lange blad og andre viktige komponentar gjer det vanskeleg å redusere den gjennomsnittlege energikostnaden (LCOE). Som ei følgje av det, blir det no studert nye og innovative design for å finne andre måtar å produsere vinturbinar med høg energitettleik.

For å realisere ei stor, produserande eining, saman med materialinnsparingar, er det gamle konseptet om fleirrotor vindturbinar (multi-rotor wind turbine) blitt relansert nyleg. I eit fleirrotorsystem er fleire små rotorar kopla saman med liten avstand, som til saman dekker eit stort areal og som gjer det mogleg å produsere ei stor mengd kraft. Sidan små rotorar blir brukt, reduserer dette kraftig mengda materialar som ein treng. Lovande aerodynamiske analysar og resultat har dette konseptet gitt oss. Likevel er det førebels ikkje blitt gjort omfattande studiar av det elektriske designet til dette systemet. Dette studiet konsentrerer seg derfor om dette aspektet og foreslår forskjellege elektriske designkonfigurasjonar for fleirrotorsystemet. Desse blir samanlikna for eitt utval av casestudiar. Dei foreslåtte konfigurasjonane er alle klyngekopla og svært forskjellige frå kvarandre. Dei er i denne oppgåva kalla for AC klynge (AC cluster), DC klynge (DC cluster) samt hybrid klynge (hybrid cluster), etter korleis krafta i dei respektive konfigurasjonane er samla.

Frå tidlegare arbeid veit ein at effekttap som den einaste parameteren for å samanlikne ulike konfigurasjonar ikkje er tilstrekkeleg. Derfor bruker dette studiet ein fleir-objektiv optimaliseringsmetode for å få fleire indikatorar, som verknadsgraden η, krafttettleik ρ og kraft-til-masse rate γ som kan samanliknast for å kunne utvikle eit godt design som kan brukast i eit fleirrotorsystem. Nøkkelparametrar blir definerte og desse er nøye studert for dei forskjellege konfigurasjonane som dette arbeidet viser. For å kunne gjere dette, nyttast Paretoanalysar for å lokalisere potensielle designpunkt og gjere meiningsfulle avvegingar mellom parametrar og mål som kan vere motstridande. Dette kan vere å maksimere verknadsgrad og samstundes minimere volum og masse.

Vidare blir det gjort omfattande analysar for å etablere analytiske uttrykk for effekttap, volum og masse av komponentane som inngår i dette studiet, då dette trengs for å evaluere η, γ og ρ. Komponentar som blir studerte er avgrensa til å inkludere kraftelektronikk, som vil seie svitsjeventilar (switch valves), DC-link kondensatorar og fasereaktorar.

Vidare er forskjellige casar lagt fram for å kunne gjere solide samanlikningar. Dei to fyrste casane har tre turbinar per klynge, med maskinar på 444 kW. Det

som skil, er moduleringsmetoden, då denne er endra frå case 1 til case 2. Videre studerer case 3 og 4 oppførselen til konfigurasjonane når først klyngestorleiken, deretter maskinstørrelse blir auka. Til slutt, i case 5, er ei DC seriekopling av vindturbinane studert, forskjellig frå parallellkoplingane som er studert tidlegare i oppgåva.

Resultata viser ein stor skilnad når moduleringsmetoda blir endra, så dette vil påverkar designet. I tillegg har det å auke både klyngestorleiken og maskinstorleiken i dette arbeidet vist seg å vere føremålstenleg. Trass i dette, vil det å auke storleiken skape utfordringar når det kjem til kontroll. Større maskinar kan også redusere den aerodynamiske vinsten systemet har vist, samt auke mengda material som ein treng, samanlikna med mindre maskinar.

Gjennom heile analysen har DC- og hybrid-klynga prestert best. Hybridkonfigurasjonen har høgast krafttettleik og kraft-til-masse rate ved maskineffekt på 444 kW, men denne treng å opererast på ikkje-optimal hastigheit. Den parallellkopla DC-klynga har prestert liknande som hybridklynge og er også verdt å forske vidare på. I tillegg var seriekoplinga i DC lovande, då den også reduserer behovet for transformatorar. Men ei realisering av DC-nett trengs å bli forska meir på.

Uansett, for å gjere fleirrotorsystemet mogleg å konkurrere med konvensjonelle vindturbinar må det til store reduksjonar av komponentar, som i DC- og hybridklynga. Resultata som er fått gjer det mogleg å diskutere potensielle fordelar med dei forskjellege konfigurasjonane. Men ei utviding av systemet, inkludert eit kontrollsystem, må gjerast for å kunne velje eit design på eit godt nok grunnlag.

Table of Contents

List of Figures

List of Tables

Acronyms

AC Alternating Current

CFD Computational Fluid Dynamics

DC Direct Current

DFIG Doubly Fed Induction Generator

DPWM1 Discontinuous Pulse Width Modulation

FID Final Investment Decisions

HVAC High Voltage Alternating Current

HVDC High Voltage Direct Current

IGBT Insulated-gate bipolar transistor

LCOE Levelised Cost of Energy

PMSG Permanent Magnet Synchronous Generator

RMS Root Mean Square

SCIG Squirrel Cage Induction Generator

SFTM Symmetrical Flat-Top Modulation

SPWM Sinusoidal Pulse Width Modulation

SVPWM Space-Vector Pulse Width Modulation

THD Total Harmonic Distortion

TSO Transmission System Operator

VSC Voltage Source Converter

VSI Voltage Source Inverter

VSR Voltage Source Rectifier

WFC Wind Farm Control

WRIG Wound Rotor Induction Generator

Chapter 1

Introduction

The Multi-Rotor Wind Turbine concept is gaining attention both in academia and among manufacturers. Concerning this, an extensive investigation of the electrical design of the system is found necessary and is performed in this work.

This chapter provides the background and motivation for the multi-rotor system and why it is researched. The objective and scope of the thesis are presented along with the methodology used, a list of publications from the author and an outline of the thesis.

1.1 Background

Wind power is improving its share in the European power system, and after experiencing a record year in new installed capacity in 2017 of 16.8 GW [1], the number was in 2018 reduced to 11.7 GW [2]. Even though this is the lowest amount since 2011, and mainly caused by regulatory changes in the EU affecting mainly onshore wind, the cumulative installed capacity is at its ever highest, at 189.2 GW. Besides, installed offshore wind power was at its third-ever highest in Europe.

The increase in cumulative installed wind power capacity, together with lower electricity demand, made wind power account for 14 % of EU's electricity demand. The increase is expected to continue, resulting in wind power capacity exceeding 200 GW by 2020 [3]. Despite decreased new installed capacity in 2018, it was still a record year for new Final Investment Decisions (FID) in future capacity [3]. Thus, wind power is the fastest growing energy source and will most likely pass the installed power from gas in 2019.

Consequently, with the increase in capacity both in Europe and worldwide, there is also an escalation in wind turbine size. The average installed onshore turbines in 2018 had a power of 2.7 MW [3]. Offshore, the European average wind turbine

size of 2018 was 6.8 MW, a 15 % increase from the year before. The world's largest turbine was installed in the UK, with its 8.8 MW and rotor diameter of 164m. Together with the ongoing reduction in the Levelised Cost of Energy (LCOE), the size of the turbines is expected to increase, and GE has announced their Haliade-X 12 MW turbine, with a rotor diameter of 220m [4].

However, with the increasing size of wind turbines, challenges arise. The social acceptance of sizeable onshore wind turbines, due to visibility and noise is one aspect, but also the technical challenges related to the amount of material required and the structures employed [5]. From the older generation of turbine blades, mostly consisting of steel, the turbine blades of today mostly consist of glass fibre and variable quantities of carbon fibre, which is more expensive. For longer blades, the share of carbon fibre required increases drastically, as this material offers higher stiffness, which is needed for longer blades to maintain stability [5].

In addition, whereas the energy capture increase with the blade length squared, the weight of the blades scale with the cube of the blade length [6]. Thus, this development provides challenges both in terms of costs, mass and size, and the increasing demand for rare earth materials [7]. Therefore, new solutions are investigated to maintain the reduction in LCOE, which is necessary to expand the use of wind power worldwide.

As an alternative to the pursuit of developing larger and larger single rotor turbines and as a possibility to develop wind turbine installations with a power of 20 MW or more, the concept of a Multi-Rotor Wind Turbine System was commenced by P. Jamieson [8, 9]. The concept has been existing for a long time but has not been getting much attention due to the fast development in turbine blade technology. The idea behind the multi-rotor system is that several small rotors, with short spacing in between, in total sweep a large area, making a generation of 20 MW or more possible using just one single installation. Due to the short blade sizes, this design saves a lot of material [9]. Moreover, the standardisation of smaller components makes the system easier to scale up.

A large study was performed in conjunction with the European project called Innwind [8], along with Vestas, who built a 4-rotor test demonstrator in Denmark for research purposes [10], both showing a possibility of increased aerodynamic performance compared to single-rotors of the same power. In [8], a solution using 45 rotors, rated at 444 kW and with a rotor diameter of 40.55m is proposed. However, as the concept is still in an early phase, and not much literature is published so far, there is room for exploring different solutions. The main focus is an installation capable of producing 20 MW, which is easily scalable, offers significant savings in material requirements, and is cost-effective compared to conventional wind turbines in the long run.

1.2 Motivation for this research

The aerodynamic behaviour of the multi-rotor system has been broadly investigated [8, 10, 11], omitting a comprehensive study of the electrical design of the system. In fact, there is no significant analysis of the electrical design of the multi-rotor system to this date. There are inquiries related to the electrical design, the collection grid, and to the possibilities of saving expensive components such as converters, transformers, and cables by letting several turbines share essential components. Investigating possible electrical solutions to realise a system with excellent performance while limiting the required volume and mass of the system is the main focus of this study.

Related work on the electrical design of the multi-rotor system [12, 13], has not been so comprehensive and has mainly been focusing on studying the power losses in different solutions. However, to propose realistic designs, it is necessary to investigate more parameters simultaneously. Therefore, a multi-objective optimisation method is employed to find the right trade-offs between important parameters which also may contradict each other. Doing this provides a good starting point to justify a choice of a configuration for the multi-rotor concept.

As the electrical design and connections of the turbines in a multi-rotor system is an important aspect, this study provides guidelines and propose concepts which should be followed up in future work. Since electrical collectors for multi-rotor systems has not been studied significantly up to now, there is some freedom on how to initiate the investigation. Reasonable assumptions must be taken, and requirements along with limitations of the system must be chosen appropriately. Hopefully, this work lays the ground for further studies in the electrical perspective of the multi-rotor system.

1.3 Objectives

The main objective of this thesis is to use a multi-objective optimisation method to provide recommendations for the design of the collector system for a Multi-Rotor Wind Turbine System. Various design alternatives were investigated and proposed in [12], which served as a groundwork for this master thesis. These configurations are presented in Figure 1.1 and are investigated more profoundly to provide some design guidelines. To easier accomplish this, the work is divided into smaller objectives, which are:

- Identify important aspects which yield for the multi-rotor system and need to be taken into consideration when designing the collector system.

- Define a set of relevant parameters to perform sensible comparisons between the different configurations. Also, choose reasonable ways to compare the different configuration when the parameters are defined.
- Develop and implement generic calculations to obtain the desired parameters which easily can be adjusted to changes in the configurations.
- Study the configuration for a diverse set of cases, to get a solid overview of the relationships and behaviour of the configurations.
- Discuss other important aspects relevant to the multi-rotor system, which are not captured by the defined comparison parameters.

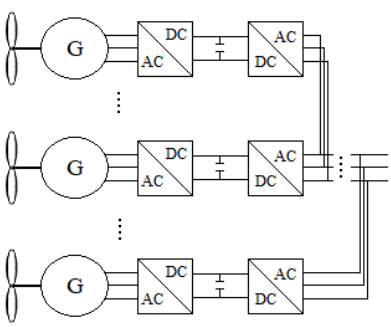

(a) AC cluster

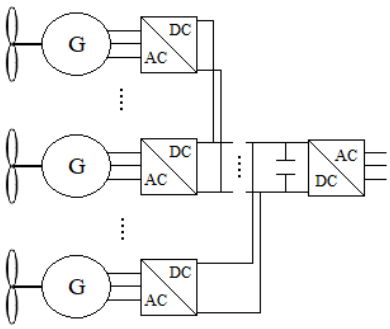

(b) DC cluster

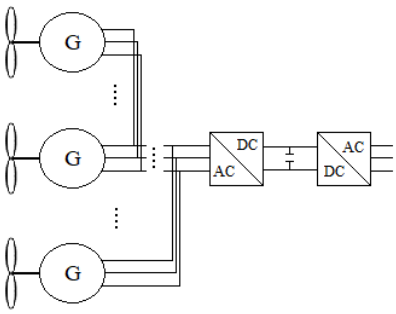

(c) Hybrid cluster

Figure 1.1: Proposed cluster topologies.

1.4 Scope

To make the masters project feasible, the scope of the study was suitably narrowed. The focus of the study is on the power electronics components used for constructing a cluster connection of wind turbines. For simplicity, only the components of one individual cluster are studied, assuming that other clusters are equal. Consequently, the components studied quantitatively in this work are the voltage source converters (VSC), including the switch valve devices, the cooling system, the DC capacitors for the DC-link as well as the phase reactors.

The machine dynamics are not studied, as the machine is just set to provide the power at which the system is rated. Also, the connection between clusters is not treated in detail. Still, aspects which are excluded from the quantitative analysis, such as requirements for the machines, filters and the control of the system, are discussed in, and added to, the future work proposals of this study.

Other limitations and assumptions relevant to the calculations and optimisation performed, are given in Chapter 5. This includes both general assumptions and specific assumptions for each case.

1.5 Methodology

This work has the following steps:

- Review of the state of the art. This includes available literature on the multi-rotor system, as well as on collector configurations.
- Define a different set of scenarios and cases. This should enable comparison of different configuration varying operating conditions.
- Select key performance indicators which are relevant for the system studied. Study in detail how to analytically calculate these indicators.
- Implement the analytic expressions to a numerical simulator (M-file scripts by MATLAB) which easily can be changed according to the design criteria.
- Debug the calculations implemented. Confirm valid operation and that the calculated results are realistic.
- Perform the analysis of the different cases studied. This is done by displaying the different performance indicators and making Pareto analyses of the obtained results.
- Draw concluding remarks based on the obtained results. The topologies are discussed and potential advantages and disadvantages are pointed out.

1.6 List of publications

Journal papers

I. H. Sunde, R.E. Torres-Olguin, O. Anaya-Lara, "Power Losses in Electrical Topologies for a Multi-Rotor Wind Turbine System", *Journal of Physics: Conference Series*, 2019. Appendix D.1. Reference [12].

Poster presentations

I. H. Sunde, R.E. Torres-Olguin, O. Anaya-Lara, "Electrical Collector Topologies for Multi-Rotor Wind Turbine Systems", poster presentation in *EERA DeepWind'2019-16th Deep Sea Offshore Wind R&D conference*, Trondheim, Norway 2019. Appendix D.2. Reference [14].

1.7 Outline of the Thesis

The thesis is outlined as follows:

Chapter 2 describes the multi-rotor system. The background for why it is gaining attention, as well as aerodynamics analysis, are laid out before the electrical system design criteria and options are presented.
Chapter 3 focuses on the parameters used in this thesis for optimisation and presents ways to compare these to obtain good design options.
Chapter 4 presents the theory needed to develop the codes used in this work. All relevant components are put at disposal.
Chapter 5 presents the different cases which are used in this study. They are presented one by one, followed by a comparison.
Chapter 6 contains concluding remarks of the study performed and presents topics which are excluded from the scope of this study on a qualitative level. These should be addressed more in detail in future work.

Chapter 2

Multi-Rotor Wind Turbine System

The multi-rotor concept is, as a matter of fact, an old concept that recently has gained new attention. The concept is considerably explained in a technical report from the European project Innwind from 2015 [8], as an approach to develop wind turbines capable of delivering 20 MW or more. The report includes the structural design and aerodynamic calculations and simulations but lacks a comprehensive study of the electrical design, which also needs a thorough examination.

Right after the publication of the report, the wind energy company Vestas installed a 4-rotor wind turbine in the Risø Test site in Denmark [10]. This turbine was constructed for research purposes and consisted of four induction generators of the type V29-225kW. The main focus was on the aerodynamic behaviour, loads, and the wake effect. This turbine has now been decommissioned, and preliminary results have been published, showing promising potential.

In this chapter, the background and motivation behind developing the multi-rotor concept are presented. Further, a review of the studied aerodynamics is performed, where both the simulations from the Innwind report and the test results from Vestas are summarised. Moreover, aspects of electrical design are introduced. The requirements needed for the application are mentioned, possible electrical configurations are presented, as well as arguments for the chosen configurations which are further studied.

2.1 Background

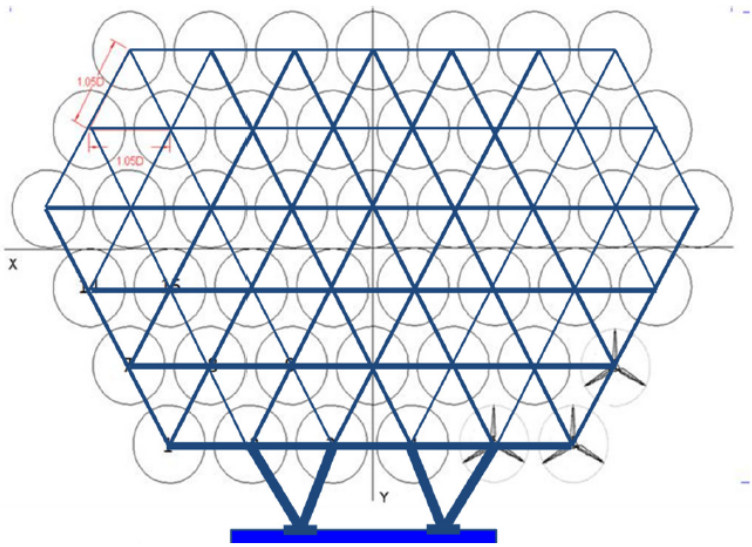

Figure 2.1: A 45-Rotor wind turbine system proposed in the Innwind.eu project [8].

The idea of a multi-rotor wind turbine is quite old and can be dated as far back as at least the start of the 20th century, with a 2-rotor windmill in Denmark [15]. Later, in the 1930s, the German wind energy pioneer Hermann Honnef proposed a 3-rotor wind turbine with the motivation of building larger wind turbines, eliminating the concerns about increased weight due to larger blades constructed in steel [8]. As steel was the only material used for developing the turbine blades, this made it possible to realise large producing units with reduced mass. However, with the development of the glass composite technology and, consequently, the modern blade technology, it became feasible to develop large single-rotor turbines [9], and the concept of multi-rotors was more or less put to the side for an extended period.

Later on, in the 1970s, another wind power pioneer, Bill Heronemus, became aware having standardised rotor- and drive train components could be beneficial and that large systems could be developed due to the scalability of the standardised components [8]. This idea was also adopted by Peter Jamieson, who highlighted the potential of massive material savings, which also results in significant cost reductions, making the multi-rotor system an advantageous alternative as a high-power wind turbine design.

Jamieson presented his ideas regarding the scaling principle and potential mate-

rial and cost savings [6] and proposed a potential design of a 45-rotor wind turbine [8]. This system is illustrated in Figure 2.1 and is one alternative to reach 20 MW or more by one single unit. The main idea is that the smaller rotors in total sweep the same area as a single rotor turbine producing 20 MW would, but with reduced material. The standardisation of the parts needed, prevent the development of new and larger blades and drive trains. Besides, several rotors can share critical components, to a more significant extent than what is feasible in any other design of wind turbines or wind farms.

Some of the key advantages of the system mentioned above are discussed in [9] and [16], such as reduced weight of blades and nacelle, which again may reduce the weight of the tower. According to [6], the ratio of the needed material, and thus the costs, for a system of n rotors compared with a single rotor of equivalent capacity, is given by $1/\sqrt{n}$. The benefits of having smaller and standardised components are the reduced complexity of installation and maintenance, as well as more accessible transportation of smaller components. Moreover, the system should be designed in a way that, in the case of a single rotor or component failure, the total produced power is not heavily influenced.

A challenge, however, is the complexity of the system. The high number of needed components, consequently means an increased possibility of failure, as more components potentially may fail. Advanced switchgear may be required to ensure safe operation and solutions to the advanced control system needed must be provided. The effects of having the rotors that close to each other under both normal and abnormal circumstances need to be studied in detail.

The multi-rotor wind turbine presented in the Innwind-project consists of 45 rotors, each rated at 444 kW, which results in the total power of 20 MW. The lattice structure which is illustrated in Figure 2.1, is claimed to be the most efficient type of support structure when minimising the mass of materials is the objective, and is a dominating solution [8]. The structure is intended to be applied offshore. Therefore, a floating structure has been inspected, as this enables installation in deep water, where the wind velocity might be higher and more stable.

2.2 Aerodynamics

The aerodynamic performance of the multi-rotor concept was studied in detail in correlation with the Innwind-project [8, 11]. In [11], a case consisting of a 7-rotor system was studied, while in [8] also a 45-rotor system was added and studied.

The 7-rotor and 45-rotor cases compared the performance of a 7-and 45-rotor turbine to an equivalent single-rotor turbine. The blades had a diameter D of 40.55 m, a power each of 444kW and a hub height (height of the central rotor)

of 227.06 m. The spacing between the rotors was set to $1.05D$. These turbines were compared with the single rotor multiplied by 7 and 45 respectively, having the same diameter and hub height, the latter being higher than the regular 1D above ground level.

Two simulation methods were used to obtain the results. These were a CFD actuator disk which gave a prediction of the mean flow field, and a vortex method used to assess the dynamic implications of the system.

The results showed an increase in thrust and power, meaning that the blocking of the flow is not negatively affecting the performance. Nevertheless, an increase in output power of 2.5-3 % was found for the 7-rotor case and at the same time, a thrust increase of 1.5 %. The 45-rotor case showed an increase of 8 % in both power and thrust compared to the single rotor. The increase in thrust may be overcome by pitch control.

After Vestas decommissioned their 4-rotor wind turbine (4R-V29), they reviled some of their field measurements and compared them with the numerical simulations previously performed [10]. The 4R-V29 turbine used four 225 kW rotors, with blade diameters of 29.2 m and an average hub height of 44.27 m as well as nearly a 1.05D spacing, as used in [8, 11]. A picture of the installed 4-rotor turbine is seen in Figure 2.2.

Figure 2.2: Vestas 4-rotor demonstrator at Risø Test Site [10].

The key findings published in [10] were an increased thrust force compared to a single rotor. Besides, due to the interactions of rotors, the power was increased as predicted by the simulations. The increase in power performance below rated power was at around 1.8 %. Furthermore, the results showed a wake recovery distance for the 4R-V29 turbine to be $1.03 - 1.44D$ shorter than for an equivalent single rotor turbine with diameter D. In addition, the wake turbulence was smaller for the multi-rotor turbine than for an equivalent single-rotor turbine. Smaller wake turbulence is beneficial when designing a wind farm of multi-rotor wind turbines, in the sense that the turbine can be placed more compact, making the power per area of a wind farm higher than for single-rotor turbine wind farms.

2.3 Electrical design and proposed configurations

The Innwind-project[8] includes a limited amount regarding the electrical design and the collector system of the multi-rotor system. A focus in the project was to investigate the impacts of connecting the turbines electrically in clusters, and also to design the system in a way that a single fault does not influence an immensely large part of the system. The method of clustering is a trade-off between the control abilities, the efficiency, and the costs of the system. In [8] it is assumed that a back-to-back converter is employed for each turbine. This assumption is not used in this study.

A critical attention is that expensive and large components can be shared by several turbines. What can be shared, includes, for instance, transformers, DC-links, protection equipment, phase reactors, filters, and also converters. A way of reducing the number of several essential components is to connect several units in clusters, as illustrated in Figure 2.3. Cluster connections offer possibilities to share critical components; for instance, one cluster can share a single transformer, instead of individual transformers in each wind turbine nacelle, which is the standard in most wind farms.

After the Innwind report from 2015 [8], [13] and [17] have been published, discussing the electrical design of the collector system of a multi-rotor wind turbine. Both of them present two different drive trains, one in AC and one in DC, where the AC drive train interfaces a back-to-back converter, and the DC drive train interfaces just one converter.

In [17], different options of collector systems in AC and DC care presented. For AC, a back-to-back converter is connected to the machine, and connection options such as radial, ringed, and star connections are outlined. For DC, only one converter is directly connected to the machine, and parallel, series, and a combined series-parallel connection are considered.

In [13], a focus is on the reliability of the system and on the investigation of the difference in connecting every turbine directly to the central hub or by clustering several turbines, both in AC and DC, using parallel connections. At simplified systems, power losses and the costs are estimated, favouring a cluster way of connecting as efficient, both in terms of power losses and costs.

When designing the electrical system for the multi-rotor concept, there are many requirements and considerations to take into account. The system consists of 45 rotors, so in the case of failure in one unit, it is undesirable that a big part of the system needs to be disconnected. To fulfil this desire, advanced switchgear is probably required. Moreover, it is desired to reduce the number of components needed. As the turbine is meant offshore, and one of the significant advantages of the multi-rotor system is reduced material, it is essential that the system is optimised when it comes to power density.

Besides, the needed amount of electrical interconnections within the turbine is high. However, as the output power is as high as it is, and the wake recovery distance as small as stated in [10], the need for high-rated subsea cables in a potential multi-rotor wind farm is reduced, making installation and maintenance easier.

To benefit from the potential savings in sharing components, cluster connections are proposed in all the configurations studied in this work. In [8], configurations employing a different number of clusters and different numbers of wind turbines within one cluster are experimented with. Clusters consisting of a varying number of wind turbines are also investigated in this work. For the sake of simplicity, the clusters are assumed to be identical, and with the same amount of turbines per clusters in all configuration. Different ways of clustering the turbines can be seen in Figure 2.3.

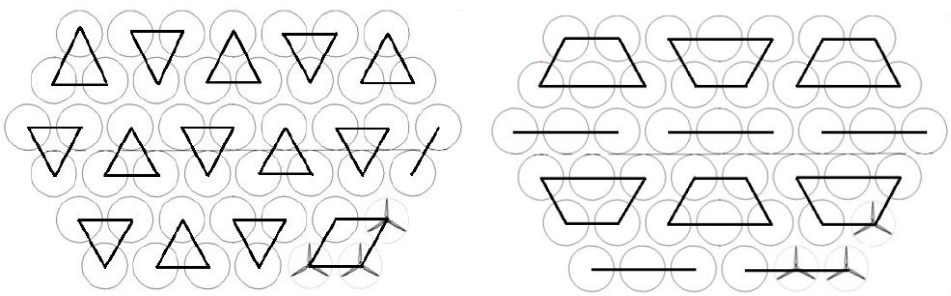

(a) Clusters of 2,3 and 4 turbines (b) Clusters of 3 and 5 turbines

Figure 2.3: Different clustering techniques[8].

The first and most known configuration from modern literature is a configura-

tion with one individual back-to-back converter for every turbine. This way allows good control possibilities with the well proven AC and back-to-back converter topology. The clusters are connected, and the voltage is transformed to the desired level before transmission. Thus, several turbines share the same transformer as well as protective gear. This topology is the normal one in modern, direct drive fully-rated converter wind turbines, and is a dominating technology in current wind projects worldwide [18].

The desired number of turbines in one cluster is connected in AC. Each cluster then interfaces an AC transformer, increasing the voltage level. Then, the number of clusters are connected, also in AC, and the voltage is increased again before transmission, either in HVAC or HVDC. However, the connection of clusters with each other is outside the scope of this study, which is limited to investigate one such cluster. This configuration will, due to its topology, be called the AC cluster and can be seen in Figure 1.1a.

The further connection with other clusters as far as the transmission is shown in Figure 2.4a. In the figure, each turbine and belonging power electronics are represented by a cross (X), before the connection with the other turbines in the same cluster is shown. After a transformer, all the clusters are connected.

In the second configuration, the individual inverters are removed, compared to the AC cluster. Each generator interfaces a rectifier, and all rectifiers in one cluster are connected to one shared DC-link and the inverter. This inverter needs to have a higher rating than the inverters in the AC cluster. A DC configuration, like this, is claimed to have multiple advantages, such as being more cost-efficient [19]. Besides, DC cables are smaller in size and weight, and reactive compensation is not needed. However, DC collection grids are not as well studied or proven as AC collection grids, which raises challenges. Protection gear for DC is needed, which increases the cost and complexity of the system [13]. Meanwhile, instead of using ordinary AC transformers for increasing the voltage, DC-DC converters with medium-frequency transformers can be employed [20]. The use of medium-frequency transformers reduces weight and volume, and this concept has gained interest both in industry and academia due to advancements in semiconductor technology, magnetic material, and control methods [21].

After the voltage is increased, the clusters can be connected before another voltage increase and transmission. However, this is not studied in this work. The scope is limited to investigate the connection of the turbines in one cluster, including the shared converter. Thus, components specific for this topology, such as DC-DC converters and DC protection gears are not studied in this work. This configuration is further referred to as the DC cluster and is seen in Figure 1.1b.

The further collection grid is shown in Figure 2.4b. The X in this figure represents one turbine and the belonging rectifier. All turbines in one cluster are

connected to a DC bus before a DC-DC converter steps up the voltage and all clusters are connected at another DC bus with a higher rating.

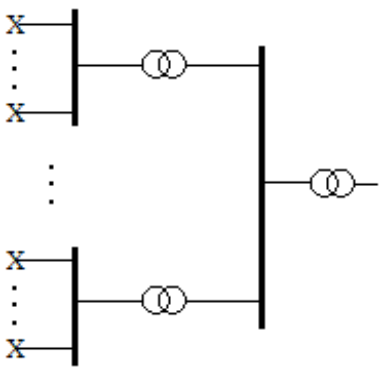

(a) AC collection topology

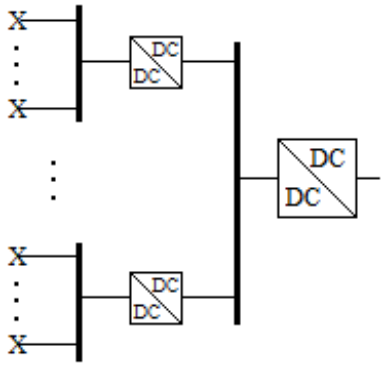

(b) DC collection topology

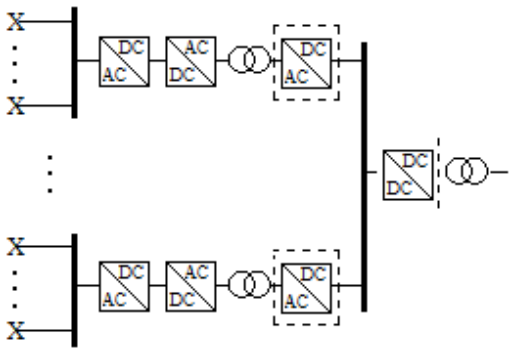

(c) Hybrid collection configuration

Figure 2.4: Different collection configuration between the clusters after the turbines in one cluster are connected.

The third configuration is untested in large scale wind power systems so far. The turbines are connected directly after the generator. A rectifier, rated for the total power of the connected turbines, is then used to convert into DC at a connected DC-link. Furthermore, a regular inverter can be used, connected to a standard AC transformer. Conversely, a DC-DC converter with a medium-frequency transformer can be employed. The first part is, in any case, an inverter. This topology has both advantages and drawbacks, but is in [22] and [23] argued to be beneficial. The attention is that several turbines share the whole converter system, reducing the number of needed converters to the number of clusters. However, there are problems regarding the control of such a system, since several turbines need to be

controlled by one single converter. Research has to be performed regarding this topology, but a high amount of savings in terms of size and weight may outweigh the possible reduction in performance. Also, due to the short distances between the rotors in a multi-rotor wind turbine, the wind profile might not vary too much. At least, the distances are less than what is assumed in an offshore wind farm proposing this, as suggested in [22] and [23].

There are different alternatives in connections, depending on the further connections should be realised in DC with DC-DC converters, or in AC, before connecting the clusters. Due to this possibility of first connecting generators, while in AC, then making the rest of the collection in DC, the topology is called a hybrid cluster. This configuration can be seen in Figure 1.1c. However, for comparison aspects, only the part until the shared inverter is studied, as this is present either if a normal-frequency or medium-frequency transformer is employed next.

The collection grid is shown in Figure 2.4c. One X in this figure represents just one turbine, and several turbines are connected to the same two converters, where the latter may serve different purposes. One solution is this being a normal inverter. Then the inverter surrounded by the dotted line is removed, and a transformer is stepping up the voltage before all clusters are connected at a common AC bus. Another option is that the inverter is used as a part of a DC-DC converter, increasing the frequency and having a medium-frequency transformer. Then, the clusters are connected at a common DC bus before another DC-DC converter steps up the voltage before transmission.

2.4 Summary

This chapter first presents the history of the multi-rotor system, which reaches back to the early 1900s. Reasons why it is now gaining attention are pointed out, and more recent work on this concept is declared. Furthermore, the observed aerodynamic gains compared to conventional wind turbines found from both simulations and the Vestas 4-rotor demonstrator are laid out. As little work is performed on the electrical design of the collector system, important cautions on this are presented. Moreover, different ways to connect the wind turbines within one cluster are argued for, as well as connecting all the clusters to pose the whole multi-rotor wind turbine proposed.

Chapter 3

The Multi-Objective Optimisation Method

The selection between the different configurations between the individual turbines in a multi-rotor wind turbine is a challenging task. Many aspects need to be taken into consideration, such as minimising the amount of mass and volume needed, while maintaining excellent efficiency and reliability. Moreover, since no such installation has ever been realised in full-scale, a techno-economical analysis needs to be carried out.

In literature, there exist numerous options when it comes to different configurations of wind turbines in cluster and collector topologies. In work belonging to this thesis [12], three entirely different, general topologies were selected. These general configurations, already presented as the AC cluster, the DC cluster, and the hybrid cluster, are used as a base for this work. In [12], the focus was to calculate the power losses of the power electronic semiconductors and use this as a guideline. However, to only study one parameter makes it challenging to provide well-argued for recommendations. The power losses, or efficiency, is of great interest, but to limit the volume and mass of the system is also of high relevance. Unfortunately, optimising efficiency and size are two conflicting objectives when it comes to the components studied in this work.

Thus, several parameters must be taken into consideration when it comes to comparing the different topologies. This is the idea behind the so-called multi-objective optimisation where several essential parameters can be studied to obtain a solution that satisfies many design criteria in the best trade-off. This chapter, therefore, defines the parameters studied more in detail in this work and how they may influence each other. Also, how these parameters can be studied to obtain the best solution, using the so-called Pareto frontier, is presented.

3.1 Key parameters for comparison

As the motivation to commence the study of the multi-rotor concept is the possible increased power output for the same swept area compared to single-rotor wind turbines, as well as savings in material, parameters which are reflecting these aspects are relevant in this work. With this in mind, the same three parameters used by [24] may also be used here.

First, one important parameter is, undoubtedly, the efficiency η, which is defined in (3.1). To develop a system with low losses is essential for making the multi-rotor system competitive with today's commercial large wind turbines. Moreover, the whole system requires a high number of generators, power electronics, transformers, passive components, as well as power cables. These components combined need to prove excellent efficiency and be competitive to the modern large-scale wind turbines in terms of this. As this study is limited to focus on the power electronics components, these losses are what is used to estimate η. Even though the different designs also have different losses associated with the generator, power lines filters, and other excluded components, will this not be taken into account here. The efficiency is represented by the input power P_{in} and calculated power losses $P_{loss,(i)}$ from the individual components as follows:

$$\eta = \frac{P_{in} - \sum_{i=1} P_{loss,(i)}}{P_{in}} \cdot 100\% \tag{3.1}$$

Second, a parameter describing the compactness of an installation related to the amount of power is of interest. Hence, the ρ, expressing the power density is an important factor and is defined by (3.2) as:

$$\rho = \frac{P_{out}}{Vol_{Tot}} = \frac{P_{in} - \sum_{i=1} P_{loss,(i)}}{\frac{1}{C_{PV}} \sum_{i=1} Vol_{(i)}} \tag{3.2}$$

Since the multi-rotor system, with its multiple rotors, inevitably results in a sizeable system, it is still essential to keep it as compact and size efficient as possible. This parameter can be calculated by adding the individual volumes $Vol_{(i)}$ and dividing the output power on this together with a utilisation factor C_{PV}, as there are some physical limits of how compact the system can be placed.

Finally, the third parameter to be used is the power-to-mass ratio. As there is no one-to-one relationship between volume and mass in installations like these, because of the difference in mass density, the aspect regarding mass is also of a huge relevance. As an example, the copper used in inductors has a relatively high mass density. So even if they use limited space, they may take up a larger part of the total mass. As the multi-rotor system is large in extent, the possibilities to

reduce weight wherever possible is of a huge pertinency. Also, offshore and floating solutions have been proposed, making the demand for reduced weight a key for the installation. The energy-to-mass ratio γ is defined by the output power divided by the total summarised weight $W_{(i)}$ of the individual components, as shown below:

$$\gamma = \frac{P_{out}}{W_{Tot}} = \frac{P_{in} - \sum_{i=1} P_{loss,(i)}}{\sum_{i=1} W_{(i)}} \tag{3.3}$$

One of the main demands of wind turbine systems designs, or any other energy conversion system, is to obtain a high efficiency η without getting too large dimensions, i.e., high power density ρ and high power-to-mass ratio γ. For most wind turbine technologies, these aspects are conflicting. According to the literature [24], which is also presented in Chapter 4, efficiency decreases when the switching frequency increases. This correlation is because the power losses increase, mainly due to the energy dissipation related to the switching. However, the size of the system will, until one point, decrease with increasing switching frequency as many components can be designed smaller if they are designed for a high switching frequency, especially capacitors and inductors, which is demonstrated in Chapter 4. Hence, the two objectives are conflicting, and a trade-off must be found where the efficiency is sufficient without the need of too large components. These relationships can be illustrated by the different plots in Figure 3.1.

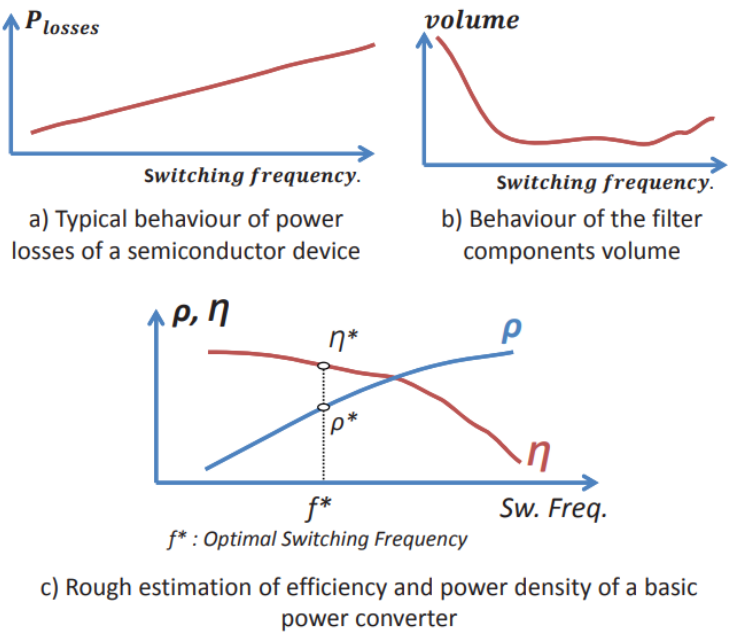

Figure 3.1: Power electronic converter typical behaviour and trade-off between efficiency and size [24].

Moreover, another important aspect regarding the choice of design for a multi-rotor wind turbine system is the number of individual components needed. It is well-known that the power converters have a high failure rate when looking at the electrical system. In fact, they are among the most frequently failing components of wind turbines [25]. According to [23], studies have shown that the failure intensity of wind turbine converters typically ranges from 0.045-0.3 failures per year, which is a lot compared with the other electrical components from the same study. As the structure is meant offshore, a system with a low failure rate is desired, as the downtime can be prolonged until the failure can be fixed, and the turbine can run with at its total rated power again. Since one major problem is the converter, a topology where the number of needed power converters is reduced may be beneficial in terms of this. The number of converters and other components is, therefore, also of importance when designing a multi-rotor wind turbine system.

3.2 Multi-objective optimisation and Pareto-front

As obtaining high efficiency in addition to high power density is two conflicting objectives as seen in Figure 3.1, a multi-objective optimisation method is found

beneficial, as there can be several possible solutions, depending on the application. The idea behind the method is to establish several performance indices, which can be optimised. These indices, presented in (3.1) - (3.3), are used to design a Pareto-front.

Pareto optimisation, often used in the field of economic optimisation, is explained in [26] and aims to find the optimal solution when combining N objectives, which often are somewhat contradictory. It may be defined as: *An optimal solution is said Pareto optimal when it is not possible to improve and objective without degrading the others. A Pareto optimal solution can then be seen as an optimal trade-off between the solutions* [27]. Usually, the Pareto front does not give one unique solution, but rather several possible solutions that all are optimal, and a change in one parameter makes the other parameters worse off. Before the Pareto front is reached, a change making one performance index better off without making any other worse off is called a Pareto improvement, and it is when no more such can be made, the Pareto front is reached.

The idea, when using the Pareto analysis for the electrical design of a multi-rotor wind turbine system, is to obtain a range of possible solutions, from where a choice based on weighting the different parameters can be made. Several parameters can be treated in a Pareto analysis, but due to simplicity and illustration purposes, the Pareto plots are kept in two dimensions.

For individual, specific cases, the Pareto analysis can be performed by saving the obtained vectors for the performance indicators (η, ρ and γ) by, for example, varying the switching frequency. A modified Pareto function developed in [24] can be used to obtain the Pareto front between the desired parameters. Besides, when several case studies are performed with different criteria, all the possible solutions can be stored in the vectors for η, ρ and γ, giving an ample space of possible solutions. The Pareto function can, then, be used to obtain the best solution possibilities, or the Pareto front, within these ample space of solutions. The function used can be seen in the appendix.

3.3 Choice of the Optimal Switching Frequency

To obtain an optimal switching frequency for further investigation, a switching frequency that provides the best trade-off between all the indicator parameters is of interest. To obtain this switching frequency, (3.4) should be maximised.

$$\Lambda = \frac{\eta}{\eta_{max}} + \frac{\rho}{\rho_{max}} + \frac{\gamma}{\gamma_{max}} \tag{3.4}$$

In the expression, η, ρ and γ are defined in (3.1) - (3.3), and η_{max}, ρ_{max} and

γ_{max} are the maximum values of these functions. The Λ represents how close the individual parameters performs compared to their respective maximum value. Thus, the maximum value of Λ when using three parameters is three.

However, it is not given that the frequency corresponding to the maximum Λ should be the design point unless the three parameters are weighted precisely equal. In reality, this may not be the case for the multi-rotor system. All three parameters are of vital importance, as the power density and power-to-mass ratio are crucial to optimise when an offshore structure is regarded. One of the major advantages of this proposed system is the possible savings in materials, so a design with low volume and mass is essential. Besides, if the system can not be proven to be cost-efficient in terms of material and at the same time maintain efficiency at the level of commercial single-rotor wind turbines, it is never manufactured. So all parameters are of importance, but this equation alone cannot give the only design point. i

3.4 Summary

In this chapter, the need for additional parameters to optimise the configurations is pointed out. These parameters, based on the work in [24], are defined, and their importance for the treated system is explained. Moreover, how optimising these parameters may be conflicting objectives is specified, and how to make Pareto analysis based on the given parameters is presented. Finally, an equation including all three parameters are presented, and maximising this can provide an optimal design switching frequency.

Chapter 4

Modelling of Power Converter Components

In order to perform optimisation of the key performance indicators η, ρ, and γ for the different connection options, extensive evaluations of the power losses, volume and mass for the relevant power converter components have to be performed.

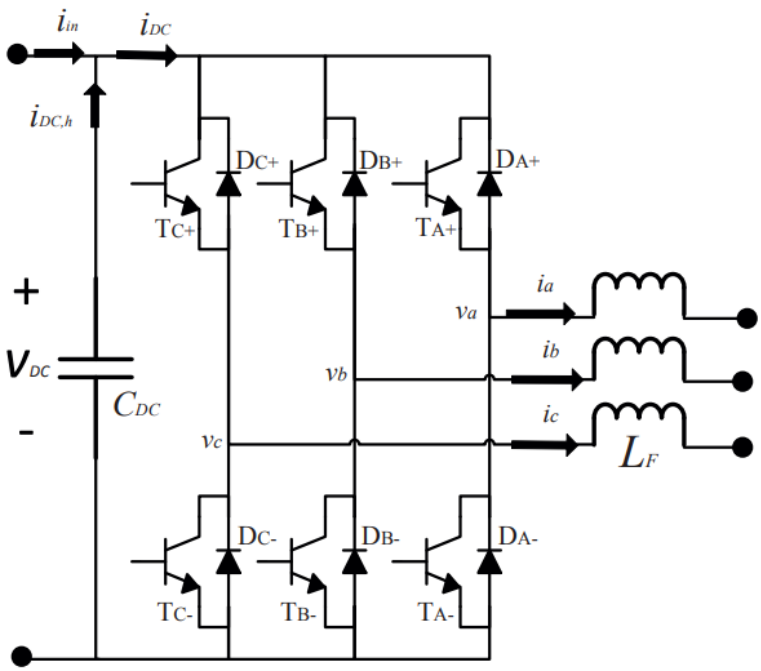

Figure 4.1: Model of a two-level voltage source converter [24].

The studied components of this work, hence the DC capacitor, semiconductor switch valves, and the phase reactors are shown in Figure 4.1. Thus, the needed theory and equations for these are presented in this chapter.

The central relations are obtained from [24], in combination with other literature treating these topics. At first, the different modulation techniques which are studied are briefly presented, and their main differences are explained. Further follows sections for the semiconductors, phase reactors, and DC capacitors, where the calculations for power losses, volume and mass are laid out. Besides, the semiconductor and inductor currents, as well as the capacitor voltage and current are defined. Finally, the total power losses, volume, and mass of the system are expressed.

4.1 Modulation techniques

The choice of modulation technique has significant consequences on the design of the system. Due to their distinctness, the different modulation techniques change essential design criteria and influences the choice of components. It is, therefore, of interest to study more than one modulation strategy, to observe the changes and relationships when using different techniques.

As the modulation technique in this study is not implemented in a simulation tool, studying more techniques is less complicated and is mainly to observe how the design is influenced according to different modulation. Thus, the Sinusoidal Pulse Width Modulation (SPWM), the Space Vector Pulse Width Modulation (SVPWM) and the Symmetrical Flat-Top Modulation (SFTM) techniques are explained, and these methods are illustrated in Figure 4.2.

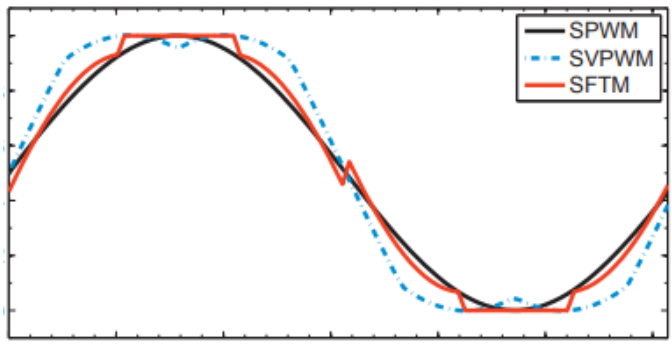

Figure 4.2: Modulating signals for the SPWM, SVPWM and SFTM [24].

4.1.1 SPWM

A sinusoidal PWM (SPWM) allows the pulse to be modulated sinusoidal, and provides only odd harmonics [28]. In addition, the SPWM method reduces the low-frequency harmonics [29]. The desired sinusoidal wave, also called the modulating wave, is in this method compared to a triangular waveform with a much higher frequency, called the switching frequency. This results in several turn-on and turn-offs of the switches within the cycles. The black line in Figure 4.2 illustrates the modulation wave. This wave is compared with a high-frequency triangular wave, and this decides the switching states of the switches, which again has various pulse width. The possible voltage to obtain using this method is given by (4.1) [30].

$$V_{LL} = \frac{\sqrt{3}}{2\sqrt{2}} \cdot V_{DC} \tag{4.1}$$

In 4.1, the V_{DC} is the DC voltage of the DC link and V_{LL} is the line-to-line RMS-voltage of the system (or sinusoidal converter voltage). To define a generic expression relating the sinusoidal voltage to the DC voltage, a scaling factor K_{mod} is defined. When this scaling factor for the SPWM method is set to $K_{mod} = \frac{\sqrt{2}}{4}$ and the modulation index M_S is included, the general and the expanded expression for this method can be represented by:

$$V_{DC} = \frac{V_{LL}}{\sqrt{3} \cdot K_{mod} \cdot M_S} = \frac{4 \cdot V_{LL}}{\sqrt{3} \cdot \sqrt{2} \cdot M_S} = \frac{2\sqrt{2}}{\sqrt{3} \cdot M_S} \cdot V_{LL} \tag{4.2}$$

4.1.2 SVPWM and SFTM

Some modifications on the modulation method can be performed, such as connecting at the third harmonic [31]. A popular modulation approach for a two-level converter is Space Vector Pulse Width Modulation (SVPWM) [32]. The method is more advanced and requires more computational effort, but increases the output capability. The blue line in Figure 4.2 illustrates the modulating wave of this method. This method also decreases the losses due to harmonics and provides a 15 % higher output voltage than what is possible with the SPWM [31]. The SVPWM method is described in detail in [31]. Using this modulation, the possible voltage is given by 4.3.

$$V_{LL} = \frac{V_{DC}}{\sqrt{2}} \tag{4.3}$$

Another method that shares a lot of the same attributes as the SVPWM in terms of increasing the output voltage is the Symmetrical Flat Top Modulation (SFTM).

The modulating signal of this method is illustrated as the red line in Figure 4.2 and is also called Discontinuous Pulse Width Modulation (DPWM1) [33]. This method leaves out one of the two possible zero-voltage switching states [34], and leads to a reduced amount of switching cycles in addition to a reduced effective switching frequency. More about this modulation technique can be found in [34].

Also here, in order to fulfil a generic expression for the relationship between the line-to-line voltage V_{LL} and DC voltage V_{DC} for all modulation methods, the scaling factor for SVPWM and SFTM needs to be set to $K_{mod} = 1/\sqrt{6}$. Thus, the DC voltage for the SVPWM and SFTM method equals:

$$V_{DC} = \frac{V_{LL}}{\sqrt{3} \cdot K_{mod} \cdot M_S} = \frac{V_{LL} \cdot \sqrt{6}}{\sqrt{3} \cdot M_S} = \frac{\sqrt{2}}{M_S} \cdot V_{LL} \tag{4.4}$$

4.2 Semiconductors and Switch Valves

Power converts can be constructed of different semiconductor devices, such as the MOSFET, BJT, IGBT [35]. In this study, switch valves of IGBTs and anti-parallel diodes are assumed, and this configuration is hereafter referred to as an IGBT module. A switch valve may consist of several IGBT modules, connected in series or parallel. Adding modules increases the capacity of the switch valve, as the series connection increases the possible voltage rating, and parallel connection the possible current rating. The dissipated energy related to the switch valves increases the device temperature. Thus, a properly dimensioned cooling system is required.

The behaviour and characteristics of the semiconductors depend on the rating and size, which affects the power losses, volume, and mass. How these parameters are calculated is explained in this section, mainly based on [24].

4.2.1 Power losses

The power losses for the semiconductors are divided into conduction losses and switching losses. The conduction losses are related to the on-state of the devices, which is when they are conducting current, the middle part in Figure 4.3. Thus, the on-state resistance for the particular device is of importance and can for a fixed temperature be found in the device datasheet.

On the other side, the switching losses are related to the transition between states. As can be seen in Figure 4.3, energy from this transition is dissipated when the voltage decreases from the blocking voltage to a voltage of low value and the device current at the same time increases. Thus, the dissipated energy during each switching summarised, poses the switching losses.

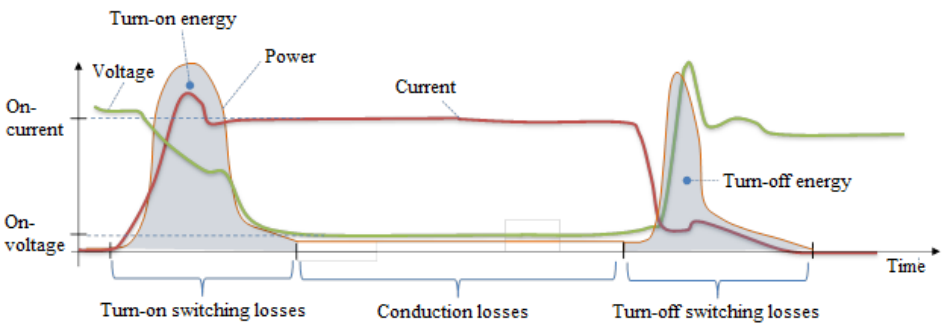

Figure 4.3: Switching and conduction losses of semiconductor [36].

Figures in a semiconductor datasheet can illustrate the voltage-current characteristics for a semiconductor device. In the blocking state, the current is very low until the maximum blocking voltage is reached. Therefore, the blocking state losses can be neglected without losing any accuracy of importance. Nevertheless, in the conduction state, the actual switch device voltage v_{sw} can be linearly approximated as:

$$v_{sw} = V_{sw0} + R_C \cdot i_{sw} \tag{4.5}$$

In (4.5), V_{sw0} is the switch device threshold voltage, R_C the on-state resistance and i_{sw} the current through the switch device. This expression is separated into expressions for both the IGBTs and diodes. If datasheets for IGBT modules are investigated, it is visible that both the threshold voltage as well as the on-state resistance are temperature-dependent. Usually, the data at two different temperatures are given, so a linear approximation is used to express the temperature dependence of these parameters. Hence, the threshold voltage and on-state resistance at junction temperature T_j is given as:

$$V_{sw0}(T_j) = V_{sw00} \cdot (1 + \alpha_{Vsw0} \cdot (T_j - T_{j0})) \tag{4.6}$$

$$R_C(T_j) = R_{C0} \cdot (1 + \alpha_{RC} \cdot (T_j - T_{j0})) \tag{4.7}$$

Here, α_{Vsw0} and α_{RC} are temperature coefficients, V_{sw00} and R_{C0} are the threshold voltage and on-state resistance for a fixed reference junction temperature T_{j0} and can be found in the datasheet of the device.

The instantaneous dissipated power P_{cond} is then given by the product of voltage and current. The average losses over one time period T can be written as:

$$P_{cond} = \frac{1}{T}\int_0^T (v_{sw} \cdot i_{sw})dt = \frac{1}{T}\int_0^T (V_{sw0}(T_j) + R_C(T_j) \cdot i_{sw}) \cdot i_{sw} \cdot dt \tag{4.8}$$

Assuming constant temperature during one time period, (4.8) can be written as:

$$P_{cond} = \frac{V_{sw0}(T_{j,AVG})}{T}\frac{1}{T}\int_0^T i_{sw}dt + \frac{R_C(T_{j,AVG})}{T}\frac{1}{T}\int_0^T i_{sw}^2 dt \tag{4.9}$$

In (4.9), $T_{j,AVG}$ is the average junction temperature. When the time varying currents are evaluated, (4.9) is simplified to:

$$P_{cond} = V_{sw,0}(T_{j,AVG}) \cdot I_{sw,AVG} + R_C(T_{j,AVG}) \cdot I_{sw,RMS}^2 \tag{4.10}$$

$I_{sw,AVG}$ and $I_{sw,RMS}$ are the average and RMS current the switch device is conducting in a given period. How to obtain these currents, which again are separated into IGBT and diode currents, I_t and I_d is studied in the next section.

The switching losses consist of the dissipated energy from the commutation at turn-on and turn-off in the IGBTs, as well as the reverse recovery losses for the diodes. These reverse recovery losses are hereafter mentioned as the dissipated energy during turn-off for the diodes.

The parameters of interest when calculating the switching losses are the switch device voltage right before turn-on and right after turn-off, v_{swb} and v_{swa}, as well as the currents through the device right before turn-on and after turn-off, i_{swb} and i_{swa}, values which can be interpreted from Figure 4.3. The dissipated energy is also temperature dependent, and a proposed model to calculate this temperature dependent energy $E_{sw,on}$ and $E_{sw,off}$ is given in [24] as:

$$E_{sw,on} = E_{sw0,on} \cdot (1 + \alpha_{Eon} \cdot (T_j - T_{j0})) \tag{4.11}$$

$$E_{sw,off} = E_{sw0,off} \cdot (1 + \alpha_{Eoff} \cdot (T_j - T_{j0})) \tag{4.12}$$

Here, $\alpha_{Eon/off}$ are the temperature coefficients of commutation energy loss at turn-on and turn-off. These can be calculated using the datasheet of the device. The temperature-independent dissipated energy $E_{sw0,on}$ and $E_{sw0,off}$ are given as:

$$E_{sw0,on} = v_{swb} \cdot (K_{Eon0} + K_{Eon1} \cdot i_{swa} + K_{Eon2} \cdot i_{swa}^2) \tag{4.13}$$

$$E_{sw0,off} = v_{swa} \cdot (K_{Eoff0} + K_{Eoff1} \cdot i_{swb} + K_{Eoff2} \cdot i_{swb}^2) \tag{4.14}$$

The polynomial regression coefficients ($K_{E(on/off)(0/1/2)}$) are used to describe how the commutation energy losses depend on the current at turn-on and turn-off and can be calculated using the datasheet of the device.

Similar as for the conduction losses, the average losses can be obtained by summarising the dissipated energy during one time interval and divide by the time interval. Also here, the junction temperature is regarded as constant during one period, and the switch device voltage right before turn-on and right after turn-off can be approximated as the device blocking voltage V_{bk}. Then the equations are simplified to

$$E_{sw0,on} = V_{bk} \cdot (K_{Eon0} + K_{Eon1} \cdot I_{swa,AVG} + K_{Eon2} \cdot I_{swb,RMS}^2) \tag{4.15}$$

$$E_{sw0,off} = V_{bk} \cdot (K_{Eoff0} + K_{Eoff1} \cdot I_{swb,AVG} + K_{Eoff2} \cdot I_{swb,RMS}^2) \tag{4.16}$$

Here, $I_{swa,AVG}$, $I_{swa,RMS}$, $I_{swb,AVG}$ and $I_{swb,RMS}$ are the average and RMS values of the currents through the switch devices at the moment after (a) and before (b) it is turned off. These values can be calculated based on the input and output current of the converter, and they mainly depend on the converter topology, modulation strategy, and power factor. The procedure to obtain the different device currents are explained in the next section.

The switching losses $P_{sw,on}$ and $P_{sw,off}$ are further found by multiplying the dissipated energy per switching with the number of switching per second, hence the switching frequency f_{sw}, and assuming a constant junction temperature $T_{j,AVG}$ during one period. The gives (4.17) and (4.18).

$$P_{sw,on} = f_{sw} \cdot E_{sw,on} = f_{sw} \cdot E_{sw0,on} \cdot (1 + \alpha_{Eon} \cdot (T_{j,AVG} - T_{j0})) \tag{4.17}$$

$$P_{sw,off} = f_{sw} \cdot E_{sw,off} = f_{sw} \cdot E_{sw0,off} \cdot (1 + \alpha_{Eoff} \cdot (T_{j,AVG} - T_{j0})) \tag{4.18}$$

4.2.2 Semiconductor device currents

Both the equations for the conduction losses in (4.10) as well as the switching losses in (4.17) and (4.18) are dependent on the average and RMS currents of the semiconductor device.

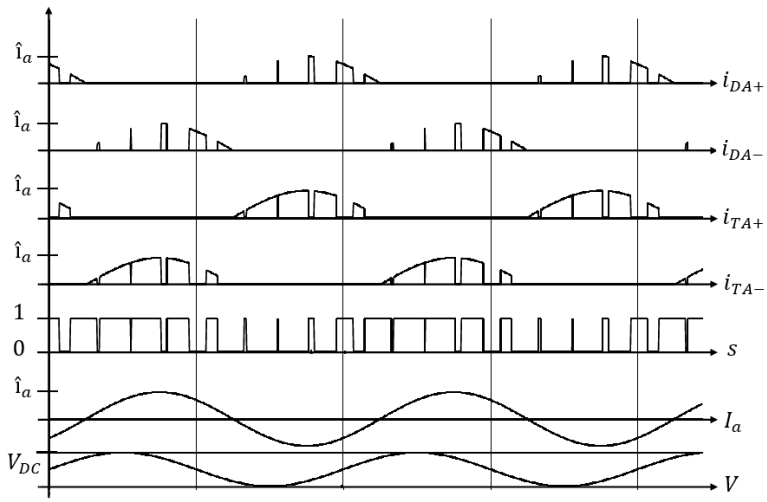

Figure 4.4: Phase current divided into its components [37].

The relationship between the device output current and the currents in the diodes and IGBTs is rather complex, especially for the RMS currents. This complexity comes clear in Figure 4.4 where the currents in the different diodes and IGBTs in one half-bridge are shown and can be compared to the semiconductor devices in Figure 4.1.

The currents $I_{sw,AVG}$ and $I_{sw,RMS}$ needed to evaluate the conduction losses in (4.10) are divided into IGBT and diode currents, I_t and I_d. The average currents are functions of the relative turn-on time α_a of the converter and the displacement angle θ, as shown in (4.19) and (4.20).

$$I_{t,AVG} = \frac{1}{2\pi} \int_{\phi}^{\pi+\phi} (\alpha_a(\theta) \cdot i_a(\theta)) \cdot d\theta \tag{4.19}$$

$$I_{d,AVG} = \frac{1}{2\pi} \int_{\phi}^{\pi+\phi} ((1 - \alpha_a(\theta)) \cdot i_a(\theta)) \cdot d\theta \tag{4.20}$$

These equations need to be carefully evaluated to obtain correct expressions. This is performed in previous works [38, 39] for many modulation methods such as SPWM, SVPWM and SFTM method and summarised in [24]. A comparison shows that the expressions for the average currents are identical because of the defined scaling factor K_{mod} and can be expressed as in (4.21) and (4.22). The currents are dependent on the modulation index M_S, the displacement angle θ, and the phase

current I_a as shown below.

$$I_{t,AVG} = \frac{\hat{I}_a}{2}\left(\frac{1}{\pi} + \frac{M_S \cdot \cos\phi}{4}\right) = \left(\frac{\sqrt{2}}{2\pi} + \frac{K_{mod}}{2} \cdot M_S \cdot \cos\phi\right) \cdot I_a \tag{4.21}$$

$$I_{d,AVG} = \frac{\hat{I}_a}{2}\left(\frac{1}{\pi} - \frac{M_S \cdot \cos\phi}{4}\right) = \left(\frac{\sqrt{2}}{2\pi} - \frac{K_{mod}}{2} \cdot M_S \cdot \cos\phi\right) \cdot I_a \tag{4.22}$$

Meanwhile, performing evaluations of the RMS currents reveals that these are dependent on the modulation method. The IGBT currents are presented in [24] as:

$$\left(\frac{I_{t,RMS}}{I_a}\right)^2 = \frac{3\pi + 8 \cdot M_S \cdot \cos\phi}{12\pi} \tag{4.23}$$

$$\left(\frac{I_{t,RMS}}{I_a}\right)^2 = \begin{cases} \frac{-M_S+3\pi-4M_S\cos^2(\phi)+8\sqrt{3}M_S\cos(\phi)}{12\pi} & |\phi| < \frac{\pi}{6} \\ \frac{3\pi+2M_S(2+\frac{\sqrt{3}}{2}\sin|2\phi|-\cos^2(\phi))}{12\pi}\ldots & \\ \ldots + \frac{2M_S(-2\sin|\phi|+2\sqrt{3}\cos(\phi))}{12\pi} & \frac{\pi}{6} < |\phi| < \frac{\pi}{2} \end{cases} \tag{4.24}$$

$$\left(\frac{I_{t,RMS}}{I_a}\right)^2 = \begin{cases} \frac{(6-8M_S)\sqrt{3}\cos^2(\phi)+\sqrt{3}M_S(4+8\cos(\phi))}{12\pi}\ldots & |\phi| < \frac{\pi}{3} \\ \ldots\frac{-8M_S\sin|\phi|+(4M_S-3)\sin|2\phi|-3\sqrt{3}+2\pi+6|\phi|}{12\pi} & \\ \frac{3\pi-3|\phi|+(4M_S-3)\sin|2\phi|}{6\pi} & \frac{\pi}{3} < |\phi| < \frac{\pi}{2} \end{cases} \tag{4.25}$$

(4.23) is the expression for SPWM, (4.24) for the SVPWM and (4.25) for the SFTM method. The evaluations performed on (4.21) and (4.22) to obtain (4.23), (4.24) and (4.25) can be studied more in detail by conferring [39] for the SPWM method and [38] for the SVPWM and SFTM methods.

When these are obtained, the diode current can easily be obtained as:

$$\left(\frac{I_{d,RMS}}{I_a}\right)^2 = \frac{1}{2} - \left(\frac{I_{t,RMS}}{I_a}\right)^2 \tag{4.26}$$

Notice that (4.26) is obtained from geometric considerations, making it valid for all modulation methods mentioned above. The previously obtained currents contribute to calculating the conduction losses, from previously stated equations.

Furthermore, the switching losses need the values of the average and RMS currents through the device right after it is turned on and right before turn-off. A

fair approximation to be made is that the current in the upper IGBT at turn-on is equal to the current through the lower diode at turn-off [24]. Also, the current can be regarded as constant during one switching period, if high switching frequencies are assumed. From this follows that the turn-on switching current can be regarded as equal to the turn-off switching current. Therefore, the average and RMS values of the current through all devices can be treated as equal, which gives:

$$I_{swa,AVG} = I_{swb,AVG} = I_{ta,AVG} = I_{tb,AVG} = I_{db,AVG} \tag{4.27}$$

$$I_{swa,RMS} = I_{swb,RMS} = I_{ta,RMS} = I_{tb,RMS} = I_{db,RMS} \tag{4.28}$$

Here, $I_{ta,AVG}$ and $I_{ta,RMS}$ are the average and RMS currents at the moment after turn-on respectively, and $I_{tb,AVG}$, $I_{tb,RMS}$, $I_{db,AVG}$ and $I_{db,RMS}$ are the average and RMS values of the current through the IGBTs and diodes right before turn-off respectively. These two currents can be evaluated by:

$$I_{swa,AVG} = \frac{1}{2\pi} \int_{\phi}^{\pi+\phi} (\alpha_{swa}(\theta) \cdot i_a(\theta)) \cdot d\theta \tag{4.29}$$

$$I_{swa,RMS} = \sqrt{\frac{1}{2\pi} \int_{\phi}^{\pi+\phi} (\alpha_{swa}(\theta) \cdot i_a^2(\theta)) \cdot d\theta} \tag{4.30}$$

Here is α_{swa} the switching function of the converter, which again is a function of the relative turn-on time α_a of the converter leg given above:

$$\alpha_{swa} = \begin{cases} 1 & 0 < \alpha_a < 1 \\ 0 & \alpha_a = 1 \text{ or } \alpha_a = 0 \end{cases} \tag{4.31}$$

This results, based on [24], in the simple expressions for the current which yields for both the SPWM and SVPWM methods, expressed in (4.32) and (4.33).

$$I_{swa,AVG} = \frac{\sqrt{2}}{\pi} \cdot I_a \tag{4.32}$$

$$I_{swa,RMS} = \frac{1}{\sqrt{2}} \cdot I_a \tag{4.33}$$

For the SFTM, the expressions are more complicated, as can be seen in (4.34) and

(4.35).

$$I_{swa,AVG} = \begin{cases} \frac{\sqrt{2}(2-\cos(\phi))}{2\pi} I_a & |\phi| < \frac{\pi}{3} \\ \frac{\sqrt{6}\sin(\phi)}{2\pi} I_a & \frac{\pi}{3} < |\phi| < \frac{2\pi}{3} \\ \frac{\sqrt{2}(2+\cos(\phi))}{2\pi} I_a & \frac{2\pi}{3} < |\phi| < \pi \end{cases} \tag{4.34}$$

$$I_{swa,RMS} = \sqrt{\frac{1}{3\pi} - \frac{\sqrt{3}}{4\pi} \cdot \cos(2\phi)} \cdot I_a \tag{4.35}$$

4.2.3 Cooling system, volume and mass

In every state, energy dissipation is adding heat to the system. However, the junction temperature must comply with the maximal junction temperature at every operation state, making essential the need for a proper cooling system. To obtain the desired cooling system, a thermal model can be implemented to obtain the required thermal resistance. If this is done for the worst operating scenario, this data can be used to design the needed cooling system of the switch valve.

It is the cooling system that really makes up the switch valve volume. A cooling system is needed for every module, and to keep the values realistic, there is normally a constraint on the ratio between the cooling system and module volume at around 6-8 [24]. The cooling system consists of an aluminium or copper structure as well as a fan. The heat sink volume Vol_{HSal} and fan volume Vol_{fan} are expressed in (4.36) (4.37) as:

$$Vol_{HSal} = K_{HS0} \cdot \left(\frac{1}{R_{thHS}}\right)^{K_{HS1}} = K_{HS0} \cdot \left(\frac{P_{loss,mod}}{\Delta T_{HS,max}}\right)^{K_{HS1}} \tag{4.36}$$

$$Vol_{fan} = K_{fan0} \cdot (Vol_{HSal} - K_{fan2})^{K_{fan1}} \tag{4.37}$$

R_{thHS} is the thermal resistance, which from its definition is set to total dissipated power $P_{loss,mod}$ divided by the maximum allowable heat sink to ambient temperature difference $\Delta T_{HS,max}$. K_{HS0}, K_{HS1}, K_{fan0}, K_{fan1}, and K_{fan2} are proportionality coefficients found from data for commercially available heat sinks and fans. Since every module requires a heat sink system, the total volume of the switch valve Vol_{valve} is simply the sum of module volume Vol_{mod} and heat sink volume Vol_{HS}, multiplied with the number of parallel and series connected devices, n_p and n_s, and hence:

$$Vol_{valve} = n_p \cdot n_s \cdot (Vol_{mod} + Vol_{HS}) \tag{4.38}$$

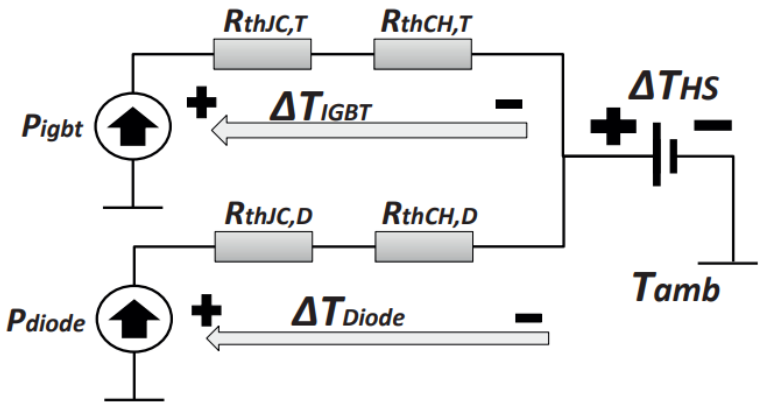

Figure 4.5: Thermal module of an IGBT module [24].

The maximum allowable heat sink to ambient temperature difference, $\Delta T_{HS,max}$ can be obtained by exploring the thermal model for a module consisting of an IGBT and an anti-parallel diode, as in Figure 4.5. From this figure, (4.39) is obtained as:

$$\Delta T_{HS,max} + T_{amb} = K_{SFT} \cdot T_{j,max} - \Delta T_{mod,max} \tag{4.39}$$

In 4.39, K_{SFT} is the safety factor of thermal design, $T_{j,max}$ is the maximum junction temperature and T_{amb} is the ambient temperature. $\Delta T_{mod,max}$ is given by:

$$\Delta T_{mod,max} = max\left\{R_{th,igbt} \cdot \frac{P_{igbt}}{N_{isxm}}; R_{th,diode} \cdot \frac{P_{diode}}{N_{isxm}}\right\} \tag{4.40}$$

Here, $R_{th,igbt}$ and $R_{th,diode}$ are the junction-to-heat sink thermal resistance of the IGBT and diode, given in the module datasheet. N_{isxm} is the number of internal IGBTs/diodes per module, while P_{igbt} and P_{diode} are the conduction and switching losses in the IGBTs and diodes respectively, consisting of the conduction and switching losses from previous equations.

As the power losses in the switch valves increase with switching frequency, also the dissipated energy and temperature increase. Consequently, the thermal resistance is reduced for high power losses. When the thermal resistance for one switching frequency eventually is too low, the number of connected semiconductor devices needs to be increased, as this gives a sudden increase in the total thermal resistance. Both the limit in minimum thermal resistance and the expression for the switching frequency-dependent thermal resistance can be found by investigating

(4.36).

When the volume is obtained, the mass can be found by the density of the material used. The mass is calculated by (4.41), where ρ_{module} and Vol_{module} are module density and volume, given in a device datasheet, along with the densities for the fan and heat sink, ρ_{fan} and ρ_{HSal}, which also can be calculated from datasheets.

$$Mass_{valve} = n_s \cdot n_p \cdot (\rho_{module} \cdot Vol_{module} + \rho_{fan} \cdot Vol_{fan} + \rho_{HSal} \cdot Vol_{HSal}) \quad (4.41)$$

4.3 Phase reactors and filter inductors

In order to control both the active and reactive flow of power, the phase reactors are used to regulate the currents through them [40]. The phase reactors of a VSC can be seen as the inductors to the right at the two-level converter in Figure 4.1. The reactors also work as a filter which helps to reduce the harmonic contents created in the currents from the switching of the converters. The size of the phase reactors depends on, among other things, the switching frequency, which also influences the losses. These relationships are explained in this section.

To simplify the model, only the phase reactor inductor is studied in this work. Nonetheless, additional inductors are required for realising LCL-filters to minimise the current ripple. The same generic methods for calculating power losses, volume, and mass, are valid for filter inductors, but calculations for this are not included in this work. However, qualitative aspects regarding filters are discussed in Chapter 6.

4.3.1 Power losses

The inductor losses are divided into winding and core losses. To obtain the winding losses, the power loss density is expressed and used together with both electrical and reference parameters to obtain the final expression. Derivations in detail can be found in [24] and the final expression for the inductor winding losses P_{wL} is presented in (4.42).

$$P_{wL} = \left[1 + \left(\frac{2}{3} + \frac{4}{\pi^2}\left(\frac{f_{sw}}{f_{L1}}\right)^2\right)\left(\frac{\delta_{iL}^2}{6}\right)\right] \cdot \left[\frac{2f_{Lref}^2 + f_{L1}^2}{3f_{Lref}^2}\right] \cdot K_{\rho w0} \cdot Vol_L^{K_{\rho w1}} \quad (4.42)$$

In (4.42), f_{L1} is the fundamental frequency, f_{Lref} the inductor reference frequency, f_{sw} the switching frequency $K_{\rho w0}$ and $K_{\rho w0}$ are proportionality regression coefficients found from reference inductor technology. Vol_L is the inductor volume

defined in (4.45) and δ_{iL} is the ratio of peak-to-peak current ripple to maximum fundamental current, defined by (4.43).

$$\delta_{iL} = \frac{\Delta I_{Lh}}{\sqrt{2} I_{L1}} \tag{4.43}$$

I_{Lh} and I_{L1} are the two components that pose the inductor current, hence the inductor ripple current and the fundamental current. Thus, ΔI_{Lh} means the peak-to-peak current ripple. This ratio δ_{iL} typically has a maximum level, as it is desirable to keep it as low as possible.

Moreover, the core loss equation is a result of longer derivation, with a base in Steinmetz equation [41], which is an empirical way of approximating the core power loss density. How this is further derived to result in (4.44), can be studied in detail in [24]. Thus, the core losses P_{coreL} equal:

$$P_{coreL} = \left(\frac{6 + \left(\frac{\delta_{iL} f_{sw}}{f_{L1}} \right)^2}{6 + \delta_{iL}^2} \right)^{\frac{\alpha_L}{2}} \cdot \left(1 + \frac{\delta_{iL}}{2} \right)^{\beta_L} \cdot K_{\rho c0} \cdot Vol_L^{K_{\rho c1}} \cdot \left(\frac{f_{L1}}{f_{Lref}} \right)^{2 \cdot (\alpha_L - \beta_L)} \tag{4.44}$$

$K_{\rho c0}$ and $K_{\rho c0}$ are proportionality regression coefficients found from reference inductor technology and α_L and β_L are Steinmetz constants related to the material [41].

4.3.2 Volume and mass

Both inductor volume and mass are proportional to the inductance and the inductor current. This relationship can be viewed more in detail in [24], where the following expressions for the inductor volume Vol_L and mass $Mass_L$ are derived.

$$Vol_L = K_{VL0} \cdot (L_F \cdot I_L^2)^{K_{VL1}} \tag{4.45}$$

$$Mass_L = K_{\rho L0} \cdot Vol_L^{K_{\rho L1}} \tag{4.46}$$

In (4.45) and (4.46), $K_{VL0}, K_{VL1}, K_{\rho L0}$ and $K_{\rho L1}$ are proportionality regression coefficients obtained from a reference inductor technology and L_F is the inductance value, which is expressed in the next section.

4.3.3 Inductance and inductor current

The inductor value L_F is dependent on the line-to-line voltage V_{LL}, the voltage of the DC-link V_{DC} as well as the peak-to-peak current ripple ΔI_{Lh} at the switching frequency f_{sw}, according to literature [24]. This gives:

$$L_F = \left(\frac{V_{LL}}{\sqrt{3}} - \frac{V_{LL}^2}{2 \cdot V_{DC}} \right) \cdot \frac{1}{\Delta I_{Lh} \cdot f_{sw}} \tag{4.47}$$

The maximum peak-to-peak current ripple is typically specified by the ratio of peak-to-peak current ripple to maximum fundamental nominal current, δ_{iL}, so the required inductance can be expressed by an equation dealing with the possibility of using different modulation techniques, as:

$$L_F = \left(1 - \frac{3}{2} \cdot K_{mod} \cdot M_S \right) \cdot \frac{V_{LL,N}^2 \cdot \cos\phi}{\sqrt{2} \cdot \delta_{iL} \cdot f_{sw} \cdot P_N} \tag{4.48}$$

P_N represents the nominal power the inductors are rated for.

There is a limit in the switching frequency when it comes to the inductance. If the switching frequency is below this value, the inductance is too large, so the design needs to consider this. The value of maximum filter inductance $L_{F,max}$ is also dependent on the ratio of the inductor voltage to line-to-line voltage δ_{VL} and the nominal frequency f_1, and is given by:

$$L_{F,max} = \frac{3 \cdot \delta_{VL} \cdot V_{LL,N}^2 \cdot \cos\phi}{\pi \cdot f_1 \cdot P_N \cdot \sqrt{6 + \delta_{iL}^2}} \tag{4.49}$$

If the back-to-back converter interfaces a generator, which is the case when regarding wind turbines, the machine inductance needs to be taken into consideration at this side. Then the required filter needs to be reduced, by simply subtracting the machine inductance L_M, hence:

$$L'_F = L_F - L_M \tag{4.50}$$

As can be seen from (4.50), the total needed inductance, here expressed by L'_F, becomes negative for $L_M > L_F$. In this case, the inductance at this side can be neglected.

The nominal RMS inductor current I_{LF} consists of both the nominal output current I_a and the current ripple component I_{Lh} and is with some approximations

presented in [24] expressed by:

$$I_{LF} = \sqrt{I_a^2 + I_{Lh}^2} = \sqrt{1 + \frac{\delta_{iL}^2}{6}} \cdot I_a \tag{4.51}$$

4.4 DC capacitor and filter capacitance

The DC capacitor, or the DC link, is located between the rectifier and inverter in a back-to-back converter, as can be seen from the two-level VSC in Figure 4.1. This element works as a storage device, an energy buffer to keep the power balance, in addition to filtering out the voltage ripple [40]. It is dimensioned based on the required DC voltage decided by the system, and how to calculate the power losses, volume and mass of the capacitor is explained in this section.

Capacitors are also generally used after the converter stage as a an additional filter, usually an LCL filter. This is, however, outside the scope to investigate in this study and is proposed to be investigated in a future study.

4.4.1 Power losses

The capacitor losses are composed of two terms, the dielectric losses $P_{\epsilon C}$ and the resistive losses $P_{\Omega C}$. As derived in [24], the dielectric losses for a DC capacitor can be expressed as:

$$P_{\epsilon C} = \frac{\sqrt{3}}{2} \cdot f_{sw} \cdot C \cdot \tan(\delta_0) \cdot \delta_{Vdc}^2 \cdot V_{DC}^2 \tag{4.52}$$

In (4.52), f_{sw} is the switching frequency, C is the capacitance of the plate capacitor used, $\tan(\delta_0)$ is the dissipation factor of the dielectric, δ_{Vdc} is the ratio of peak-to-peak voltage ripple to DC voltage of the converter V_{DC}.

The resistive losses are obtained by the product of the series resistance R_{sC} and the capacitor current I_C squared, as seen in (4.54).

$$P_{\Omega C} = R_{sC} \cdot I_C^2 \tag{4.53}$$

The series resistance is the sum of the resistances inside of the capacitor. It can be estimated based on the equation from [24] as:

$$R_{sC} = K_{\Omega C0} \cdot C^{K_{\Omega C1}} \cdot V_{CN}^{K_{\Omega C2}} \tag{4.54}$$

$K_{\Omega C0}$, $K_{\Omega C1}$ and $K_{\Omega C2}$ are proportionality regression coefficients found by taking

data from reference capacitor technologies, and V_{CN} is the rated voltage of the capacitor.

4.4.2 Volume and mass

The capacitor volume Vol_C and mass $Mass_C$ are related to the capacitance and capacitor voltage. More extensive derivations are found in [24], where the expressions for capacitor volume and mass are given as:

$$Vol_C = K_{VC0} \cdot C^{K_{VC1}} \cdot V_{CN}^{K_{VC2}} \tag{4.55}$$

$$Mass_C = K_{pC0} \cdot Vol_C^{K_{pC1}} \tag{4.56}$$

$K_{VC0}, K_{VC1}, K_{VC2}, K_{pC0}andK_{pC2}$ are proportionality regression coefficients taken from reference capacitor technology.

4.4.3 Capacitance and capacitor voltage and current

The design of the DC-link voltage $V_{DC,N}$ is, as previously stated, simply related to the line-to-line AC voltage $V_{LL,N}$, the modulation index M_S and the scaling factor K_{mod} as:

$$V_{DC,N} = \frac{V_{LL,N}}{\sqrt{3} \cdot K_{mod} \cdot M_S} \tag{4.57}$$

Further, the DC-link capacitance is derived in [24] to (4.58), where P_N is the nominal power of the capacitor.

$$C_{DC} = \frac{P_N}{V_{DC,N}^2 \cdot (\delta_{Vdc} + 0.5 \cdot \delta_{Vdc}^2) \cdot f_{sw}} \tag{4.58}$$

As these parameters are obtained, the dielectric power losses, the volume, and the mass can be calculated. However, the resistive losses from (4.54) are dependent on the RMS value of the capacitor current $I_{C,RMS}$. This current needs, according to Kirchoff's current law, to be defined from the input current $I_{in,AC,RMS}$ to the capacitor and the current $I_{vsc,AC,RMS}$ entering the voltage source converter. If it is assumed to be pure AC currents with no common harmonics, the current stress on the capacitor can be expressed as:

$$I_{C,RMS}^2 = I_{vsc,AC,RMS}^2 + I_{in,AC,RMS}^2 \tag{4.59}$$

The two contributions can, according to [24], be expressed by (4.60) and (4.61).

$$I_{vsc,AC,RMS}^2 = \frac{\sqrt{6} \cdot K_{mod} \cdot M_S}{\pi} \cdot \left[1 + \left(4 - \frac{3\sqrt{6}\pi \cdot K_{mod} \cdot M_S}{2}\right) \cdot \cos^2 \phi\right] \cdot I_a^2 \tag{4.60}$$

$$I_{in,AC,RMS} = \delta_{Iin} \cdot I_{in,AVG} \tag{4.61}$$

These expressions are related to the displacement factor $\cos\phi$ and δ_{Iin}, which is the ratio of the RMS ripple component to the DC component of the DC-link input current and the average input current $I_{in,AVG}$ can be expressed by:

$$I_{in,AVG} = I_{vsc,AVG} = 3 \cdot (I_{t,AVG} - I_{d,AVG}) = 3 \cdot K_{mod} \cdot M_S \cdot \cos\phi \cdot I_a \tag{4.62}$$

$I_{t,AVG}$ and $I_{d,AVG}$ are here the average IGBT and diode currents respectively.

4.5 Total losses, volume and mass of the evaluated system

When equations obtaining the power losses, volume and mass of the converters, inductors, and capacitors are introduced, the equations for overall values of these parameters can be defined. First, the power losses must be obtained for both the IGBTs and diodes by adding the corresponding losses, according to (4.63) and (4.63).

$$P_{IGBT} = P_{cond,IGBT} + P_{sw,on,IGBT} + P_{sw,off,IGBT} \tag{4.63}$$

$$P_{diode} = P_{cond,diode} + P_{sw,off,diode} \tag{4.64}$$

From this, the total losses from the six valves in a two-level voltage source converter can be found by (4.65), taking the number of series- or parallel-connected devices into consideration.

$$P_{loss,VSC} = 6 \cdot n_s \cdot n_p \cdot (P_{IGBT} + P_{diode}) \tag{4.65}$$

Analogous, the inductor and capacitor losses are found by summing the winding and core losses, and the dielectric and resistive losses respectively, as seen from (4.66) and (4.67).

$$P_{loss,L} = P_{wL} + P_{coreL} \tag{4.66}$$

$$P_{loss,C} = P_{\epsilon C} + P_{\Omega C} \tag{4.67}$$

Finally, the total losses of the studied components are found by (4.68).

$$P_{loss,total} = P_{loss,VSC} + P_{loss,L} + P_{loss,C} \tag{4.68}$$

In the same way, the volume and mass for the studied components must be summarised to obtain the total value. This is shown in (4.69) and (4.70), where C_{PV} is the volume utilisation factor.

$$Vol_{total} = \frac{1}{C_{PV}} \cdot (6 \cdot Vol_{valve} + Vol_L + Vol_C) \tag{4.69}$$

$$Mass_{total} = 6 \cdot Mass_{valve} + Mass_L + Mass_C \tag{4.70}$$

4.6 Summary

In this chapter, the background theory for investigating the η, ρ, and γ is laid out. The different modulation techniques are briefly explained. Mainly, the calculations of power losses, volume, mass, as well as relevant currents and voltages for the semiconductor switch valves, inductors, and capacitors are given, primarily based on [24].

Particular emphasis is given to the semiconductor calculations, as this is what is changed the most during the different designs. The same inductor and capacitor are used for all possible arrangements studied, and the parameters and coefficients for all these devices are found in Appendix A.

Chapter 5

Case studies

In this chapter, the case studies performed are presented. In this way, the configurations can be compared at different criteria, providing a wider space of possible solutions. Consequently, the size and number of clusters are varied, as well as modulation methods and machine size. Adequate recommendations should be provided after investigating these selected alternatives.

The chapter starts with a section about the design of the configurations. Here are specific parameters for the system and the converters presented, as well as assumptions that yield for all analyses. Furthermore, the cases 1-5 are presented one by one. They all include descriptions and assumptions specific for that case, results, and analysis. Finally, the cases are compared to each other to draw some essential conclusions and recommendations. The cases studied are:

- Case 1: Clusters consisting of three turbines rated at 444 kW, using the SPWM method.
- Case 2: Clusters consisting of three turbines rated at 444 kW, using the SVPWM and SFTM methods.
- Case 3: Expanded cluster size to five turbines rated at 444 kW, using the SPWM and SFTM methods.
- Case 4: Clusters consisting of three turbines rated at 750 kW, using the SPWM and SFTM methods.
- Case 5: Series connection of the DC cluster, consisting of three, four, and five turbines rated at 444 kW, using the SPWM method.

In case 1, individual plots of the power losses, volume, and mass are included to point out and better understand relationships. In case 2, these plots are included

in the Appendix. For the remaining cases, only the critical indicator parameter plots are included in the results.

5.1 Design of the configurations

Throughout the case studies, the configurations are changed, mainly concerning the size of clusters and the size of machines. However, some fixed parameters are used, and these are presented in this section. How to design the switch valves is explained, and moreover, it is established how the limit in inductance affects the lower limit in switching frequency. Finally, some general assumptions for the study are laid out.

5.1.1 System parameters

There are some constraints to consider when it comes to the parameters of the multi-rotor system. As mentioned, [8] operates intending to produce a total of 20 MW by dividing into 45 small rotors of 444 kW. The report mentioned above provides some remarks regarding machine voltage, frequency, power factor, and equivalent machine reactance. These values are taken into consideration and presented in Table 5.1. These values are mostly used throughout the whole study, except the nominal machine power, which in case 4 is increased to observe how this affects the configurations.

Table 5.1: System parameters

Parameter	Symbol	Value
Nominal power	P_N	444 [kW]
Nominal RMS voltage	$V_{LL,N}$	690 [V]
Nominal frequency	f_N	50 [Hz]
Power factor	$\cos\phi$	0.85
Equivalent machine reactance per phase	L_M	0.15 [p.u.]

Other design parameters such as different safety factors and constraints which are necessary for a realistic design and which are contained in the equations presented in Chapter 4, are taken from the recommendations provided in [24]. These are typical and standardised values for these parameters and can be seen in Table 5.2. They are kept at these values for all simulations, and the only parameter that varies is the over-voltage factor which is changed between 1.15 and 1.1 depending on if the SPWM or SVPWM/SFTM respectively is used.

Table 5.2: Design parameters and constraints

Parameter	Symbol	Value
Overload factor	k_{olf}	0.3
Volume utilisation factor	C_{PV}	0.7
Relative input DC-link current ripple	δ_{IiL}	0.3
Nominal modulation index	$M_{S,nom}$	0.99
Ambient temperature	T_{amb}	40 [C]
Over-voltage factor	k_{ovf}	1.15 / 1.1
Safety factor for DC voltage	k_{vdc}	0.7
Safety factor for peak voltage	k_{vp}	0.8
Safety factor of thermal design	K_{SFT}	0.85
Max. relative inductor voltage	$\delta_{VL,max}$	0.3
Max. relative heat sink volume	$\delta_{HS,max}$	8
Max. relative AC current ripple	$\delta_{iL,max}$	0.2
Max. Relative DC link ripple	$\delta_{Vdc,max}$	0.02

The maximum relative AC current ripple $\delta_{iL,max}$ is set to 20 %. This is a high value and additional inductive filters in the configuration are required to limit the ripple to acceptable values. Additional filters are not analysed in this work but discussed in Chapter 6.

5.1.2 Design of semiconductor devices

In the design of the switching devices, the required blocking voltage, and the maximum current the devices can withstand are two of the most important considerations. The semiconductor modules have a given rating, and their current and voltage rating should not be surpassed. In the case of the blocking voltage, some safety factors are used in order to ensure reliability. An over-voltage factor k_{ovf} secures operation under over-voltages and is usually set to 1.1 for systems with line-to-line RMS voltage under 1 kV and 1.15 for systems with a higher voltage [42]. In addition, also the safety factors k_{vp} and k_{vdc} for peak AC and DC voltage respectively are present. Typical values for these factors are 0.75-0.85 for the peak voltage and between 0.6 and 0.7 for the DC voltage [24]. This results in, if the semiconductors are not connected in series, the following expression for the minimum DC blocking voltage $V_{block,min}$ [24]:

$$V_{block,min} = \begin{cases} \frac{V_{DC,N} \cdot k_{ovf}}{k_{vdc}} & \text{for } \delta_{Vdc} \leq 2 \cdot \left(\frac{k_{vp}}{k_{vdc}} - 1 \right) \\ \frac{V_{DC,N} \cdot k_{ovf} (1 + \frac{\delta_{Vdc}}{2})}{k_{vp}} & \text{for } \delta_{Vdc} > 2 \cdot \left(\frac{k_{vp}}{k_{vdc}} - 1 \right) \end{cases} \tag{5.1}$$

The maximum peak current I_{psw} considers an overload factor k_{olf}, normally of 30 %, and the current ripple δ_{iL}. This maximum peak current that the device must withstand is then expressed in [24] as:

$$I_{psw} = \sqrt{2} \cdot I_a \cdot \left(1 + \frac{\delta_{iL}}{2}\right) \cdot (1 + k_{olf}) = \sqrt{\frac{2}{3}} \cdot \frac{P_N \cdot \left(1 + \frac{\delta_{iL}}{2}\right) \cdot (1 + k_{olf})}{V_{LL,N} \cdot \cos\phi} \tag{5.2}$$

The switch valves should be designed to meet these criteria. If the maximum peak current is higher than the allowable current from one device, this can be overcome by adding an extra device in parallel until the desired rating is met. Obviously, extra elements have an impact on the volume and energy density, as is shown later. Moreover, the required design may also have to be modified according to switching frequency. As higher switching frequency leads to higher power losses and energy dissipation, this increases the temperature in the device. To maintain a high enough thermal resistance, also the number of parallel connected devices can be increased to reach this. This is well modified by the physical characteristic of each configuration, as is shown later in this chapter. With the rated current I_n of a given module and a demanded peak current I_{psw}, the minimum number of parallel connected devices $n_{p,min}$ is given by [24]:

$$n_{p,min} = \left[\left(\frac{I_{psw}}{1.6 \cdot I_n} - 1\right) \cdot \left(\frac{1 + \delta_{CI}}{1 - \delta_{CI}}\right) + 1\right] \tag{5.3}$$

In 5.3, δ_{CI} is the current imbalance which occurs since the modules are never exactly equal.

The switch valve must also be able to withstand the required blocking voltage. This does not need to be done by employing modules with higher voltage rating, but also by a series connection of modules. Adding one extra module in series increases the possible voltage with the rating of the module, which makes it possible to dimension for high voltages.

If the switching losses result in too little thermal resistance, also more series connected modules can be connected to overcome this challenge. Thus, the minimum required number of series-connected devices depends on the blocking voltage of the device V_{block}, the maximum DC voltage V_{DC} and the maximum phase voltage $\hat{V}_{LL}$. Besides, also the peak voltage and dc voltage safety factors k_{vp} and k_{vdc} influences the design, as these are meant to protect from overshoot voltages at turn-off. The expression for the minimum number of series-connected devices $n_{s,min}$ can be seen

in (5.4) [24].

$$n_{s,min} = max\left\{\frac{\hat{V}_{LL}}{k_{vp}\cdot V_{block}};\frac{V_{DC}}{k_{vdc}\cdot V_{block}}\right\} \tag{5.4}$$

In the study, mostly parallel connections are used. Therefore, the required blocking voltages and possible devices are presented here while the data for the series connections are presented in the relevant case, case 5.

In (4.57) it is shown that the DC voltage is dependent on which modulation technique is used. By investigating the two different scaling factors K_{mod} presented, it is found that the SPWM results in a higher DC voltage than the SVPWM and SFTM, due to the nature of the modulation techniques. By using the standard values presented in Table 5.1 and 5.2, the required minimum blocking voltages needed are $V_{block,min} = 1.870$ kV for the SPWM and $V_{block,min} = 1.549$ kV for the SVPWM and SFTM. As one standardised and intensely commercially available voltage rating of semiconductor modules is 1.7kV [43], this rating can be used when the SVPWM and SFTM methods are utilised. However, for the SPWM module with the required voltage rating beyond 1.7kV, there is a sudden change in voltage rating of the device that must be used, and this impacts the system design and the obtained results.

As the next standardised and excessively commercial available semiconductor devices are rated at 3.3 kV [43], this rating is used for the SPWM method. As these are presented with their respective needed calculated coefficients in [24], the 3300V x 1500A module from Infineon [44] and 1700V x 3600A module from Infineon [45] are used here. The parameters and coefficients used in the calculations can be found by their respective datasheets ([44, 45]) and are presented in Figure A.1 in Appendix A. Devices rated at 2.4 kV are also commercially available, but not to the same extent. Due to scope limitations, this module is not implemented in this analysis. However, these would probably be a better fit with the requirements in the SPWM simulations, which needs to be kept in mind when analysing the results.

5.1.3 Limit in inductance

In the case of the machine reactance, from Table 5.1, it has a value of 0.15 p.u., which corresponds to an inductance larger than the phase reactor inductance calculated by (4.48). Due to this, a phase reactor at the machine side of the converter is not needed. This is assumed to yield for the rest of the study.

Meanwhile, at the collector side of the converter, the phase reactor is necessary and represents a large proportion of the total mass and volume of the components studied. For too low switching frequencies, the design inductance from (4.48)

surpasses the limit inductance given from (4.49). This limit frequency changes depending on which modulation technique is used. The limit frequency, however, is the same for one given configuration, while the inductance is different. This relationship for the AC cluster, with both the limit inductance, the SPWM inductance, and the SVPWM/SFTM inductance is illustrated in Figure 5.1.

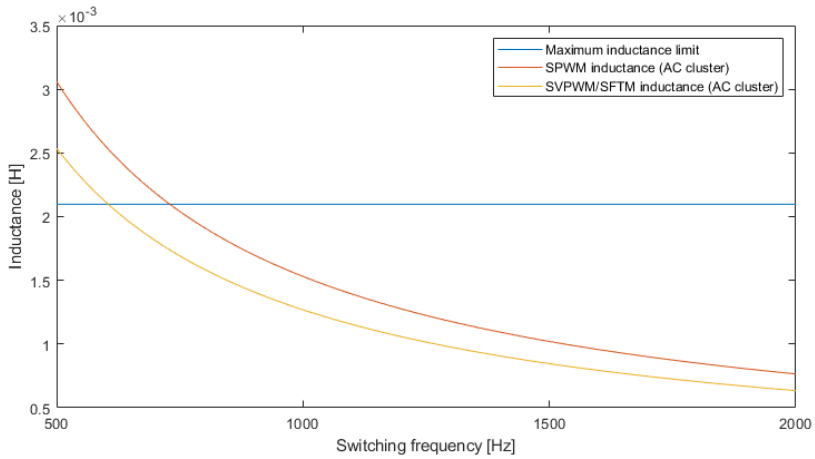

Figure 5.1: Design inductance intersection with maximum inductance.

By inspecting the intersection with the maximum inductance limit, by putting (4.48) equal to (4.49), a limit in the switching frequency is obtained. Hence, it is useless to investigate switching frequencies beneath this limit. For the SPWM, the intersection is at a bit higher than 700 Hz, while the SVPWM/SFTM limit is at around 600 Hz. These values will, therefore, be used as lower limits further in the analysis.

When comparing the equations for the inductance and the limit inductance in (4.48) and (4.49), it is observed that the limit is independent of power or any other configuration-dependent parameter. This means that the DC and the hybrid cluster have other values for maximum inductance and inductance, but these intersect at the same point as in Figure 5.1.

5.1.4 Common assumptions for the case study

- All the calculations are performed on one individual cluster. To compare the configurations on a system level, it is, therefore, assumed that all clusters are identical.
- To perform reasonable comparisons when only one cluster is studied, other

components such as transformers, filters, and protective gear are excluded from the study.

- The internal cables are neglected in the study since they do not have a great impact on the system level perspective.
- The study does not include the design of the electric machine in order to limit the scope and have a fair comparison between all the configurations. The machine is assumed to provide the nominal power P_{nom}.
- The calculations are performed for the rated power P_{nom} for all devices. Thus, power losses at earlier stages are not considered. This assumption simplifies the system, but the effects are quite small and affecting all configurations similarly.
- The configurations are designed for the worst case operating scenario. Thus the design for the maximum losses which occur at the maximum junction temperature is studied. Hence, the junction temperature is kept constant at its maximum value, i.e. $T_j = T_{j,max}$.
- To weigh up for the mismatch in voltage rating of some configurations compared to semiconductor ratings, the loss calculations are performed with the actually required blocking voltage. This is done to show the potential if a wider selection of semiconductor devices would be available. Doing so influences the results for all parameters, but in the same way for all configurations in each case study. Thus, this makes the comparisons more reasonable and gives better convergence in the calculations.

5.2 Case 1: Frequency sweep using SPWM

In the first case, *clusters of three turbines* are studied. The machines used have an assumed *power of 444 kW*, and the *SPWM method* is used. All the parameters from Table 5.1 and 5.2 are used as they are presented, with an over-voltage factor of 1.15.

A frequency sweep is performed, ranging from the limit frequency at 700 Hz until 1800 Hz. At this frequency, all the performance indicators are beneath their previous maximum values and continue to decrease.

In this section, first, the assumptions are presented in order to analyze this case. The results of the analysis are presented using both tables and plots to see the key indicators and significant differences clearly. A comparative analysis is performed,

where the optimum frequency for all configurations and the corresponding parameter values before a Pareto analysis is presented, showing the possible solutions and Pareto front when the three key parameters are plotted versus each other.

5.2.1 Assumptions in case 1

In the AC cluster, each generator connects to a back-to-back converter, with their individual DC capacitor and phase reactors before they are connected in a cluster. Then, after the connection, several clusters may share components such as LC filters, transformers, and cables. This results in 15 clusters of three wind turbines, which means a total of 90 individual converters.

The DC cluster, which shares the collector-side converter with the three turbines in the same cluster, obviously has a lower number of needed converters. Other components may be shared similar as in the AC cluster, but this connection reduces the number of DC capacitors and phase reactors by two thirds. In addition, 45 rectifiers and 15 inverters are required, resulting in a total reduction of converters by one third.

The hybrid cluster, where the generators are connected before the shared back-to-back converter, has even more savings in terms of converters. The total of 15 clusters which, in this scope, only need two converters each, results in a total of 30 converters. The filters, transformers, and cables are assumed shared in the same way as the other configurations.

The total power of one investigated cluster will, in this case, be equal $P_{cluster} = 3 \cdot P_{nom} = 1.332$ MW. From this, calculations are performed, based on the above-mentioned methodology, to obtain the performance indicators for the cluster. When this is obtained, the systems total losses, mass and volume can be found by multiplying with the number of clusters.

In all the configurations, parallel connections are performed, keeping the voltage constant. Using the SPWM, the DC voltage and the minimum required blocking voltage are calculated to be $V_{DC} = 1.138$ kV and $V_{block,min} = 1.870$ kV. Because of this, the module with the rating of 3300V x 1500A from Infineon [44] is selected.

The configurations differ from each other, mainly in the requirements of the semiconductors. As a parallel connection is used, an increase in the current occurs. However, for the AC cluster, the treated current within this scope is all over the same, making the 3300V x 1500A module overrated, and the need for extra modules occurs at a high switching frequency.

For the DC and hybrid clusters however, the shared converters experience three times the current, making the maximum peak current higher than the module is capable of. Then, the number of parallel connected modules needs to be designed higher. Summarised in Table 5.3 are the peak currents and the minimum required

number of parallel connected devices for the switch valve.

Table 5.3: Semiconductor module, peak current and required parallel connected modules for the topologies using SPWM.

	Semiconductor module	I_{psw}	$n_{p,min}$
AC cluster rectifier	3300V x 1500A	883.9 A	1
AC cluster inverter	3300V x 1500A	883.9 A	1
DC cluster rectifier	3300V x 1500A	883.9 A	1
DC cluster inverter	3300V x 1500A	2651.7 A	2
Hybrid cluster rectifier	3300V x 1500A	2651.7 A	2
Hybrid cluster inverter	3300V x 1500A	2651.7 A	2

5.2.2 Results of case 1

The results for the three configurations are shown in Figure 5.2 - 5.4, and present the power losses, volume and mass one by one.

In terms of the power losses, which are illustrated in Figure 5.2a, 5.3a and 5.4a, it is clear that the switch valve losses are the dominant. The inductor losses, in green, are quite constant in every configuration, but lower for the DC and hybrid clusters, as the higher rated power gives smaller inductance (confer 4.48). The capacitor losses, in purple, are for all configurations under 0.3% and thus negligible.

Concerning the AC cluster, the point in switching frequency where an extra module is needed occurs at around 1515 Hz for the inverter and 1580 Hz for the rectifier. At this frequency, the power losses increase drastically.

For the DC cluster, this point is at 1190 Hz for the inverter and 1580 Hz for the rectifier. As can be seen, the effect of adding another module at the inverter does not impact as much as for the rectifier.

This effect also comes clear in the hybrid cluster. When connecting additional modules at 1190 Hz and 1290 Hz for the inverter and rectifier respectively, this does not influence more than a jump of about 1 percentage point.

This trend is also visible for the volume and mass in Figure 5.2 - 5.4 (b) and (c). When the extra modules are needed, there is a jump in both volume and weight for the configurations. This jump is, when combining the three machines, smaller for the hybrid cluster and the shared converter in the DC cluster than the other converters.

The inductor volume and mass decrease with increasing switching frequencies in a similar shape for all the configurations. However, this effect is after a while, outweighed by the addition of modules. This behaviour creates a minimum point for the volume and mass, where the design point may be centred around.

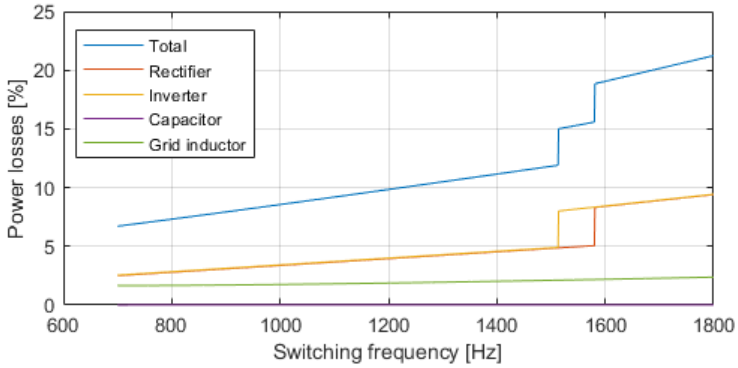

(a) Power losses

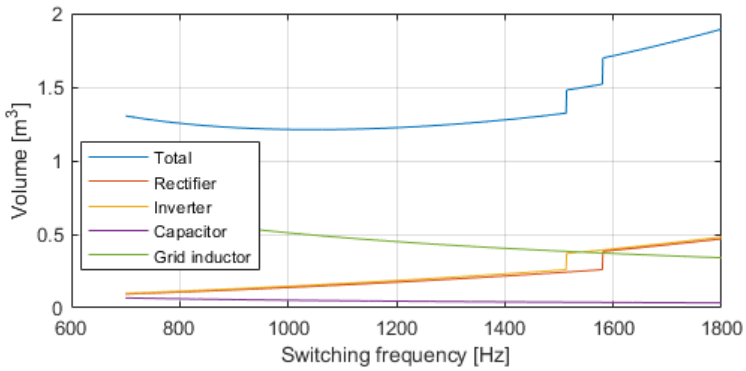

(b) Volume

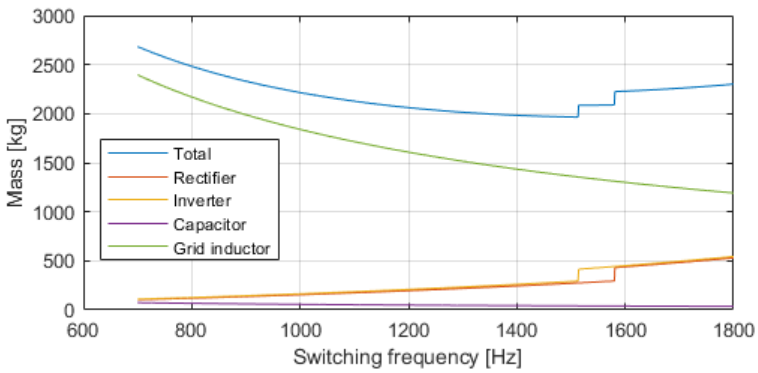

(c) Mass

Figure 5.2: Power losses, volume and mass for the AC cluster using SPWM.

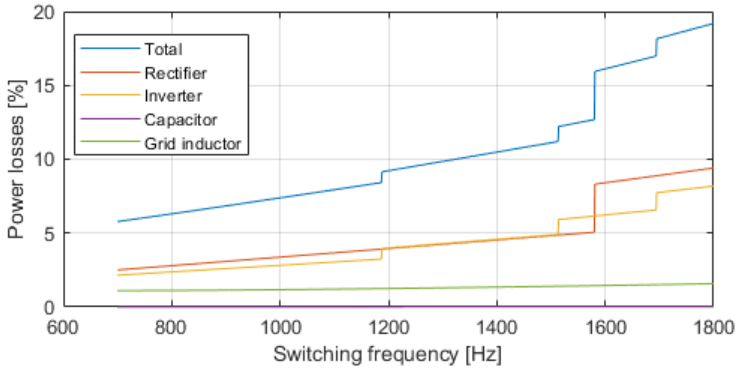

(a) Power losses

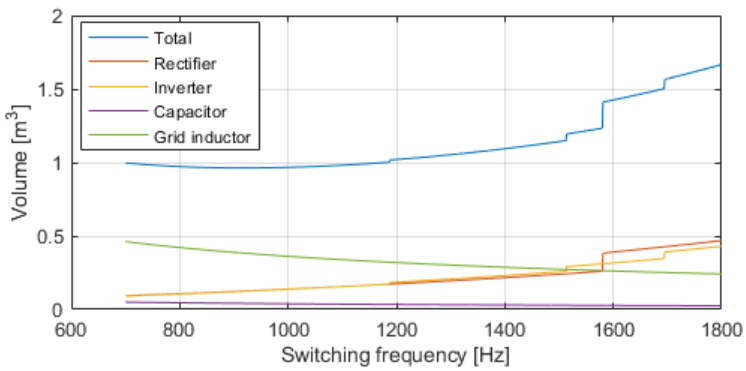

(b) Volume

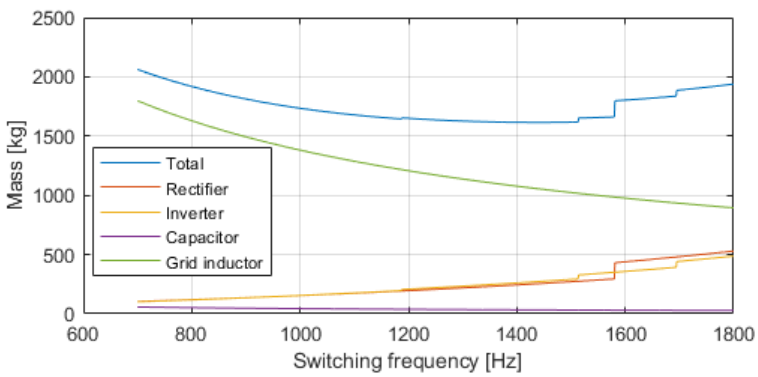

(c) Mass

Figure 5.3: Power losses, volume and mass for the DC cluster using SPWM.

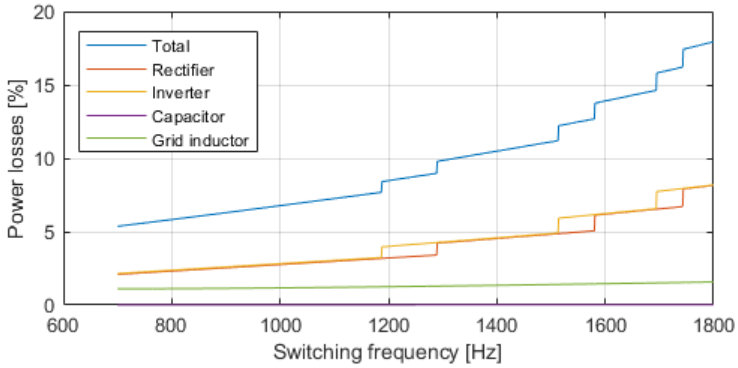

(a) Power losses

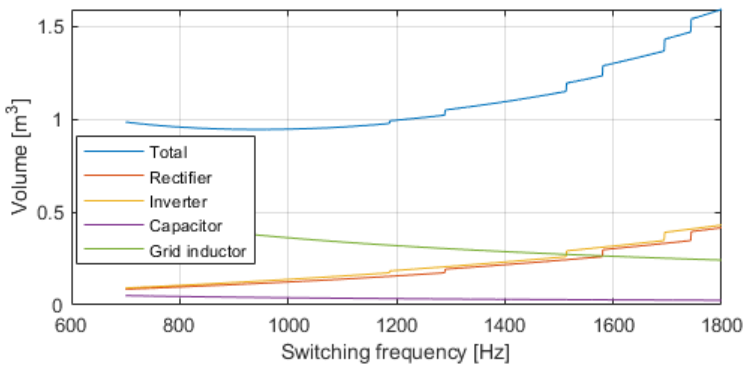

(b) Volume

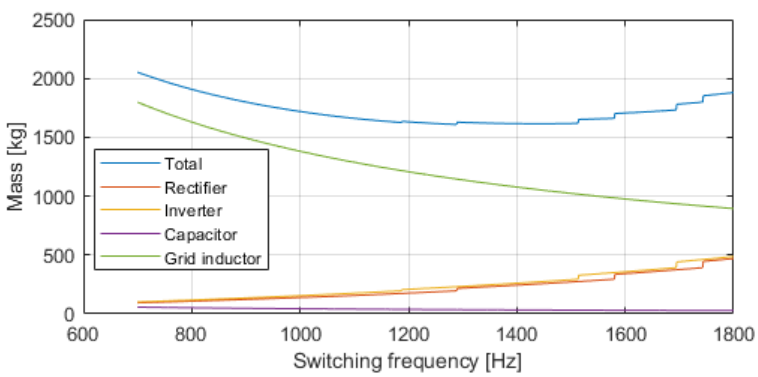

(c) Mass

Figure 5.4: Power losses, volume and mass for the hybrid cluster using SPWM.

5.2.3 Comparative analysis of case 1

To analyse the results and compare them with respect to each other, the performance indices defined in (3.1)-(3.3) are used. This gives the plots in Figure 5.5.

The plots show the power density and power-to-mass ratio at the left y-axis, and efficiency at the right y-axis. It is visible that after the connection of an additional parallel connected device, the performance decreases for all parameters in all configurations. To obtain the optimum switching frequency, a design where all these parameters perform well are the main interest. Analytically, when η, ρ and γ are weighted equally, the expression in (3.4) needs to be maximised. The maximum Λ, its corresponding switching frequency and parameters are summarised in Table 5.4.

Table 5.4: Maximum Λ values and its corresponding switching frequencies and performance indices at this point using SPWM.

	Λ_{max}	f_{sw}	η	ρ	γ
AC cluster	2.9195	1149 Hz	90.49 %	0.99 MW/m^3	0.58 MW/t
DC cluster	2.9337	1048 Hz	92.35 %	1.26 MW/m^3	0.72 MW/t
Hybrid cluster	2.9415	1078 Hz	92.85 %	1.30 MW/m^3	0.74 MW/t

The optimum switching frequency is located differently, and the values can be compared to the plot in Figure 5.5. At this optimum switching frequency, it is possible to obtain the total losses, volume, and mass for the whole 20 MW system. This can be obtained by simply calculating what the losses, volume, and mass would be, based on the η, ρ and γ values in Table 5.4 or multiplying the values from Figure 5.2-5.4 with the total number of clusters, as this is the results for one cluster and they are assumed equal. The total losses, volume, and mass are summarised in Table 5.5, showing the significant total impact of improving the performance indicators.

Table 5.5: Power losses, volume and mass at the given optimum frequency using SPWM.

	f_{sw} [Hz]	Losses [MW]	Volume [m^3]	Mass [t]
AC cluster	1149	1.902	20.20	34.38
DC cluster	1048	1.530	15.87	27.78
Hybrid cluster	1078	1.430	15.38	27.03

To investigate the performance indices in a more comparative manner, they are split into separate plots for efficiency, volume, and mass in Figure 5.6. Studying

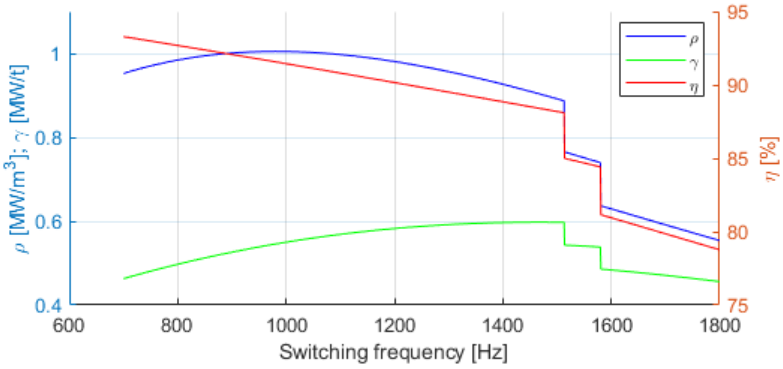

(a) AC cluster

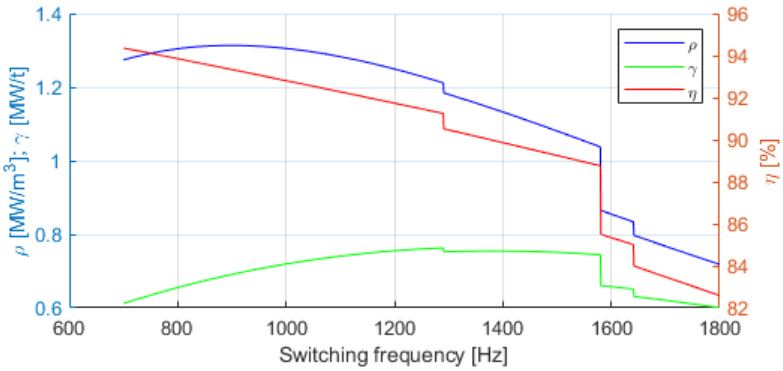

(b) DC cluster

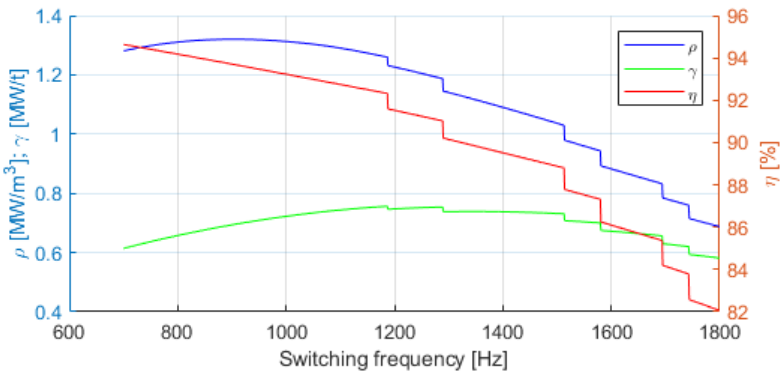

(c) Hybrid cluster

Figure 5.5: Key parameters for the three configurations using SPWM.

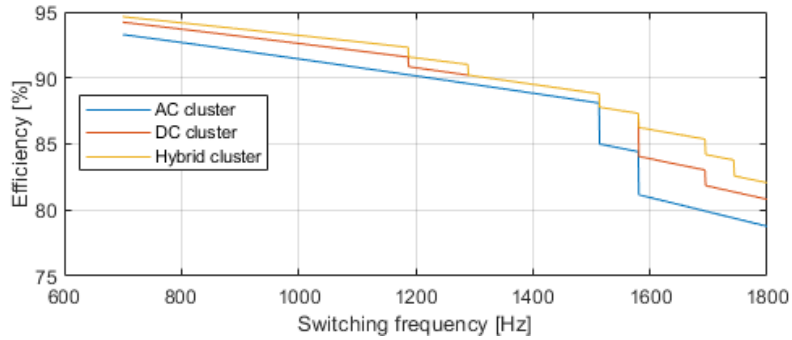

(a) Efficiency

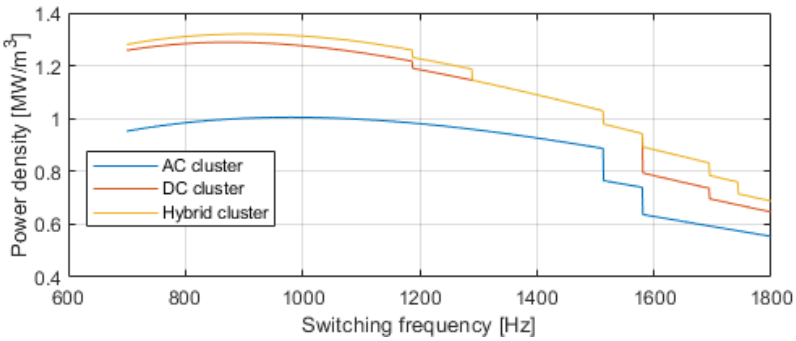

(b) Power density

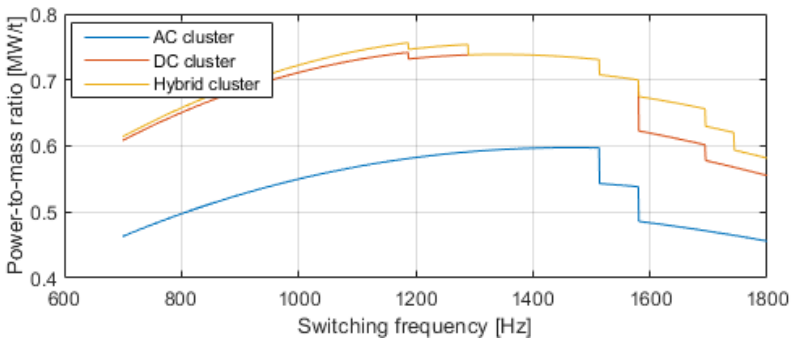

(c) Power-to-mass ratio

Figure 5.6: Comparison of key parameters for the topologies using SPWM.

the efficiency in Figure 5.6a, there is a linear reduction in efficiency for three configurations until the addition of a module. The addition influences each configuration differently. It is e.g., an increase by three modules in the AC cluster but only one for the hybrid cluster.

All three configurations have efficiency above 90 % for a longer period, which is expected for the total system of two power converters, capacitors, and inductors, keeping in mind that the worse case conditions are explored. In typical operation, the efficiency is higher. The hybrid cluster performs overall the best based on Figure 5.6a, closely followed by the DC cluster and then the AC cluster.

Concerning power density in Figure 5.6b, it is observed more substantial differences. The number of individual converters needed in the AC cluster, makes the volume needed higher than the two others, which has a reduced number of converters. This relationship also yields for the power-to-mass ratio in Figure 5.6c.

The consequences when adding parallel modules are similar as for the power losses, meaning sudden drops in performance. Both the ρ and γ experience maximum at different frequencies, but it is visible that the hybrid cluster performs the best, tight followed by the DC cluster, while the AC cluster is some steps behind with these indicators.

In Figure 5.7, the distribution of power losses in percentage for each configuration is illustrated. The pie diagrams coincide with the power loss plots in Figure 5.2a, 5.3a and 5.4a. The rectifier and inverter losses are both split into conduction and switching losses, to see how it is distributed. Besides, the plots presented are obtained at one specific switching frequency, the optimum switching frequency for optimising Λ, given in Table 5.4.

First of all, it is worth noticing that the losses summarise into different values, the same power as the total power loss line in Figure 5.2a, 5.3a and 5.4a at that specific switching frequency. The total losses are 126.8 kW for the AC cluster, 102.0 kW for the DC cluster and 95.4 kW for the hybrid cluster.

As the diagram shows, the capacitor losses (in purple) are negligible in all configurations. For the AC cluster, they equal 0.1 % while the hybrid cluster has the highest capacitor losses with almost 0.3 %. The dielectric losses, defined in (4.52) are low, as well as the resistance from (4.53). The resistive losses, however, are proportional with the capacitor current squared, which is higher for the configurations sharing the capacitor.

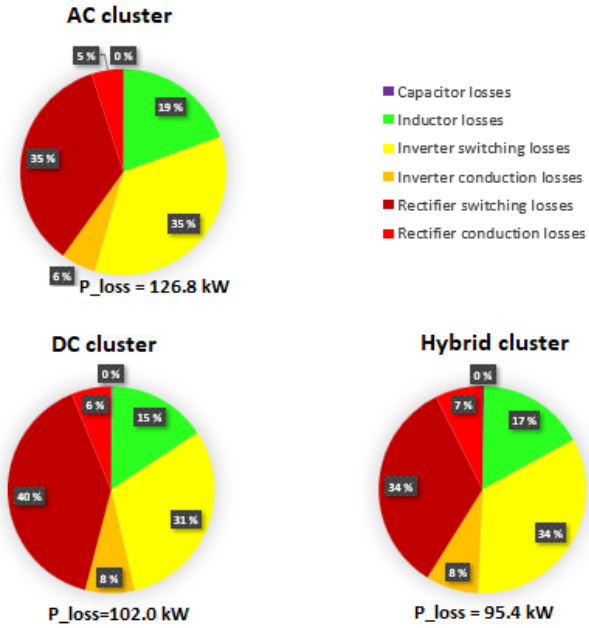

Figure 5.7: Distribution by percentage of the power losses for the three configuration in case 1. Total power losses given in kW.

The inverter conduction losses increase a bit, both in value and share when the collector side converters are replaced with one shared inverter, as from the AC cluster to the DC and hybrid clusters. The switching losses, however, are heavily reduced in value. As the total losses are lower for the DC and hybrid clusters, the share does not decrease that much, but in value, the switching losses are reduced by almost 25 % when combining three inverters to one larger, compared with having three separate ones as in the AC cluster. In total, the losses are reduced when inverters are shared.

This coherence also yields for the rectifier, when comparing the AC and hybrid cluster, where the AC cluster has three separate rectifiers, and the hybrid cluster, which has a rectifier shared by three turbines. The conduction losses increase a bit, but the switching losses are heavily reduced for the hybrid case.

Regarding the inductor losses, the values in the DC and hybrid clusters are very similar, with just a few percentage points in difference. This similarity is reasonable, as the inductance is equal. However, the AC cluster needs three times as many inductors, as they are placed right after the inverter but before the connection. This results in more inductors rated at a lower power. Thus, the inductor losses are higher and represent 19 % of the AC cluster power losses. In value, they are

about 50 % higher than the losses in the DC and hybrid configurations, which share inductors.

5.2.4 Pareto analysis of case 1

Pareto analysis is carried through for the three different configurations and can be seen in Figure 5.8. The power density is plotted against the power-to-mass ratio, where the red dots indicate the Pareto front for these two parameters. Besides, the efficiency is indicated by different colours from blue to yellow, where yellow represents the highest efficiency.

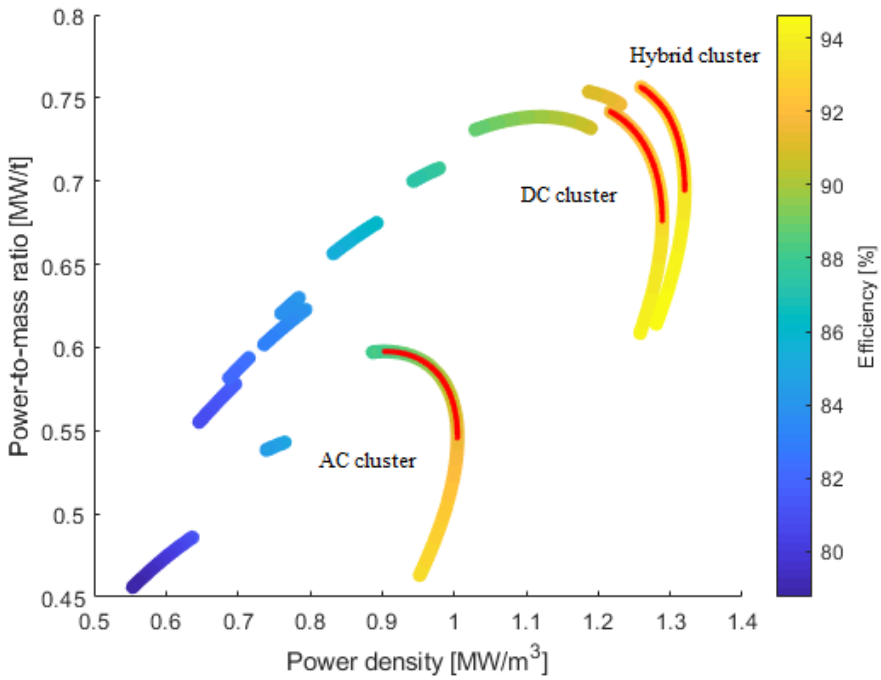

Figure 5.8: Pareto plot, power density versus power-to-mass ratio, with efficiency indicated by the colour bar for the SPWM.

It can be noted that the Pareto Front for all three configurations in the figure is close to coinciding with the maximum efficiency. This makes it possible to find design points keeping all three parameters at acceptable values, not far from the values found in Table 5.4.

The empty spaces without any data points represent the addition of modules. When this happens, steps in the parameters occur, and therefore, no valid solutions

on the $\rho - \gamma$ plot. Also, the Pareto front line is shifted to the right in all cases, indicating that the best design is where the power density is high. In all the cases, the Pareto front stops right before the first additional parallel connected module is inserted for one of the converters.

5.3 Case 2: Frequency sweep using SVPWM and SFTM

The second case is similar to the first case, with *three turbines per cluster* and a machine *power of 444 kW*. However, instead of the SPWM method, the *SVPWM and SFTM methods* are used in this case. Thus, the parameters from Table 5.1 and 5.2 are valid here, and the over-voltage factor of 1.1 is used. The change of modulation technique influences the system quite a lot since the modulation strategy changes the DC voltage and thus the design. Also, the limit inductance is changed, giving a lower-limit switching frequency of 600 Hz.

In the following sections, some assumptions relevant to the analysis of this case is presented. The results are presented using both tables and plots, before a comparative analysis is performed, finding the optimum switching frequency and corresponding parameters. The last section presents the Pareto analysis of the two different modulation techniques.

5.3.1 Assumptions in case 2

The assumptions made in this case are mainly the same as for case 1, including the same amount of converters for each configuration. The difference is the modulation strategies, as here a Space Vector Pulse Width Modulation (SVPWM) and a Symmetrical Flat-Top Modulation (SFTM) are used.

According to (4.3), these modulation methods lower the required DC voltage. It is now less than 1 kV, at $V_{DC} = 985.7$ V, which allows reduction of the over-voltage factor from Table 5.2 from 1.15 to 1.1. All this together influences the required blocking voltage of the module, which now is calculated by (5.1) to equal $V_{block,min} = 1.549$ kV. This again opens the opportunity to use modules rated for 1.7 kV, which are, to a great extent commercially available. Thus, the module selected in this case is a 1700V x 3600A from Infineon [45].

The rest of the case is, in principle, the same as for the first case. As the current rating of the applied module now is 3600 A, and the maximum peak current is the same as in the case 1, presented in Table 5.3, the device rating surpasses the maximum peak current possible in the three configurations. Moreover, since switching frequencies above 600 Hz are studied, the number of needed parallel con-

nected modules, $n_{p,min}$, has already increased before this limit is reached due to increased temperature from the power losses for the rectifier in the hybrid configuration, using SVPWM. The inverter, however, does not require additional modules before almost 800 Hz. This coincides with [24], where the rectifiers require additional modules at lower frequencies for lower rated modules as this 1700 V x 3600 A module. Thus, $n_{p,min} = 1$ for all configurations except the hybrid rectifier for SVPWM.

5.3.2 Results of case 2

The results for the SVPWM are shown in Appendix B. The plots demonstrate the same trends as in case 1. The AC cluster can operate at the highest switching frequencies before adding additional modules. The reason for this is that the modules that operate at higher total power dissipate more energy and quicker increase the temperature, which requires lower thermal resistance.

In Figure B.1, the power losses are shown, which are lower than for the SPWM. The inductor losses are lowest for the DC and hybrid clusters, as these inductors handle higher power than the AC cluster. The DC and hybrid clusters have at every point lower losses than the AC cluster.

The volume and mass in Figure B.2 and B.3 follows the same trend as for the SPWM, where there is a minimum point due to the increasing semiconductor volume and mass and decreasing inductor volume and mass for increasing frequencies. The steps in the higher rated modules are smaller than for the lower rated modules.

The results for the SFTM method are shown in Figure B.4-B.6 in Appendix B. The same trend is followed for this modulation method as for the previous ones. The total losses, volume, and mass are lower for the DC and hybrid clusters. Overall, this method performs similar to the SVPWM but slightly improved.

5.3.3 Comparative analysis of case 2

In order to analyse the results and compare them with respect to each other, the performance indices defined in (3.1)-(3.3) are used. This gives the plots in Figure 5.9 and 5.10 for the SVPWM and SFTM methods.

The plots in Figure 5.9 and Figure 5.10 show the power density and power-to-mass ratio at the left y-axis, and the efficiency at the right y-axis. An optimum switching frequency, where all these parameters are optimally performed, can be obtained in the same way as for Case 1 by use of the Λ-function. These values and corresponding parameters are summarised for the two modulation strategies in Table 5.6.

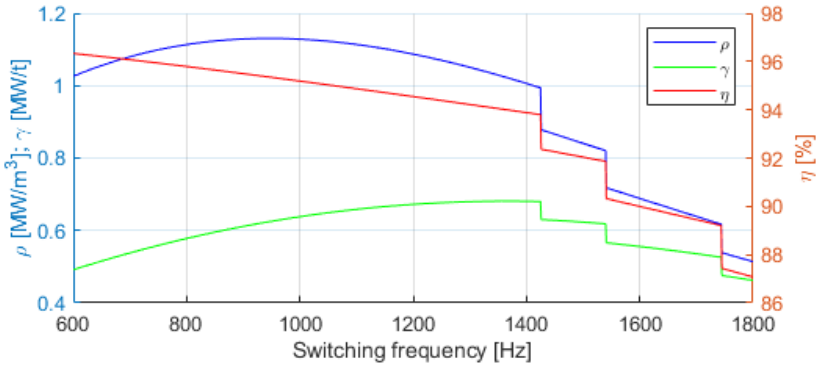

(a) AC cluster

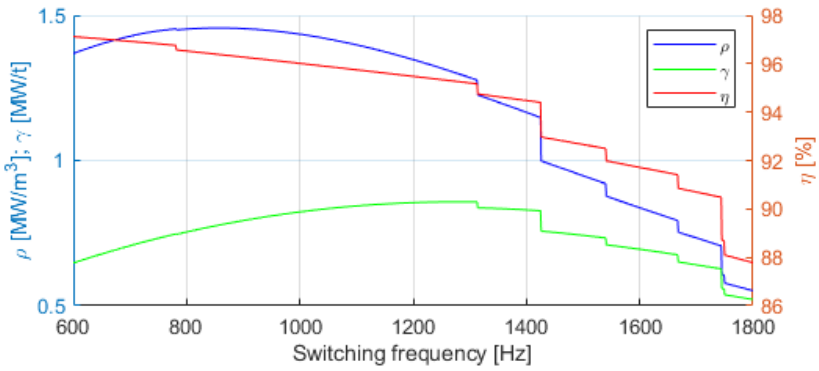

(b) DC cluster

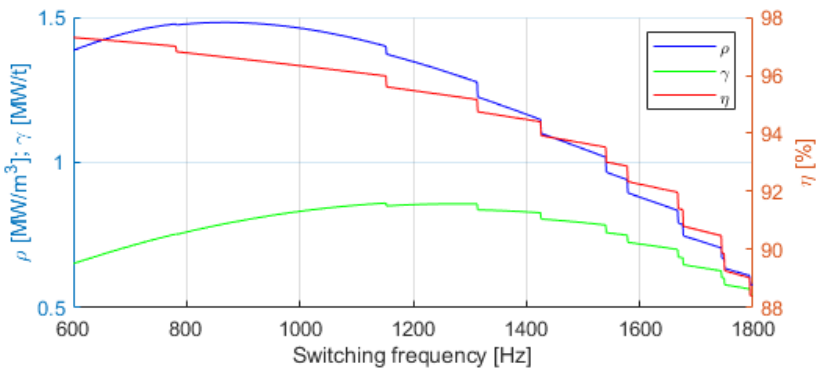

(c) Hybrid cluster

Figure 5.9: Key parameters for the three configurations, using SVPWM.

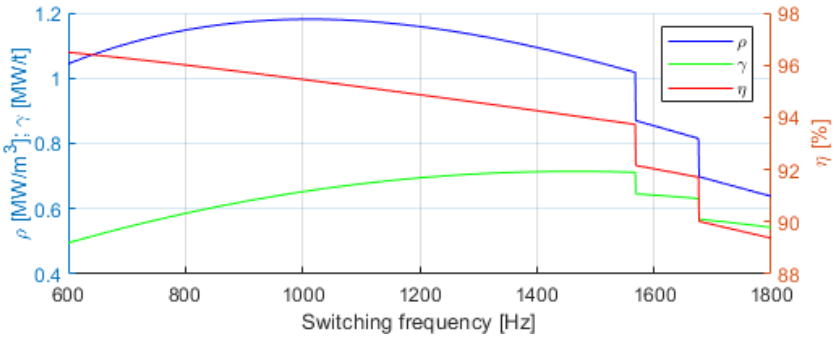

(a) AC cluster

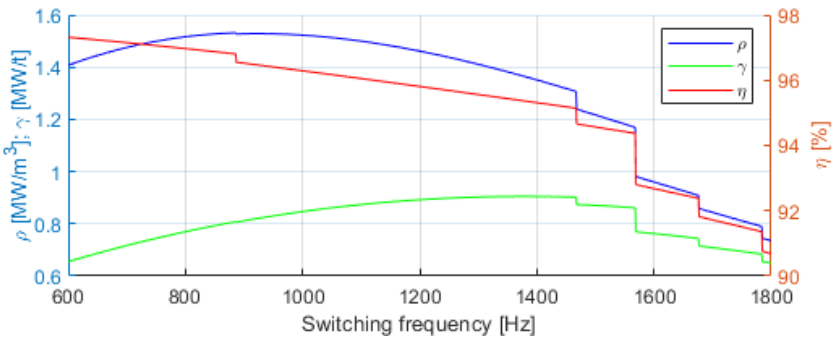

(b) DC cluster

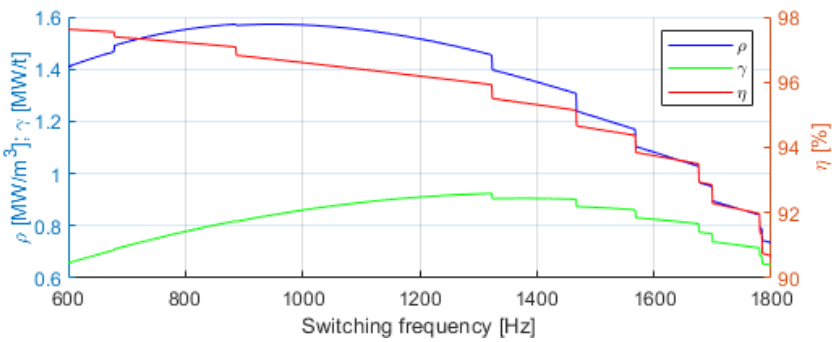

(c) Hybrid cluster

Figure 5.10: Key parameters for the three configurations, using SFTM.

Table 5.6: Maximum Λ values and its corresponding switching frequencies and performance indices at this point for the SVPWM and SFTM method.

	Λ_{max}	f_{sw}	η	ρ	γ
AC-C SVPWM	2.937	1116 Hz	94.82 %	1.11 MW/m^3	0.66 MW/t
AC-C SFTM	2.939	1194 Hz	94.88 %	1.16 MW/m^3	0.69 MW/t
DC-C SVPWM	2.937	1031 Hz	95.93 %	1.43 MW/m^3	0.83 MW/t
DC-C SFTM	2.934	1112 Hz	96.02 %	1.50 MW/m^3	0.88 MW/t
Hybrid-C SVPWM	2.947	1038 Hz	96.24 %	1.45 MW/m^3	0.84 MW/t
Hybrid-C SFTM	2.940	1140 Hz	96.31 %	1.54 MW/m^3	0.90 MW/t

Also, the performance parameters can be used to obtain the total power losses, volume, and mass which would occur for the parameters treated in the 20 MW multi-rotor system. These values are summarised in Table 5.7.

Table 5.7: Power losses, volume and mass at the given optimum frequency using SVPWM and SFTM.

	f_{sw} [Hz]	Losses [MW]	Volume [m^3]	Mass [t]
AC cluster SVPWM	1116	1.036	18.02	30.30
AC cluster SFTM	1194	1.024	17.24	28.99
DC cluster SVPWM	1031	0.814	13.99	24.10
DC cluster SFTM	1112	0.796	13.33	22.73
Hybrid cluster SVPWM	1038	0.752	13.79	23.81
Hybrid cluster SFTM	1140	0.738	12.99	22.22

For an easier comparison of the different performance indices, the plots are divided into one plot for each comparison parameter for the two strategies in Figure 5.11 and 5.12.

From these figures, it is clear that adding modules affects the AC cluster configuration more than the other two configurations, in the sense that this enforces a larger step in decreasing performance. However, this starts to happen at a higher switching frequency than the DC and hybrid configurations. Thus, for all the configurations, a meaningful design would be around 1000-1200 Hz in switching frequency, as this maintains good performance for all the configurations. This is confirmed by conferring Table 5.6.

When comparing the parameters for the two different modulation techniques used in this section, it comes clear that the SFTM performs slightly better. Studying the data in Table 5.6, the efficiency is about the same, but the power density and power-to-mass ratio are slightly higher for the SFTM than the SVPWM. This

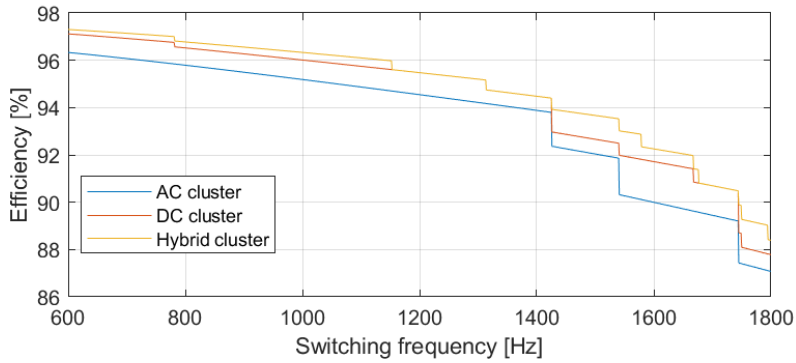

(a) Efficiency

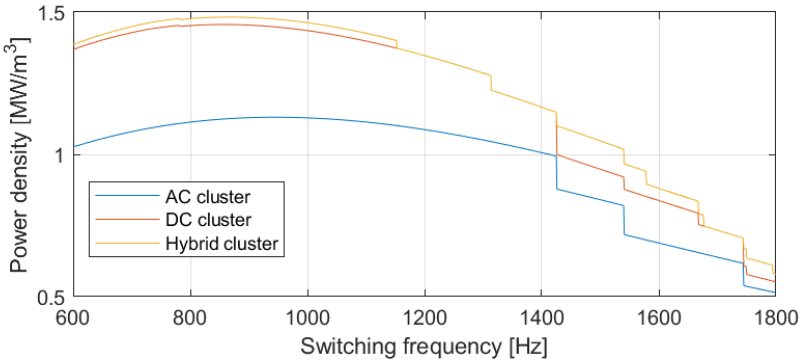

(b) Power density

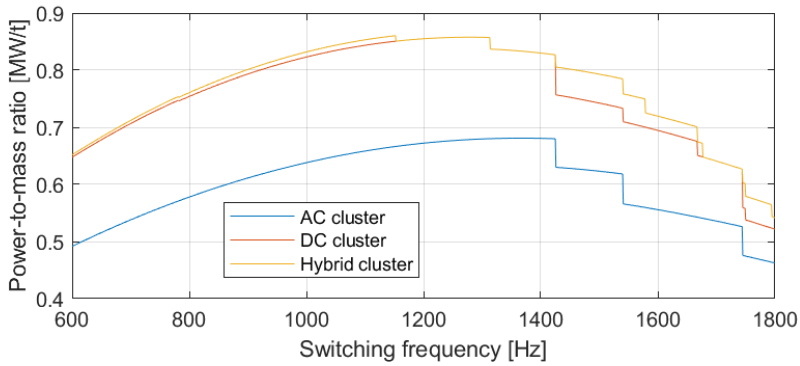

(c) Power-to-mass ratio

Figure 5.11: Comparison of key parameters for the topologies using SVPWM.

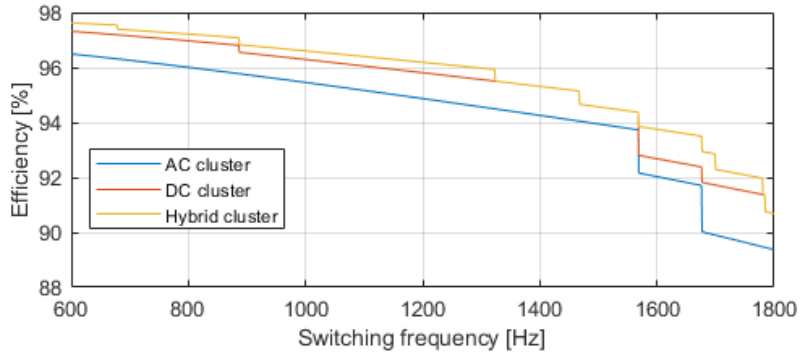

(a) Efficiency

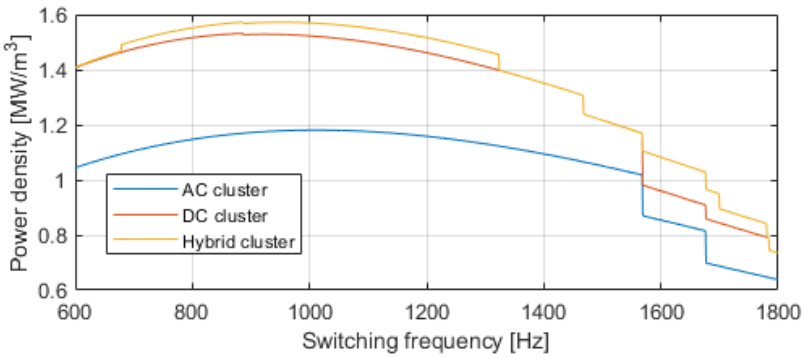

(b) Power density

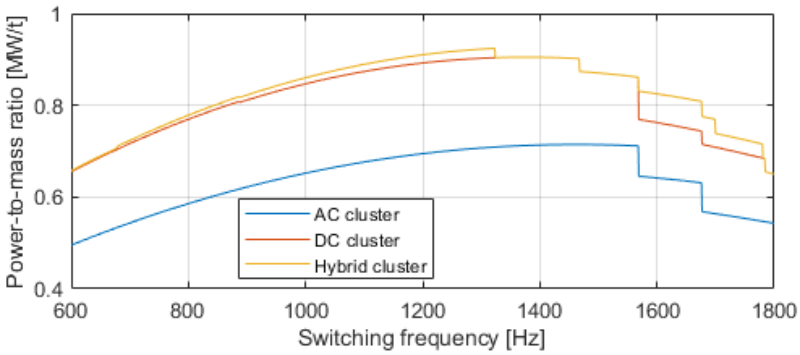

(c) Power-to-mass ratio

Figure 5.12: Comparison of key parameters for the topologies using SFTM.

is also visible from the plots in Figure 5.11 and 5.12.

Moreover, it is clear that the DC and hybrid clusters all over scores better than the AC cluster. Regarding efficiency, the difference is only a bit more than a percentage point, but regarding the power density and power-to-mass ratio, which are essential parameters for the multi-rotor system, there are significant differences, where the DC and hybrid clusters show a lot better performance. These two, however, are quite similar to each other with a slight advantage to the hybrid cluster all over.

5.3.4 Pareto analysis of case 2

Similar to the Pareto front in Case 1, this is carried out for the SVPWM and SFTM. The power-to-mass ratio γ is plotted against the power density ρ, and the red dots are showing the Pareto front between these two parameters. Besides, a colour bar presents solutions for the efficiency η, which enables an illustration of three parameters in a 2D plot. The results for each configuration for the two modulations methods can be seen in Figure 5.13.

When studying the AC cluster for the two modulation methods in Figure 5.13a and 5.13b, its Pareto front is clearly separated from the DC and hybrid clusters. The Pareto front coincides with an efficiency of about 95 % for both modulation methods, but it is observed that the AC cluster performs better with the SFTM method in Figure 5.13b.

The Pareto fronts of the DC and hybrid clusters are not that far from each other. It is clear that the hybrid cluster gains more advantages from changing to the SFTM from the SVPWM method than the DC cluster, as the space between increases. The Pareto front in both cases coincides with an efficiency of over 96 %. One can also observe that the Pareto front, except one point, starts after the first addition of a parallel module, represented by a small discontinuity.

By following the lines for the configurations in the direction of decreasing efficiency, and thus increasing switching frequency, it is observed that the SFTM has fewer additions of required parallel connected devices. Fewer additions make the decrease in both power density and power-to-mass ratio less steep for the SFTM method.

Due to the increased performance of all indicators at the Pareto front, it is clear to say that the SFTM method is the best of these to studied modulation techniques. Thus, the SFTM method is used further together with the less complicated SPWM method in case 3 and 4.

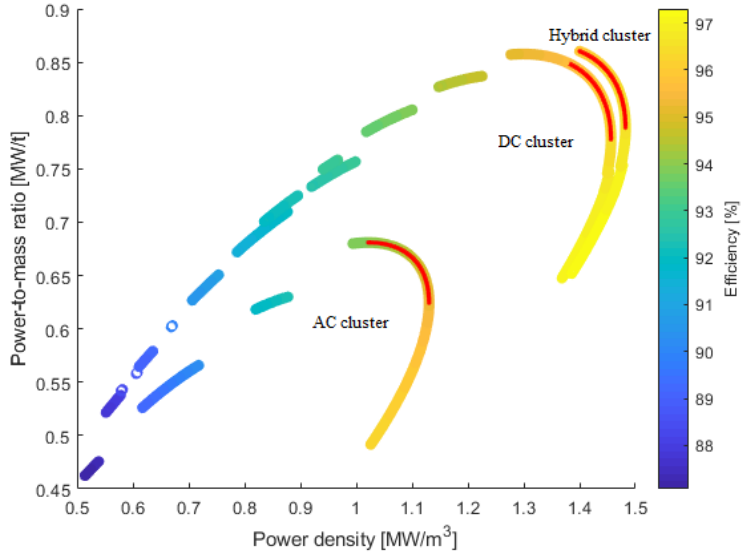

(a) SVPWM

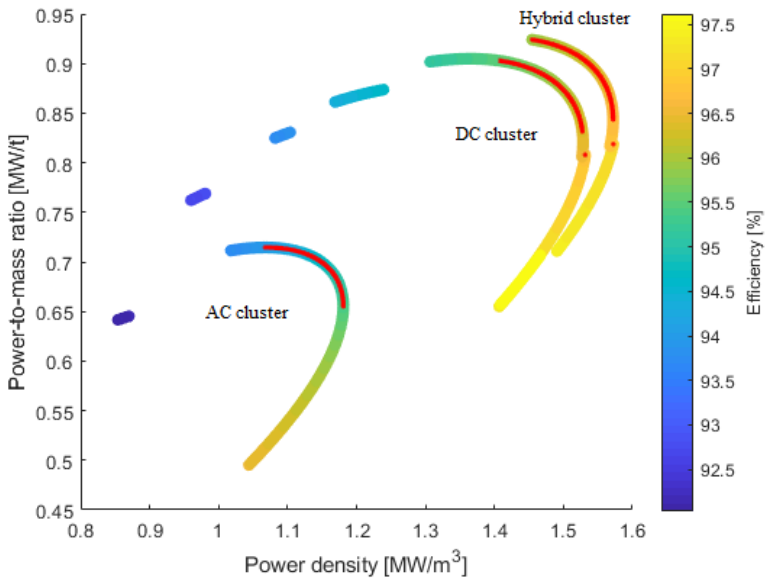

(b) SFTM

Figure 5.13: Pareto plot, power density versus power-to-mass ratio with efficiency indicated by colour bar for the SVPWM and SFTM.

5.4 Case 3: Expansion of clusters

Case 3 has the objective of studying the influence of a different number of turbines per cluster. From the previous cases, having three turbines per cluster, this number is now increased to *five turbines per cluster*, like in Figure 2.3b. A machine *power of 444 kW* is still assumed, and both the *SPWM and SFTM methods* are studied.

As the previous cases have shown that the SFTM method obtains the best results, this method is used in addition to the SPWM, which is easier to implement in a real application [46]. Therefore, the analysis is performed for these two methods.

This section, first, presents assumptions that stand out for this configuration. Second, results are presented for both modulation methods, before, finally, a comparative analysis and the Pareto analysis are presented.

5.4.1 Assumptions in case 3

For making the comparisons as good as possible, the same parameters as defined in Table 5.1 and 5.2 are used. Thus, the over-voltage factor k_{ovf} is different for the two modulations techniques studied, as the SPWM corresponds to a value of 1.15 and 1.1 for the SFTM. Also, the starting frequency from the performed frequency sweep is different, as explained previously in this chapter.

This way of connecting the multi-rotor system changes the required number of components. First of all, when the size of the clusters is increased to five wind turbines, only nine such clusters are needed to produce the desired 20 MW. This results in, as in the previous cases, a number of 90 converters, and the same number of DC-links and phase reactors for the AC cluster, but a reduced number of required AC filters, transforms and cables.

For the DC cluster, the number of rectifiers is 45, the same as before. However, the number of inverters, DC-links, and phase reactors reduce from 15 to 9, making a total of 54 converters. This reduction comes in addition to the decreased number of filters, transformers, and cables.

The hybrid cluster also has a decreased need for components, as now, in total, only 18 VSCs are required. The other components are decreased to the same number as for the other cases. This reduction is beneficial in terms of cost, but will most likely create challenges regarding control and more significant impact if one converter breaks down.

The addition of two turbines compared to Case 1 and case 2 affects the rating of the needed converters. As they are still connected in parallel, the required DC voltage remains the same, dependent on the modulation method. However, now the power of one cluster will equal $P_{cluster} = 5 \cdot P_{nom} = 2220$ kW, which influences the current.

The maximum peak current, which decides the number of needed parallel modules for the high-power converters, increases for the DC and hybrid clusters. For the AC cluster, this remains equal, as each machine interfaces a back-to-back converter. This is also the case for the rectifiers in the DC cluster. For the other converters, this value now equals 4419.5 A. The maximum peak current, type of module, and the corresponding need of parallel connected modules are summarised in Table 5.8.

Table 5.8: Semiconductor module, peak current and required parallel connected modules for the topologies using SPWM and SFTM with the increased cluster size.

	Module	I_{psw}	$n_{p,min}$
AC cluster rectifier SPWM	3300V x 1500A	883.9 A	1
AC cluster inverter SPWM	3300V x 1500A	883.9 A	1
AC cluster rectifier SFTM	1700V x 3600A	883.9 A	1
AC cluster inverter SFTM	1700V x 3600A	883.9 A	1
DC cluster rectifier SPWM	3300V x 1500A	883.9 A	1
DC cluster inverter SPWM	3300V x 1500A	4419.5 A	3
DC cluster rectifier SFTM	1700V x 3600A	883.9 A	1
DC cluster inverter SFTM	1700V x 3600A	4419.5 A	2
Hybrid cluster rectifier SPWM	3300V x 1500A	4419.5 A	3
Hybrid cluster inverter SPWM	3300V x 1500A	4419.5 A	3
Hybrid cluster rectifier SFTM	1700V x 3600A	4419.5 A	2
Hybrid cluster inverter SFTM	1700V x 3600A	4419.5 A	2

5.4.2 Results and comparative analysis of case 3

The Λ defined in (3.4) and the switching frequency giving these values are obtained, as well as the corresponding parameter values at this switching frequency. This is when all three parameters are weighted equally, and these values are presented in Table 5.9.

Comparing this case with the previous case, where each cluster was limited to three turbines in Table 5.4 and Table 5.6, some notes can be taken. First, the AC cluster experiences no change when increasing the number of turbines per cluster. This relation is trivial, as none of the studied components is changed, but just multiplied. However, for the DC cluster and hybrid cluster, there is a slight reduction in switching frequency where the Λ is optimised, in where the Λ-value is slightly increased. This also yields for the three parameters defined, they all increase at this optimum point when the cluster size is increased.

Table 5.9: Maximum Λ values and its corresponding switching frequencies and performance indices at this point for the SPWM and SFTM method with increased cluster size.

	Λ_{max}	f_{sw}	η	ρ	γ
AC-C SPWM	2.920	1149 Hz	90.49 %	0.99 MW/m^3	0.58 MW/t
AC-C SFTM	2.936	1194 Hz	94.88 %	1.16 MW/m^3	0.69 MW/t
DC-C SPWM	2.925	990 Hz	92.96 %	1.40 MW/m^3	0.79 MW/t
DC-C SFTM	2.939	1065 Hz	96.57 %	1.67 MW/m^3	0.97 MW/t
Hyb.-C SPWM	2.934	1028 Hz	93.50 %	1.43 MW/m^3	0.81 MW/t
Hyb.-C SFTM	2.947	1073 Hz	96.95 %	1.74 MW/m^3	0.99 MW/t

Moreover, from this, the total losses, volume, and mass of these components for the 20 MW multi-rotor having five turbines per cluster can be obtained, and these are summarised in Table 5.10. The total values decrease compared to having three turbines per cluster, indicating potential savings.

Table 5.10: Power losses, volume and mass at the given optimum frequency for the SPWM and SFTM method with increased cluster size.

	f_{sw} [Hz]	Losses [MW]	Volume [m^3]	Mass [t]
AC cluster SPWM	1116	1.902	20.20	34.48
AC cluster SFTM	1194	1.024	17.24	28.99
DC cluster SPWM	1031	1.408	14.23	25.32
DC cluster SFTM	1112	0.686	11.98	20.62
Hybrid cluster SPWM	1038	1.300	13.99	24.69
Hybrid cluster SFTM	1140	0.610	11.49	22.20

The key performance indicators for case 3 with five wind turbines per cluster are illustrated in Figure 5.14 and Figure 5.15. For comparison reasons, the performance indicators for three turbines per cluster found in the previous cases are included with a dashed line. The continuous line illustrates the results of this case.

Figure 5.14 shows the performance indicators for the SPWM method. As the cluster size does not affect the AC cluster, these results coincide. In Figure 5.14a, the efficiency is shown. This parameter is similar for all configurations, and the increase when having 5 turbines per cluster is similar for the DC and hybrid clusters. Regarding the power density and power-to-mass ratio in Figure 5.14b and 5.14c, the increase when expanding the clusters are larger and still slightly favouring the hybrid cluster.

Studying the same plots for the SFTM method in Figure 5.15, reveals the same

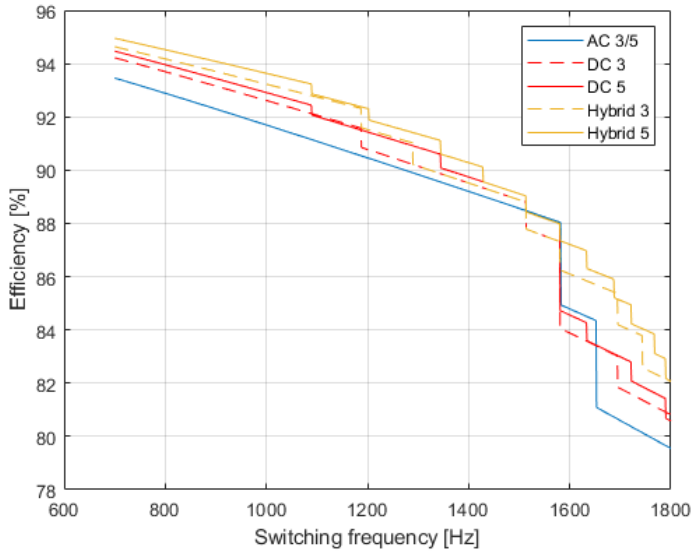

(a) Efficiency

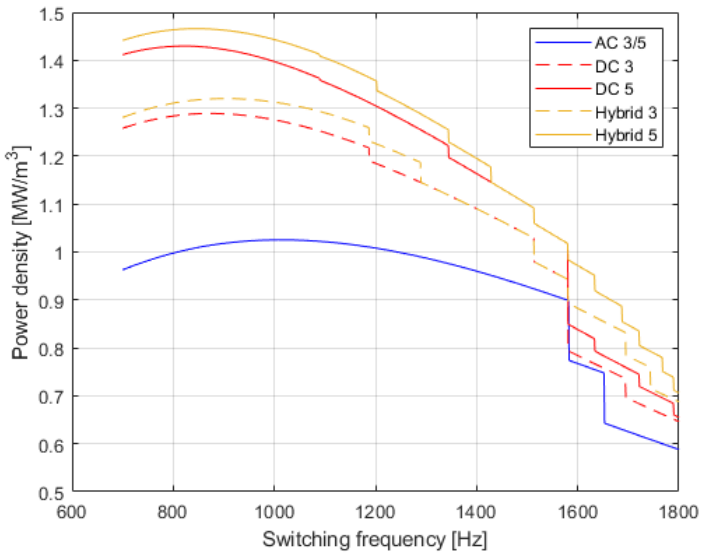

(b) Power density

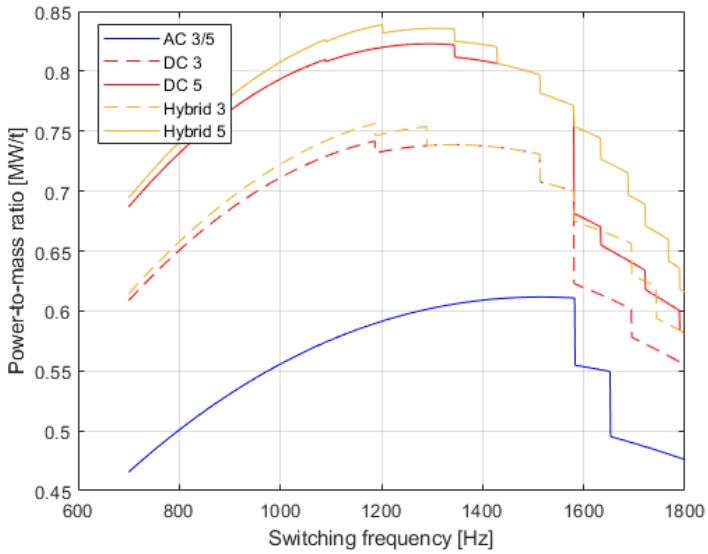

(c) Power-to-mass ratio

Figure 5.14: Comparison of key parameters for the topologies of three and five turbines per cluster, using SPWM.

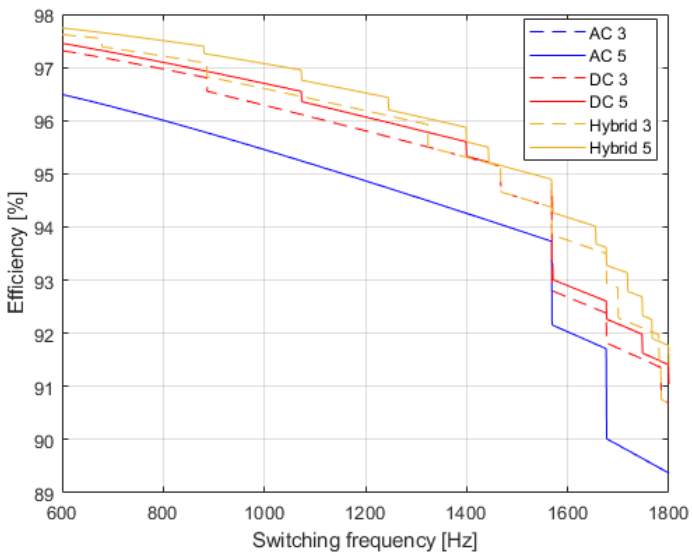

(a) Efficiency

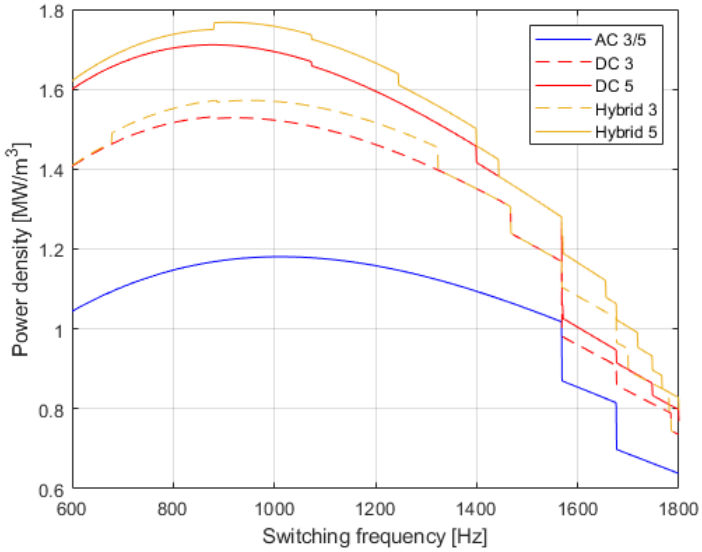

(b) Power density

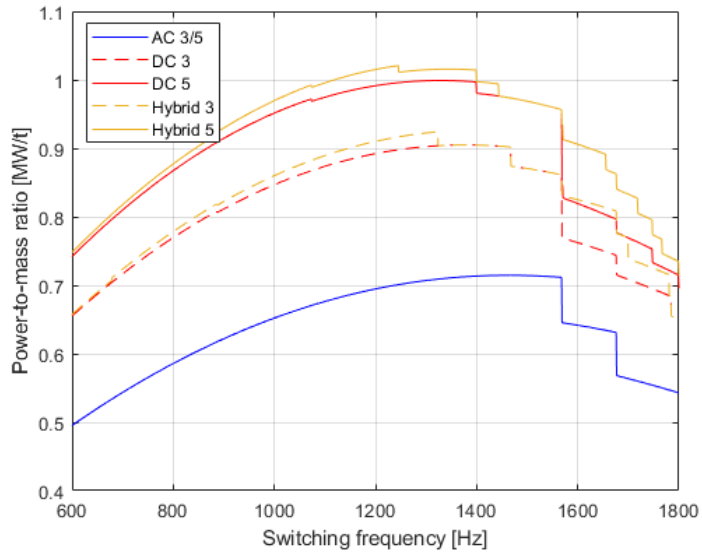

(c) Power-to-mass ratio

Figure 5.15: Comparison of key parameters for the topologies of three and five turbines per cluster, using SFTM.

trend as for the SPWM method. The efficiency is higher, and also the gap between the configurations is larger than for the SPWM. The plots for power density and power-to-mass ratio show the same trend, where the increase is similar for the DC and hybrid clusters, while the AC cluster remains constant when increasing the cluster size.

5.4.3 Pareto analysis of case 3

The plots of the Pareto analysis using five turbines per cluster are shown in Figure 5.16. Here, all the three configurations are included in one plot, for easier comparison.

In Figure 5.16a, the SPWM is used and in Figure 5.16b the SFTM. The power density and power-to-mass ratio are on the axis, and the red lines show the Pareto front between these two parameters. Besides, the colour bar shows how efficiency varies along with this relationship.

The plots are shifted to the right, starting with the AC cluster furthest to the left, then the DC cluster and the hybrid cluster respectively. One can observe that the maximum efficiency does not coincide with the Pareto front, as this is located at a lower power-to-mass ratio. The DC and hybrid clusters have a discontinuous Pareto front, one for maximum ρ and one for maximum γ. It is visible in both plots that the hybrid cluster in total performs the best around these most likely design points, with the DC cluster close behind.

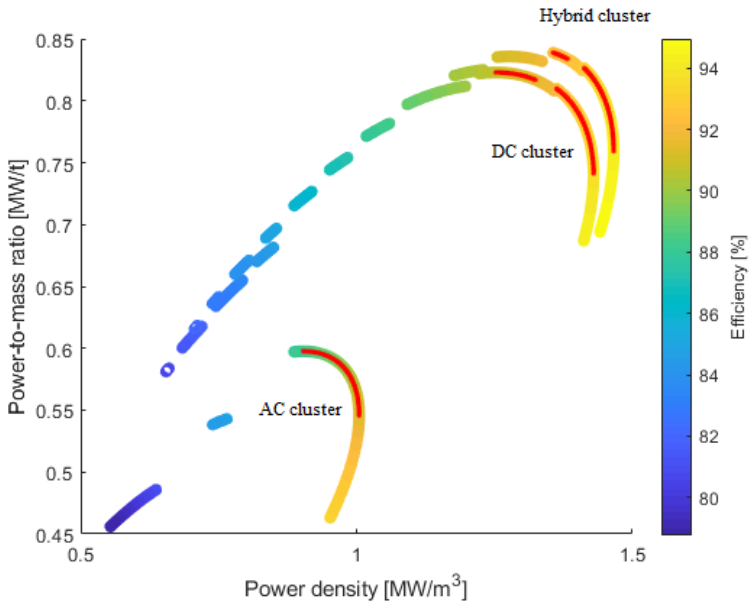

(a) SPWM

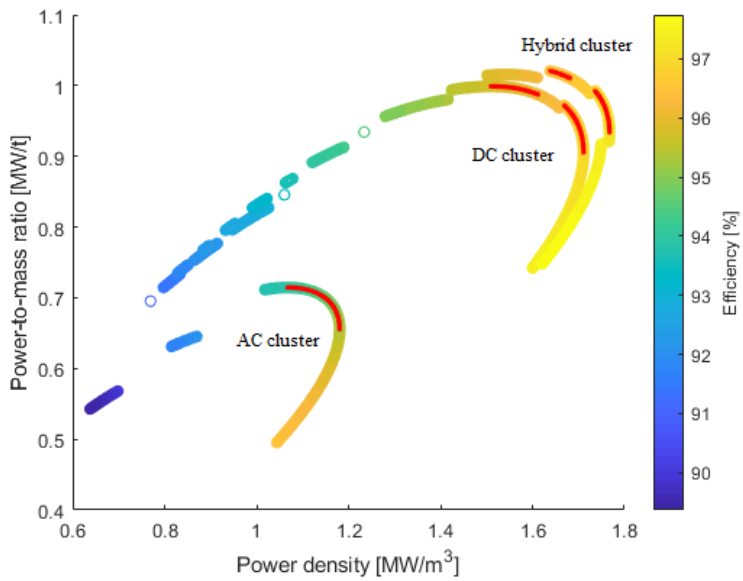

(b) SFTM

Figure 5.16: Pareto plot, power density versus power-to-mass ratio with efficiency indicated by colour bar for five turbines per cluster, using SPWM and SFTM.

5.5 Case 4: Increased power

In case 4, the machine power is increased to *750 kW*. *Three turbines per cluster* is again used, and both the *SPWM and SFTM methods* are studied.

The European project Innwind aimed to develop a 20 MW turbine [8]. In the report, this was chosen to consist of 45 turbines, each having a 444 kW rating. The scalability and small size of these machines and belonging blades were arguments for these configurations. However, also other machine sizes may be of interest to investigate, and this is performed in this case.

This section presents all the assumptions for case 4, which also uses the two modulation methods SPWM and SFTM. The results and the comparative analysis are presented for all configuration using both plots of the critical parameters and tables showing the optimum frequency and belonging parameters. The Pareto analysis is presented, where the three key parameters are plotted versus each other.

5.5.1 Assumptions in case 4

Also for this case, the parameters defined in Table 5.1 and 5.2, except the nominal power, are maintained, and the over-voltage factor varies due to different modulation techniques.

The change in turbine power affects the number of required turbines to reach 20 MW. A number of 27 turbines results in the total power of 20.25 MW, and this configuration makes it possible to divide into clusters of three turbines, and a total of 9 such clusters. Each cluster then has a power of 2250 kW, which is close to the power of one cluster in case 3.

This design requires larger blades and larger machines, and the rating of required electrical components increases. However, the number of needed components is reduced, as the number of turbines is reduced by 40 %. The AC cluster requires a total of 54 converters, the DC cluster 36 and the hybrid cluster 18 converters. The DC and the hybrid cluster also have reduced requirements of DC-links and phase reactors compared to the AC cluster. The requirements for filters, transformers, and cables are treated as equal for all configurations.

The increase in power to 750 kW, keeping the line-to-line RMS voltage unchanged at 690 V, leads to an increase in current. The limit in switching frequency remains unchanged despite the increase in power, but the maximum peak current increases for the configurations, affecting the minimum required number of parallel connected modules. These parameters are summarised in Table 5.11 for the two modulation techniques.

Table 5.11: Semiconductor module, peak current and required parallel connected modules for the topologies with the SPWM and SFTM method with increased machine power.

	Module	I_{psw}	$n_{p,min}$
AC cluster rectifier SPWM	3300V x 1500A	1493.1 A	1
AC cluster inverter SPWM	3300V x 1500A	1493.1 A	1
AC cluster rectifier SFTM	1700V x 3600A	1493.1 A	1
AC cluster inverter SFTM	1700V x 3600A	1493.1 A	1
DC cluster rectifier SPWM	3300V x 1500A	1493.1 A	1
DC cluster inverter SPWM	3300V x 1500A	4479.2 A	3
DC cluster rectifier SFTM	1700V x 3600A	1493.1 A	1
DC cluster inverter SFTM	1700V x 3600A	4479.2 A	2
Hybrid cluster rectifier SPWM	3300V x 1500A	4479.2 A	3
Hybrid cluster inverter SPWM	3300V x 1500A	4479.2 A	3
Hybrid cluster rectifier SFTM	1700V x 3600A	4479.2 A	2
Hybrid cluster inverter SFTM	1700V x 3600A	4479.2 A	2

5.5.2 Results and comparative analysis of case 4

For this case, the maximum Λ, its corresponding switching frequency and the key parameters at this switching frequency for the configurations are summarised in Table 5.12. Again, it is clear that the SFTM gives better results than the SPWM, and that the DC and hybrid cluster configurations perform better than the AC cluster. Actually, at this increased power, the DC and hybrid cluster configurations are sharing many of the design points. This is clear from the Table 5.12 where the values for the two modulation methods coincide for the DC and hybrid clusters. The values are quite similar to case 3.

Table 5.12: Maximum Λ values and its corresponding switching frequencies and performance indices at this point for the SPWM and SFTM with increased machine power.

	Λ_{max}	f_{sw}	η	ρ	γ
AC-C SPWM	2.971	1076 Hz	92.84 %	1.16 MW/m^3	0.65 MW/t
AC-C SFTM	2.964	1209 Hz	96.08 %	1.38 MW/m^3	0.81 MW/t
DC-C SPWM	2.934	1026 Hz	93.55 %	1.44 MW/m^3	0.82 MW/t
DC-C SFTM	2.947	1060 Hz	96.99 %	1.74 MW/m^3	0.99 MW/t
Hyb.-C SPWM	2.934	1026 Hz	93.55 %	1.44 MW/m^3	0.82 MW/t
Hyb.-C SFTM	2.946	1060 Hz	96.99 %	1.74 MW/m^3	0.99 MW/t

Repeatedly, the dimensions in terms of total mass and volume in addition to total power losses can be found based on the previously calculated parameters. As 750 kW-rated machines now are used, the individual units are larger, but this effect is more or less outweighed by the reduction in needed units to produce 20 MW. The total losses, volume, and mass are summarised in Table 5.13.

Table 5.13: Power losses, volume and mass at the given optimum frequency for the SPWM and SFTM method with increased machine power.

	f_{sw} [Hz]	Losses [MW]	Volume [m^3]	Mass [t]
AC cluster SPWM	1076	1.432	17.24	30.77
AC cluster SFTM	1209	0.784	14.49	24.69
DC cluster SPWM	1026	1.290	13.89	24.39
DC cluster SFTM	1060	0.602	11.49	20.20
Hybrid cluster SPWM	1026	1.290	13.89	24.39
Hybrid cluster SFTM	1160	0.602	11.49	22.20

The key performance indicators for case 4 with increased power to 750 kW are illustrated by the continuous line in Figure 5.17 and Figure 5.18. For comparison reasons, the results when using a power of 444 kW from previous cases are also included with a dashed line.

With the increased power, the addition of modules occurs at an earlier stage. This is especially clear for the AC cluster, which now is affected by the change in design. From the efficiency plot in Figure 5.17a, it is seen that this increased power makes the efficiency for the AC cluster approach the efficiency of the DC and hybrid clusters, despite that the efficiency of the two latter also increases with the increased power.

There is also a great increase in performance for all configurations in power density and power-to-mass ratio, as seen in Figure 5.17b and Figure 5.17c. Despite that the AC cluster increases more than the two other configurations, the DC and hybrid cluster configurations are still by far the most advantageous.

The same trend as for the SPWM is shown in the plot for the SFTM method, as shown in Figure 5.18. In Figure 5.18a, it is clear that the efficiency is still higher for the DC and hybrid clusters. Moreover, in Figure 5.18b and Figure 5.18c, the AC cluster performance increases more than the other, but still, in total, performs worse than the DC and hybrid clusters.

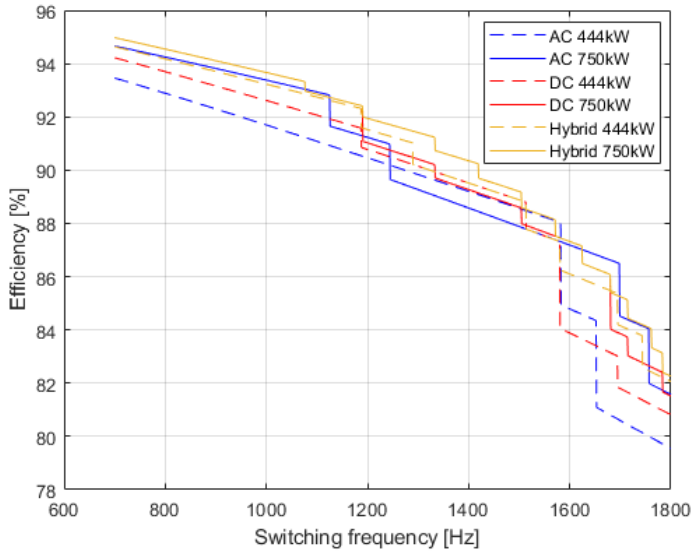

(a) Efficiency

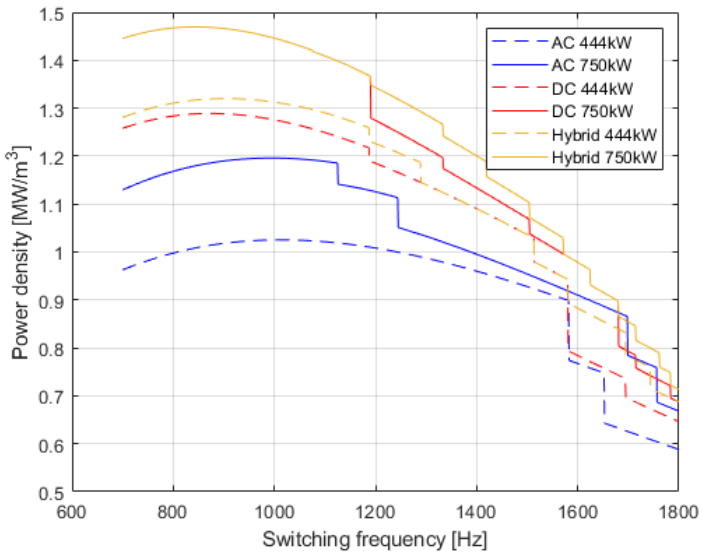

(b) Power density

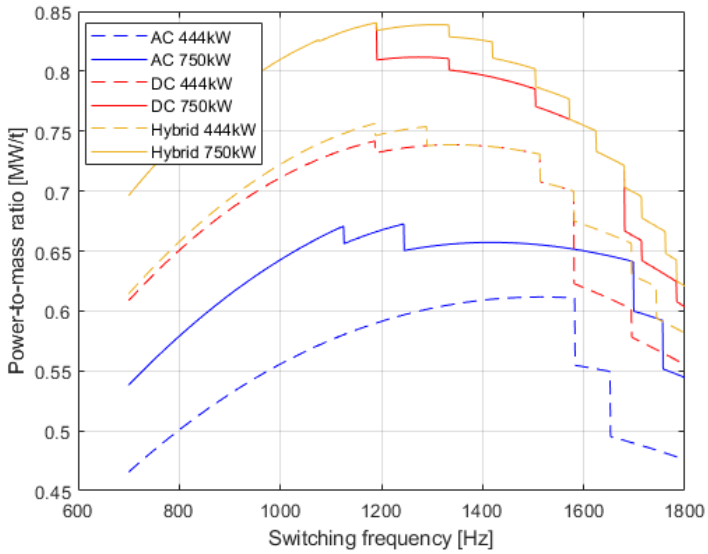

(c) Power-to-mass ratio

Figure 5.17: Comparison of key parameters for the topologies a power of 444 kW and 750 kW, using SPWM.

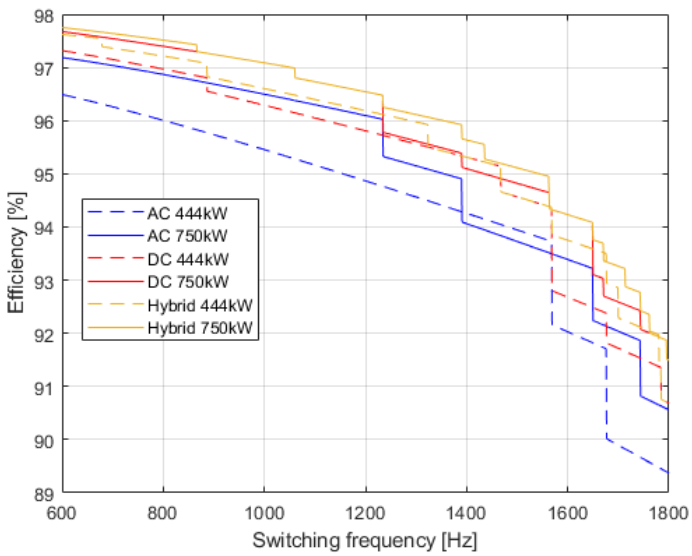

(a) Efficiency

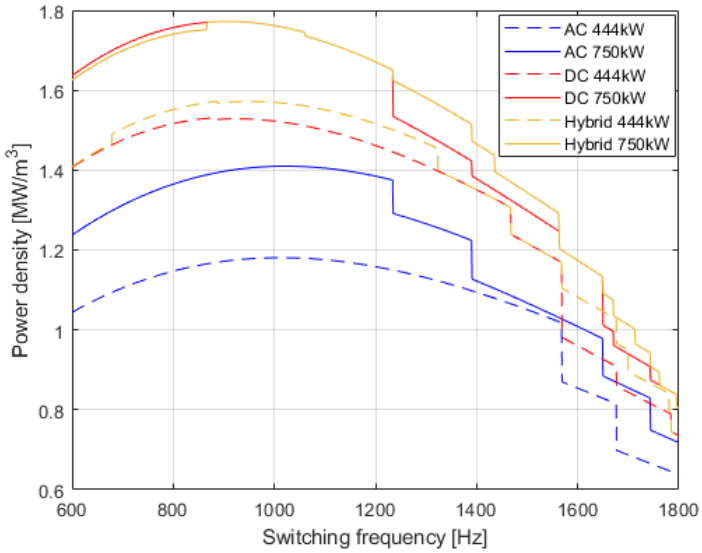

(b) Power density

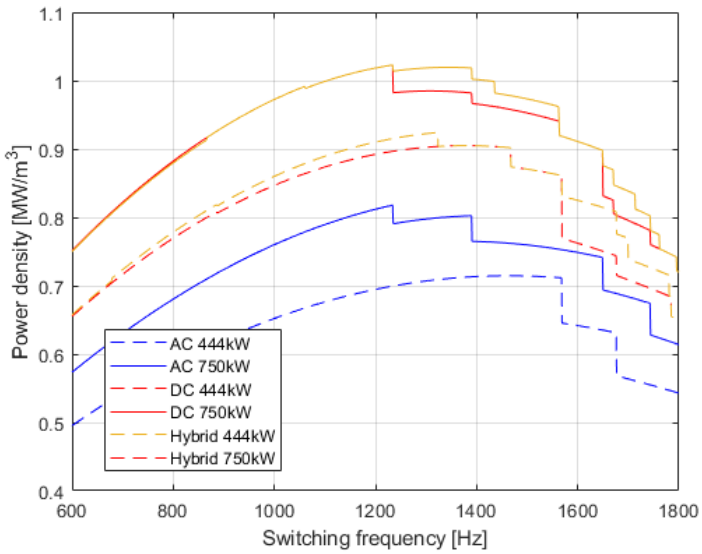

(c) Power-to-mass ratio

Figure 5.18: Comparison of key parameters for the topologies a power of 444 kW and 750 kW, using SFTM.

5.5.3 Pareto analysis of case 4

The results from the Pareto analysis when 750 kW-turbines are investigated are presented in 5.19. The figure is divided into two, where the three configurations are presented in each figure but for the two different modulation techniques. When comparing the two, it is easy to see that the SFTM method performs better, in terms of efficiency, power density, and power-to-mass ratio. However, in both plots, the trend is the same.

Figure 5.19a shows the Pareto analysis of all three configurations using the SPWM method. It is clear that the AC cluster is not at the same level as the DC and hybrid clusters, as can be seen in the Figure. The AC cluster has a clear Pareto front at a bit under 1.2 MW/m^3 and at around 0.65 MW/t. The DC and hybrid clusters coincide in most of the solution points, especially the ones relevant for the design, thus the Pareto front. This front is wider than for the AC cluster and is close to 1.5 MW/m^3 and around 0.8 MW/t. Also, the maximum efficiency is close to coinciding with the Pareto front and is at between 92-94 % along the Pareto front.

The plot showing the Pareto analysis using SFTM is shown in Figure 5.19b. The same trend is present here, with a clear step between the AC cluster and the DC and hybrid clusters. However, here the AC cluster has its Pareto front at more than 1.4 MW/m^3 and at around 0.80 MW/t. Also here, the DC and hybrid cluster solutions coincide in many points and share the Pareto front. This is at close to 1.8 MW/m^3 and at almost 1 MW/t. Besides, the efficiency is higher using SFTM than for the SPWM and is also higher at the Pareto front for the DC and hybrid clusters than for the AC cluster. However, with values between 96-97 % for the worst case operating conditions, is this more than acceptable values to have as design points.

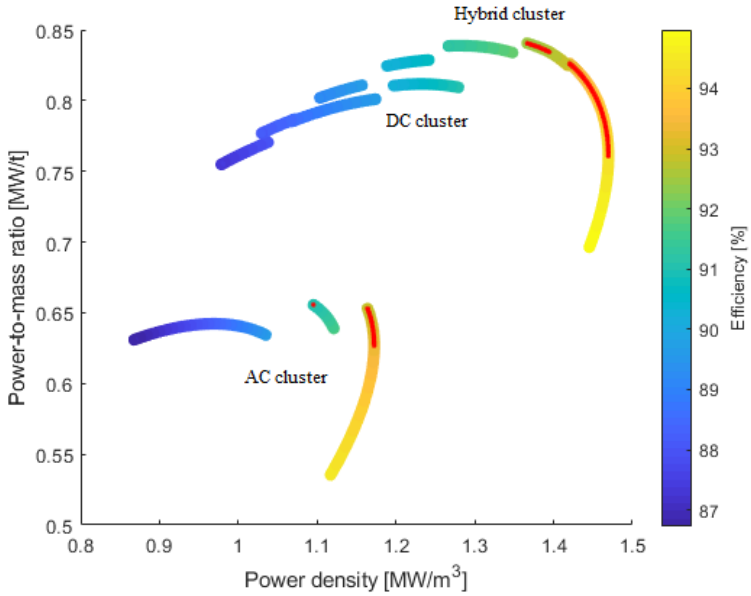

(a) SPWM

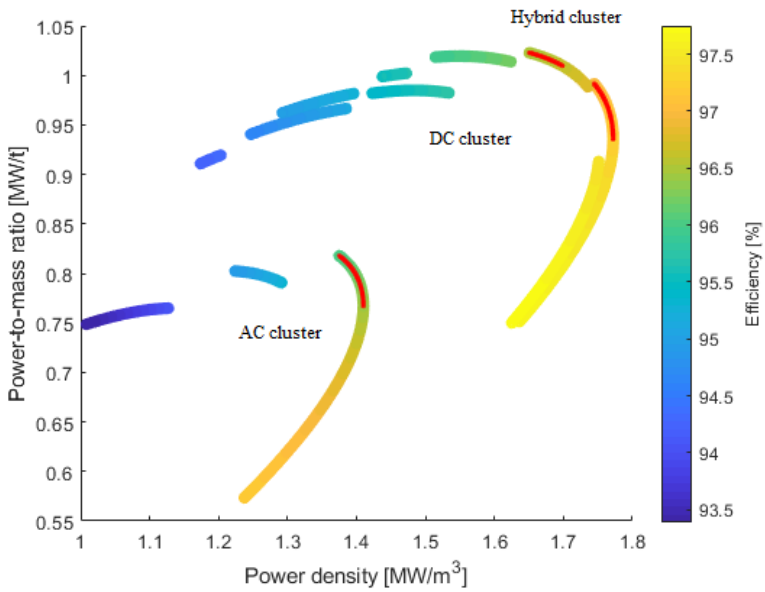

(b) SFTM

Figure 5.19: Pareto plot, power density versus power-to-mass ratio with efficiency indicated by colour bar for the increased power case.

5.6 Case 5: Series connection of the DC cluster

In the literature ([17], [19], [47], [48], [49]), the connection of turbines using DC is discussed, pointing out benefits of connecting both in series, parallel and a combination of those two. Even though this is challenging and still not tested in wind power systems, several works are advising this topology as a possible future configuration of DC connected wind farms. Challenges regarding over-voltages, reliability, insulation and DC equipment need to be overcome [47, 49], but the design can also provide a cost-efficient solution and decrease the requirement of transformers, as the series connection itself increases the voltage.

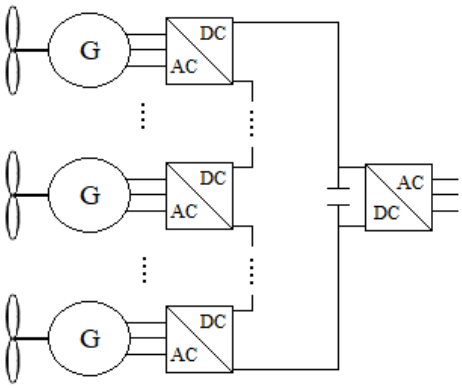

Figure 5.20: Cluster topology for DC series connection.

This case presents a study of a cluster connected in series as is illustrated by Figure 5.20. For simplicity, only *the SPWM method* is included, and *three, four and five turbines per cluster* are experimented with, rated at *444 kW*. The rated output voltage is still 690 V. As this configuration requires different voltage ratings of the semiconductor devices compared to the previous cases, these changes are presented in the section regarding assumptions for the case. In addition, as the output voltage of each cluster is higher in this series configuration, it is hard to compare the results with the previous cases directly. However, this case, providing the results and Pareto analysis in the following sections, can probably highlight some possible advantages of using this configuration.

5.6.1 Assumptions in case 5

The design change according to the number of wind turbines per cluster. In total, the configuration of 3 turbines per cluster gives 15 clusters in order to generate 20 MW, while 5 turbines per cluster require 9 clusters. 4 turbines per cluster are also

added, but a connection of only 4-turbine clusters does not come as close to the actual, desired rating. However, looking at Figure 2.3, combinations of cluster sizes can be made, and thus, it is interesting to observe how this configuration behaves.

The voltage ratings of the switch valves change depending on the number of turbines in the series connection. As the DC-voltage increases, the required blocking voltage increases as well. Notice that this has been held constant in the previous cases. The same 3300V x 1500A modules are used, and in the same way as parallel connections of modules have been performed to withstand the maximum peak current, semiconductor modules can be connected in series to increase the voltage capability.

As mentioned in the common assumptions for the case study, are the power losses calculated for the actually required blocking losses, which means that the power losses are somewhat reduced compared to if the precise semiconductor voltage rating would be used. This assumption designs the configuration in a way that adding modules in series could make it possible to lower the actual rated voltage of the semiconductors used to create a better fit. This is harder to realise in a practical design but performed to compare configuration and cases better, and also to make the calculation converge easier.

At the machine side, the voltage is divided by the number of machine side converters. Meanwhile, the single converter connected at the other side of the DC-link requires a higher number of series-connected devices. When the thermal resistance gets too low, another module can be connected in series to withstand this, instead of parallel which is done in the previous cases. A combination of series and parallel connections of semiconductor modules is not common in practice [24]. Thus, the DC-voltage, the blocking voltage of the module used, and minimum number of series connected modules of both the converter facing the machine ($n_{s,1}$) and the converter connecting all machines ($n_{s,2}$) for each number of turbines per cluster (n_C) are calculated by (5.4) and summarised in Table 5.14.

Table 5.14: DC voltage, required blocking voltage and number of required series connected modules in the individual rectifiers ($n_{s,1}$) and the shared inverter ($n_{s,2}$) for a different number of series connected turbines (n_C).

n_C	V_{DC}	$V_{DC,block}$	$n_{s,1}$	$n_{s,2}$
3	3.41 kV	3.30 kV	1	2
4	4.55 kV	3.30 kV	1	2
5	5.69 kV	3.30 kV	1	3

Table 5.14 shows that an increase in turbines per cluster increases the voltage capability due to the added semiconductor module coming from the extra con-

verter. On the other side, more turbines affect the design of the collector side converter. From the nature of a series connection, the voltage increases and the current remains constant when adding more turbines. Thus, the rated current is at 437.1 A, with the maximum peak current at 883.9 A from (5.2).

5.6.2 Results and comparative analysis of case 5

Calculations performed for configurations with both 3, 4, and 5 turbines per cluster were performed. The maximum Λ and the corresponding key parameters at this frequency are presented in Table 5.15.

Table 5.15: Maximum Λ values and its corresponding switching frequencies and performance indices at this point for the SPWM method using a series DC connection.

	Λ_{max}	f_{sw}	η	ρ	γ
DC 3	2.900	1023 Hz	91.89 %	1.25 MW/m^3	0.71 MW/t
DC 4	2.880	1136 Hz	91.31 %	1.27 MW/m^3	0.77 MW/t
DC 5	2.900	935 Hz	92.73 %	1.38 MW/m^3	0.77 MW/t

Table 5.15 shows that there are more significant differences in the optimum switching frequencies than in previous cases. The efficiency at the optimum switching frequency increases is best for the five turbines per cluster case, but this is also the case with the by-far lowest optimum switching frequency. The power density and power-to-mass ratio increases with cluster size. Nevertheless, the obtained values are in the same spectre as the results for the DC cluster configurations using SPWM with 3 and 5 parallel-connected turbines per cluster (case 1 and 3). Further, the efficiency, power density, and power-to mass for the three alternatives are presented in Figure 5.21.

The graphs showing efficiency in Figure 5.23, show small differences between the three alternatives. They are both decreasing at the same rate, and some differences are seen correlated with the addition of modules. Also, the efficiency is kept at above 90 % until around 1350 Hz.

It is more interesting to study the power density and power-to-mass ratio in Figures 5.21b and 5.21c. The trend is similar for all alternatives, where the power density experiences a maximum between about 800 - 1000 Hz and the power-to-mass ratio at much higher frequency. However, it is seen that when more series connected modules are connected, there is an increase in both power density and power-to-mass ratio. The maximum of these parameters occurs after several additions for all configurations. This consequence is due to an increased advantage when one extra module is added, as this makes the required cooling system, and

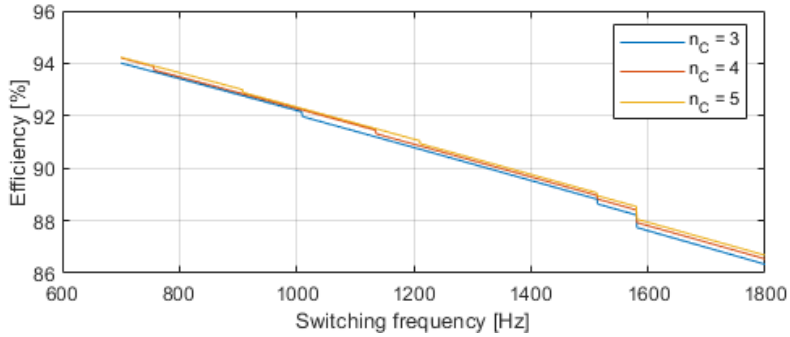

(a) Efficiency

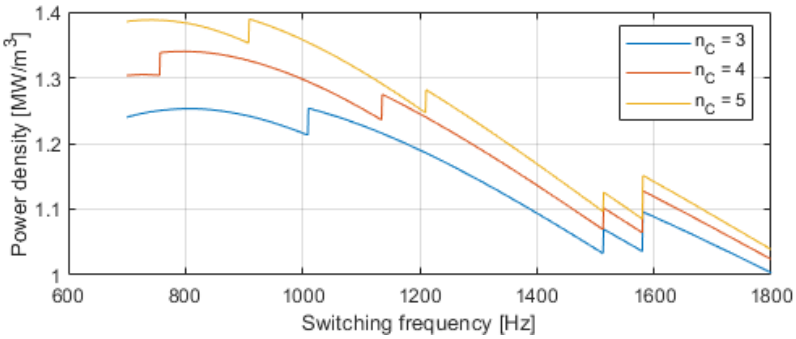

(b) Power density

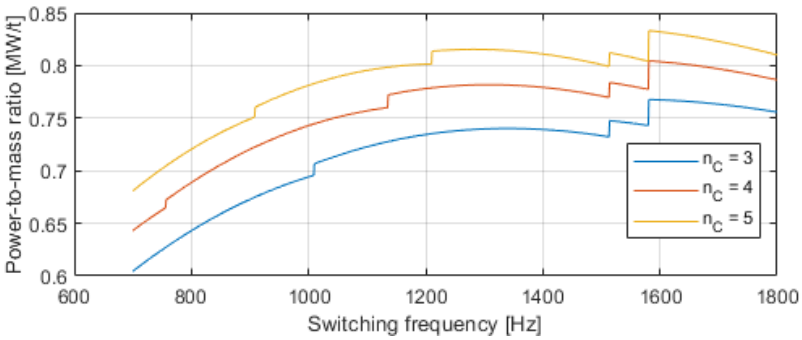

(c) Power-to-mass ratio

Figure 5.21: Comparison of key parameters for the DC series connection with cluster sizes of three, four and five turbines.

thus the modules, much smaller, so this, until one point, outweighs the effect of increasing the number. This can further be explained by studying the thermal resistance, as the addition of one module makes this resistance increase much more than for the other cases. Thus, if power-density is seen as more important than the other parameters, the design switching frequency can be increased to meet these criteria. However, this adds higher switching losses.

5.6.3 Pareto analysis of case 5

The results from the Pareto analysis is presented in Figure 5.22. The figure shows the solutions when having both 3, 4, and 5 turbines per cluster, as indicated. The efficiency is presented as the colour bar, and the red dots represent the Pareto front between power density and power-to-mass ratio.

As the number of turbines per cluster increases, the Pareto front shits to the right. The efficiency at the Pareto front is in all alternatives at around 91-93 %, except the point with the maximum power-to-mass ratio. All three alternatives have a Pareto optimal point at a location with reduced power density and efficiency. This relation is explained by the increase in the power-to-mass ratio at higher frequencies, as discussed in the previous section. Thus, it is shown by the plots that this configuration would benefit from higher switching frequencies, as this increases the power-to-mass ratio, which is an essential factor. Also, there are clear benefits of having larger clusters, but this trend decreases with size. Besides, the protective gear and insulation requirements increase with higher voltage. Meanwhile, also the increased voltage level makes the system less dependent on large and heavy transformers to step up the voltage.

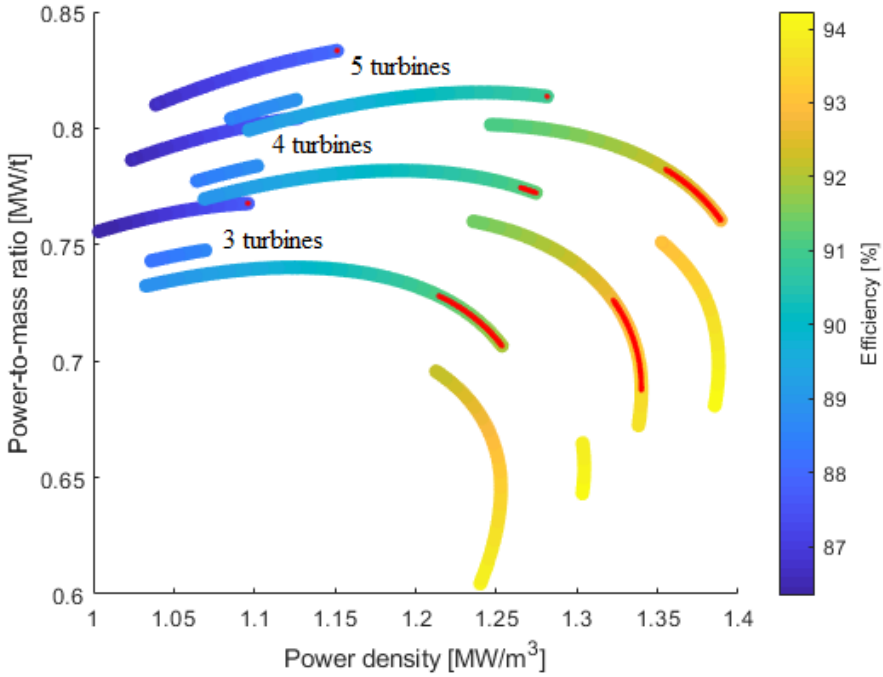

Figure 5.22: Pareto plot, power-density versus power-to-mass ratio with efficiency indicated by colour bar for DC series connection of three, four and five turbines.

5.7 Comparison of all cases

The five different cases are studied, which enables the possibilities to compare the different options with each other. The performance parameter plots, Pareto plots, and tables show some repeating patterns, but still, differences between configurations and within one configuration while the design is varied, occur. These main remarks are pointed out in this section.

It is evident that the chosen modulation method has a definite impact. The SVPWM and SFTM can modify the harmonics, thus resulting in a lowered required DC voltage, which is of high relevance as this allows other semiconductor modules with lower voltage ratings to be used. Despite that this has a powerful impact here, it is also worth mentioning that this effect is especially crucial at these specific voltage levels used here, as changes between two heavily commercially available and standardised modules occur around these ratings.

The results obtained in the previous sections indicate the importance of the key comparison parameters, η, ρ, and γ. When the power losses are found for

the whole 20 MW multi-rotor system based on the efficiency, it is observed that the few percentage points separating the configurations equals up to 500-600 kW difference in total losses. Also, for the total volume and mass of the system, small differences in the power density and power-to-mass ratio pose big differences. This is illustrated in, for example, Table 5.5, where the jump from 0.99 to 1.26 MW/m^3 and 0.58 to 0.72 MW/t from the AC to DC cluster equals around 4.5 m^3 and 6.5 tons. It should be kept in mind that these values are specific for the used component technology and vary according to the material used. Also, the total value of losses, volume, and mass are excluding several parameters which also, in reality, make an impact. Nevertheless, the parameters show the severe impact they have on design.

Throughout the cases 1-4, there is a clear, conspicuous trend when the different configuration are put against each other. Namely, the DC and hybrid clusters are quite similar to each other at the advantageous design points, while the AC cluster does not share this good performance on these parameters. Reasons for this is probably that the high amount of needed power converters and phase reactors is disadvantageous compared to the reduced amount needed in the DC and hybrid clusters. Also, investigating the ratings of the semiconductors, they are in case 1, case 2 and case 3 rated for a much higher current than what occurs in the AC cluster. This current rating fits better the DC cluster inverter and the hybrid cluster rectifier and inverter, as they have a higher power and thus higher current. This misfit impacts somewhat the AC cluster configuration, which probably would perform better if power modules closer to its rating were used. However, the higher required need of components seems to be the leading cause, and the advantage this cause cannot be overseen.

As the power in case 4 is increased to 750 kW, the current increase while the voltage is kept constant. The current in the turbine-facing converters is then very close to the current rating of the used semiconductor at 1500 A for the SPWM. The higher current affects positively on the AC cluster, as its performance improve and is closer to the performance of the DC and hybrid clusters. However, these configurations also improve their performance as power is increased. Thus, the argument about the big gap between semiconductor current rating and current in the AC cluster being a disadvantage does not seem to be deciding.

Furthermore, the performances of the DC and hybrid clusters seem to approach each other as the power increases. From Figure 5.19, it is noticed that their optimum design points coincide.

Increasing the number of wind turbines per cluster does not affect the AC cluster for the components studied here. If the scope were to be expanded, this topology would, however, also be affected, as the number of turbines sharing components such as transformers, filters, and cables would increase. For the DC and hybrid

cluster, the performance is increased when additional turbines are added to the cluster. The higher rating of the fewer power converters, capacitors and inductors seem to be beneficial, which increases the η, ρ and γ slightly. Also here, if the scope is expanded, the configurations are affected by more turbines sharing transformers, filters, and cables, and the benefits may be levelled out.

The previously stated relations, saying that both increasing power and the number of turbines per cluster is beneficial, is supported by Figure 5.23. This plot shows all possible solutions for the AC, DC, and hybrid clusters when a sweep of machine power from 444 kW to 750 kW is performed, using the SPWM method. Besides, the number of wind turbines per cluster is swept from three to five for the machine power. The plot shows the power density versus power-to-mass ratio for one such cluster and coloured based on the efficiency. However, the data from the series connection of the DC cluster is not included here, as this is hard to compare with the others, using this representation.

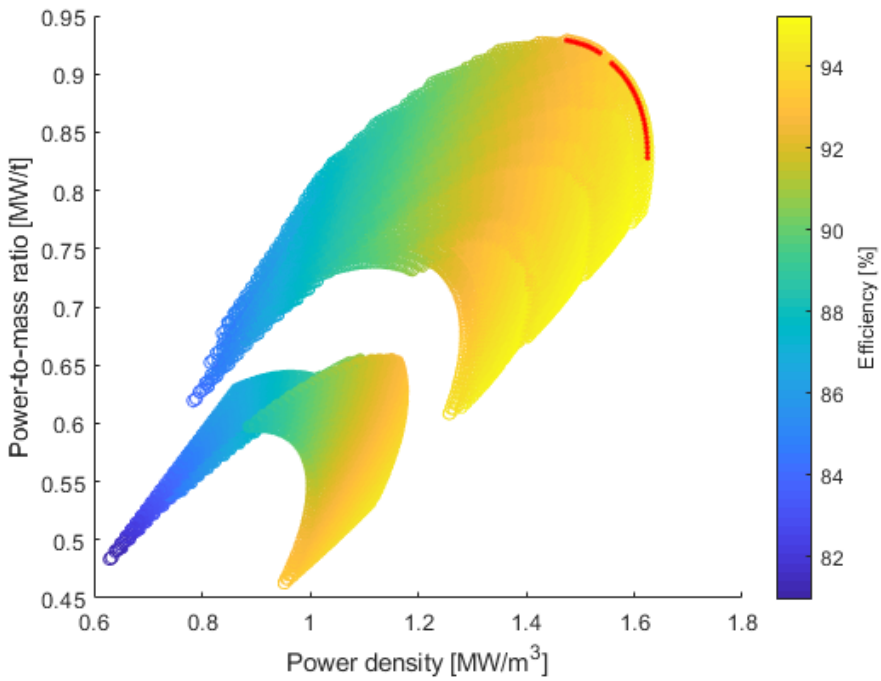

Figure 5.23: Pareto plot showing the Pareto front for all results from a sweep of cluster and machine size, using SPWM.

Analysing Figure 5.23, there is a noticeable leap between the results for the AC cluster and the results for the DC and hybrid clusters. From this, it can be read that

high power is needed to compete with the DC and hybrid clusters configurations when limiting the scope to these components. The best performance for the AC cluster is for 750 kW, and the power must be further increased to tangent the weakest performance of the other configurations. The space of solutions for the AC cluster is much smaller than the two others, as this only changes for changes in power, not in cluster size.

The Pareto front, indicated by a red dotted line, shows the optimum solution for all obtain results combined. For the DC and hybrid clusters, the weakest performance is for small cluster sizes and low power rating. When this increases, the performance increases along with their solution points being more and more coinciding. The Pareto front corresponds to both the DC and hybrid clusters, with 5 turbines per cluster and a power of 750 kW. It is also worth noticing that increasing power and the number of turbines barely affects efficiency, as this is mostly around 93-94 % at every relevant point.

However, this does not mean that making large clusters with large machines necessarily makes the best solution in total. It may appear as this might give reasonable solutions for the electrical components studied, but many aspects which are excluded here need to be studied. Large clusters will, for a fact, complicate the control, which is an essential part of the system. For the hybrid cluster, the total efficiency is decreased as more turbines have to operate at a non-optimum rotational speed. This aspect is further discussed in Chapter 6. The reliability is also affected, as a failure may affect a more significant part of the system if the clusters are large. Also, the increased aerodynamic performance found from simulations for the design having 45 small rotors decreases for fewer and larger turbines.

In Figure 5.24, the different solutions for the studied DC connections are compared. The blue lines show connections with three turbines per cluster, and the green lines are five turbines per cluster. If a parallel or series connection is displayed is indicated by different tones of the respective colour. First, it is observed clear benefits in both power density and power-to-mass ratio when having five turbines per cluster compared to three. Also, it is visible that the parallel connection, which is indicated by a darker tone of the respective colours, has a higher power density than the series connection. However, the series connections have a higher maximum power-to-mass ratio. Meanwhile, compared to previous plots, including the efficiency, the highest efficiency is also in the areas with the highest power density.

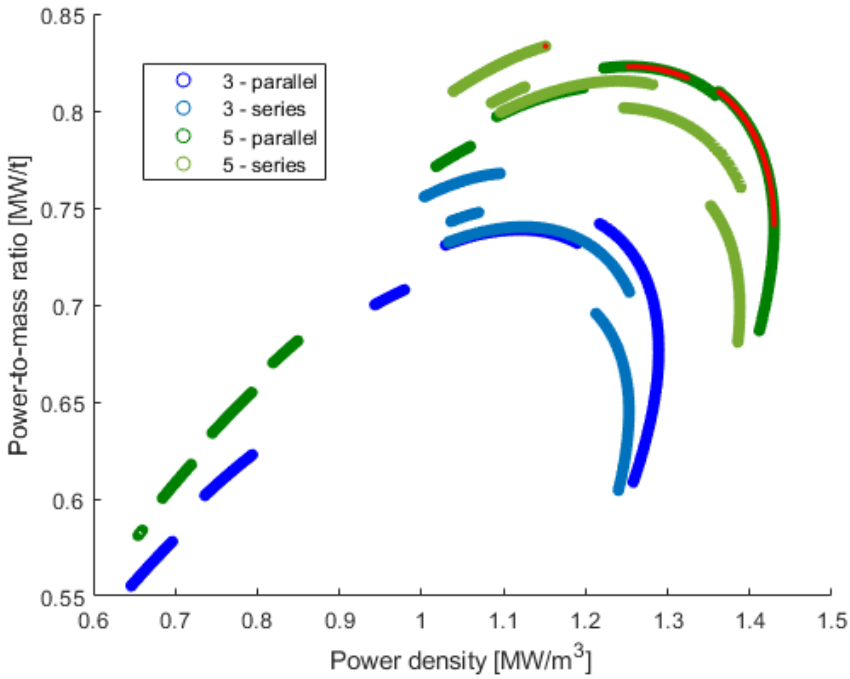

Figure 5.24: Pareto plot comparing DC parallel and series connection with three and five turbines per cluster.

The red dots represent the entire Pareto front of all possible solutions in the plot. This front is located only at the five turbines per cluster parallel connection result. However, there is also a point on the five turbines per cluster series connection line, where the power-to-mass ratio is maximised. Thus, the series connection increases its advantages if the mass is regarded as more important than volume and efficiency. What is not clear from this analysis, is also that the plots showing the series connections are at a three or five times higher voltage level. The need for transformers and DC-DC converter are decreased, which, at the system level, decreases further volume and power losses. However, this also requires more protective equipment, insulation, and advanced switchgear. Thus, what is most beneficial when expanding the system must be further analysed.

5.8 Summary

This chapter has shown various sets of cases comparing the configurations proposed. In addition to the three widely different configurations presented in Figure 1.1 which

was analysed in case 1-4, also a variation of the DC cluster was analysed in case 5, looking into the effects of connecting the turbines in series instead of parallel.

For all cases, tables have been presented showing the semiconductor device design as well as parameters at the optimum switching frequency found by optimising the Λ-function from (3.4). Besides, plots showing the performance indicators of the different cases have been presented in addition to a Pareto analysis, where the Pareto front was found. In case 1, the analysis went into more in-depth detail, illustrating the power losses, volume, and mass of each component, in addition to the distribution of the power losses. A section comparing the different cases was presented at the end, discussing the primary relationships of changing the cluster size and machine size for the different topologies, as well as finding the best solution of the combined space of solutions.

What the analysis mainly has shown, is that increasing both cluster size and machine size increases the performance of all configurations. The AC cluster showed, as expected, no effects of increasing the cluster size, but gained more from increasing the power than the other configurations. However, increasing these design criteria also rises challenges which are not included in this study.

The results and analysis showed clear benefits of using the SVPWM or SFTM method in contrast to the SPWM, as this increased all the performance indicators. However, the trend is similar, independent o modulation technique. Thus, this can be chosen after then desired configuration is decided.

The series connection of the DC cluster showed exciting results, performing close to the parallel connection and even better if reducing mass is the main focus. The behaviour of increasing the number of series-connected semiconductor devices was interesting, as this enhances the voltage level at the same time as limiting the requirements of transformers.

Clear indications were found to support the realisation of the DC or hybrid cluster. These two topologies, all over, performed better than the AC cluster since they lowered the number of required devices. However, the limitations of the scope in this analysis must be taken into consideration. When expanding the scope also to include other components and aspects, the results may change. Parts of this expansion are further discussed in the next chapter.

Chapter 6

Conclusion and future work

Following is the concluding part of this thesis. Based on the obtained results, the configurations can be discussed and recommendations for further work provided. As there are many aspects regarding the multi-rotor system which could not be included in this work, some of them are described thoroughly in the proposals for future work and should be addressed in a future study.

6.1 Conclusion

In this thesis, optimisation and design of electrical collectors for a multi-rotor system have been performed. First, in Chapter 2, the multi-rotor system was studied, summarising already established aspects and pointing out the key concerns for the electrical design, which yet has not been studied to a large extent until now. Different configuration options, based on literature, were proposed, and these were further analysed throughout the thesis. The main objective was to cover a multi-objective optimisation of different parameters, in order to provide guidelines in the electrical design of the multi-rotor system.

A set of three performance indicators has been selected, i.e., efficiency η, power density ρ, and power-to-mass ratio γ, and their relevance were explained in Chapter 3. The Pareto analysis was introduced, as this tool offers a way of easily locating reasonable design points and what possible trade-offs should be for the studied system.

In Chapter 4, detailed models of the different components were developed. For instance, different modulation techniques and how changing modulation influences the design are laid out. Analytic expressions on how to obtain necessary parameters are gathered, based on literature and available component datasheets. Particular emphasis is given to the design of the semiconductors since they are directly related

to the efficiency and size of the components. Chapter 5 explains how to perform the electrical design in terms of voltage and current rating, and how to decide the minimum required number of devices, either in series or parallel. Following in the chapter was the case study, comparing the previously proposed configurations with different internal designs, such as cluster size, machine power, and modulation method. The last case handled a variation of the DC cluster design, where the turbines are connected in series.

The AC cluster topology offers a known and well-proven technology, and this is an advantage per se because of the component availability. The individual back-to-back converter ensures excellent controllability, and a sharing of other vital components such as transformers and cables can be performed. The AC cluster shows acceptable efficiency, close to the other configurations for all cases, especially when the machine power is increased. However, because of the high number of components needed, the power density and power-to-mass ratio are relatively weak. One cause of this overall performance is that the selected semiconductor module ratings fit the AC cluster worse than the other configurations. Meanwhile, the analysis indicates that this is not the leading cause and that instead the high number of power converters and phase reactors create more losses and require more volume and mass in all cases. As shown in case 4, the AC cluster gains some performance when the machine power is increased, but can still not compete with the other configurations in terms of power density and power-to-mass ratio.

The DC cluster topology performs well in terms of efficiency, power density, and power-to-mass ratio. A primary contributor to this is the reduction of needed components. As the turbines are connected to the same DC link, the need for individual inverters is removed, which decreases the number of both total converters and phase reactors. The total efficiency, power density, and the power-to-mass ratio are all over sufficiently higher than the AC cluster due to this. For increased machine power to 750 kW in case 4, the performance indicators for the parallel connected DC cluster tangents several of the design points from the hybrid cluster, which otherwise performs the best.

The series connected DC cluster is promising since this topology performs just slightly worse than the parallel connected overall, but better if the power-to-mass ratio is weighted more. Besides, the series connection results in a higher voltage level, limiting the need for transformers at a later stage in the topology. For the DC cluster, it is also shown that the performance increase with both increasing the cluster size and the machine power. On the other side, collection in DC grids is still not common practice, and some components must be developed to realise this topology, e.g., this includes medium-frequency transformers, which reduces space needed, but also protective gear needed for DC at this power must be more researched. This yields especially for the series connection, which encounters high

voltage. However, the potential benefits are clear, making a variation of the DC cluster highly relevant.

It is reasonable to say that the hybrid cluster overall performs the best of the studied configurations. The efficiency, power density, and power-to-mass ratio of the hybrid cluster are the leading parameters in all cases compared to the other configurations, except for high machine power, when the parameters of the DC cluster equalise them. This advantage is due to the even higher reduction in needed components in the hybrid topology. The performance increases with both increasing cluster size and machine power. The substantial savings in components is a clear benefit for this topology. In the further connection, a local AC or DC grid may be deployed. If a DC grid is used, together with MFTs, the same possibilities and challenges as for the DC cluster are inherited.

Moreover, despite the excellent performance on these components, control design might be a challenging aspect. As one converter has to set the operational points for several turbines, it is evident that a large proportion of the turbines have to operate at a non-optimal speed. However, due to the short distances between the individual turbines in one cluster, the effects might not be large enough to disadvantage such a topology as this. Nevertheless, increasing the number of turbines per cluster saves more components but results in more turbines operating at this non-optimum speed. A converter failure also affects the turbine operated by that converter. How this affects the efficiency must be further studied, and a reasonable trade-off must be investigated. Besides that, the hybrid topology offers massive savings and could potentially serve as a good option in designing a multi-rotor system.

From this study, it is noted that exploring other modulation methods than the less complicated SPWM may be beneficial in terms of reducing harmonics and lowering the DC voltage. However, the SVPWM and SFTM methods are more intricate to implement, and the same relationships were obtained, independent on the modulation method. Therefore, it is worth noticing that there is a clear difference, but this can be neglected until a proper design is selected.

One of the major potential advantages with the multi-rotor system is the reduction in the required material. As increasing the turbine size from 444 kW to 750 kW requires larger blades and more material, this might eliminate these potential savings. Since no significant impact in increasing machine power compared to increasing the size of the cluster was found, it is worth noticing that increasing machine size might not be beneficial when expanding the system, especially for the DC and hybrid clusters.

The high amount of needed components in the AC cluster, which made this configuration perform poor, may result in challenges in realising a system that can perform better than conventional wind farms in terms of LCOE. Realising a system

with low LCOE is a central objective, and the costs related to the high number of components in the AC cluster might disfavour this topology.

The potential of having low LCOE seems more achievable, based on the results of this study, for the DC and hybrid cluster topologies. They both perform similar regarding the performance indicators and should be further analysed. The potential of connecting turbines in series to a common DC link is as well considerable, but also challenging to realise with the current protection and isolation technology needed. The hybrid cluster must be investigated to obtain quantitative results on how much efficiency is lost versus the savings in components when controlling the speed of several turbines from one converter.

6.2 Recommendations for further work

This thesis is meant to set the ground for an extensive study on the electrical design of a multi-rotor system. Several simplifications have been performed in this work, which must be taken into account in future work. The scope is limited, and future work must include expanding the system, including the connection between clusters. The means focus on other components, such as transformers, protective gear, and cables. In order to realise a DC connection grid, particular emphasis to the MFT, DC protective gear and cables must be given.

In this section, some qualitative remarks regarding three essential aspects are discussed to motivate future work on these fields. Hence, filter requirements, choice of the machine as well as control aspects are discussed here.

6.2.1 Filter

Only simplified AC filters have been implemented in this research. The more realistic filters have not yet been covered in order to simplify the study. However, some qualitative remarks can be pointed out to get an overview and a starting point for further work.

Regarding wind power, there are several reasons for the occurrence of harmonics. The harmonics from individual wind turbines come mainly from the power electronics equipment [50]. Also, in conventional offshore wind farms, the collection grid creates harmonics, mostly due to the capacitance of subsea connection cables and the inductance of transformers. When comparing a multi-rotor system to an offshore wind farm collection grid, one significant distinction is that subsea cables are not present, practically removing this as a cause of harmonics. However, the extensive use of power electronic converters and transformers creates harmonics, and it is crucial to study this to advance good design.

When selecting a filter, essential parameters, as before, are the efficiency, mass, and volume, and the material used is what mainly decides the costs [51]. The converter topologies already have inductive filtering, caused by the phase reactors. However, this usually is not efficient enough and purely inductive filters require too large inductance and result in high voltage drops [51]. An LCL filter is often used [51], where the first inductor is already present as the phase reactor, and the remaining capacitance and inductance need to be tuned carefully. From (4.43), the ripple of the output current from the converter relative to the fundamental current amplitude is defined. In this analysis, the phase reactors are dimensioned to reduce this ripple to a maximum this ripple to 20 %. A further reduction is necessary, but realising this with the phase reactors would require very large inductors. Nonetheless, the filter is needed to reduce this ripple to around 2 %, which is suggested by many authors in literature [51]. Thus, another inductor is needed in addition to a capacitor, resulting in an LCL filter. This capacitor is typically designed to provide reactive power of 5% of the rated power [51]. Larger capacitance reduces the size of the additional needed inductance but decreases the efficiency of the system.

The main challenges regarding the filtering are to locate where it is needed and the dimensions of the needed filters. It should be investigated if several wind turbines sharing filters are beneficial. Also, at the system level, if several clusters can share filters or not is of interest. All of this is proposed as future work.

6.2.2 Machine design

By now, a Permanent Magnet Synchronous Generator (PMSG) has been assumed to be the machine connected directly to the turbine. In [8], a PMSG is assumed, with a magnetic gearing integrated. Meanwhile, the generators used in Vestas 900 kW 4-rotor demonstrator [10] were V29-225 kW induction machines [52]. Thus, the type of machine which should be used for a multi-rotor wind turbine system is debatable and may also depend on the topology preferred.

Through the recent years, there has been a significant development in types of wind turbine drive trains. The Doubly Fed Induction Generator (DFIG) with a partial scale power converter has since the 2000's been the most adopted solution [18], and nowadays generators with full-scale power converters are getting more and more of the market share. The increased controllability, as well as the full-scale power converters (FSC) better ability to provide ancillary services to the grid, are some of the factors for this development. Which type of machine which will lead the next years is still unclear, but literature is leaning towards the PMSG [18, 53].

The DFIG has been a popular choice for single rotor turbines in wind parks, due to their relatively low investment costs. A WRIM is directly connected from

the stator, through a transformer, and to the grid, while the rotor is connected through a power converter. Because of this design, the power converter only needs to be designed for about 30 % of the power. On the other side, the DFIG requires a gearbox, which not only increases the service costs significantly [53], but increases the weight of the system. This is a significant disadvantage for a multi-rotor system. Besides, it is hard to realise a shared DC-link, eliminating the proposed DC cluster as an alternative. Thus, if a DFIG were to be used, the AC cluster and the hybrid cluster would remain as the possible topologies. However, the controllability of clusters of DFIG compared to FSC machines would be challenging, especially for the hybrid solution, as the DFIG offers more mediocre control attributes than a full-scale power converter.

In recent years, using solutions with full-scale power converters have been more and more popular, due to its comprehensive control options [18]. This can be realised by either connecting a SCIG, a dc-excited synchronous generator or a PMSG to the converter and further to the grid. The elimination of slip rings compared to the DFIG is an advantage, as this increases reliability. Also, the gearbox may be simpler or even removed, and the generator itself provides better power density and power-to-mass ratio, especially if permanent magnets are used instead of coils [53].

SCIGs are typically constructed with a belonging gearbox, and it is mainly the PMSG which has been deployed as a direct drive solution [54]. The SCIG is claimed to be available at a lower cost than the PMSG and has in recent years also been applied for variable speed operation [55]. Also, since the direct drive PMSG solution has no gearbox, the generator is large and heavy, consisting of multiple poles. A possibility to use SCIG for direct drive operation was therefore investigated in [54]. The lack of permanent magnets or salient poles was meant to make a competitive design and reduced required mass. Also, as the prices and availability of permanents magnets are insecure, this could be an advantage for the SCIG. It was found that increasing the number of poles reduced the required active mass of a SCIG, but this was still high compared to the PMSG and more at the level of a dc-excited direct drive SG.

When a direct drive system is desired, the direct driven PMSG is, therefore, a good option, especially for the configurations using some sort of a back-to-back topology. The costs might be higher initially, but the removal of gearbox reduces the operation and maintenance costs. The PMSG is larger than an SCIM, but the removal of the gearbox evens out this benefit. Also, since additional excitation is not needed for the PMSG, the losses are reduced. A future challenge, however, might be the availability of rare-earth magnets, which makes it necessary to pay attention to other wind turbine generator developments. As the connection in DC and also the proposed hybrid connection lowers the controllability, the induction

generators can gain some benefits for the configuration, as they easier can operate at variable frequency. It is, therefore, worth exploring the differences in applying SGs or IGs in a multi-rotor concept.

6.2.3 Control Design

The control algorithm of the multi-rotor wind turbine system is of high relevance and needs to be investigated extensively in order to realise the system. The control is essential, not only to make the system work and operate at acceptable efficiency but also to provide ancillary services, an ability which is required in the modern wind turbines [56]. Future wind turbines should be able to provide for instance reactive power, frequency support, and synthetic inertia to the grid, which makes control more complex and of higher importance than it has previously been.

From work performed in [8], it was found that the capability of the multi-rotor system to provide synthetic inertia is reduced compared to a conventional wind turbine of the same size. This is mainly due to the decreased mass of the several rotors in the system compared to one large rotor. However, provision of synthetic inertia, as obtained by other synchronous machines, is possible with this design. Besides, the droop capability of the investigated multi-rotor system was found to be at around 4 %, which is similar to conventional synchronous machines.

The layout of the control of the individual configurations is quite different because of their distinctness. Concerning the cluster level control, there are significant differences. As the AC cluster has one back-to-back converter per turbine, this offers maximum controllability. Each turbine can at every time operate at its optimum rotational speed, allowing maximum power capture. In addition, the voltage can easily be controlled for each turbine before the clusters are connected.

A significant part of the controllability is also maintained for the DC cluster. The individual VSRs make it possible to operate at optimum rotational speed and power capture. However, the voltage must be controlled by a shared VSI, which may limit how large the clusters can be. The design is also different depending on if a parallel or series connection is used, as the latter increases the voltage which needs to be controlled.

On the other side, the hybrid cluster does not have the possibility of every turbine operating at optimum speed. One VSC controls the operational point of every turbine associated with that cluster. This solution, of course, decreases efficiency, but work performed in [23] shows that it might be beneficial, accounting for the potential savings. Also, for a multi-rotor system, the different wind speeds for a cluster of turbines varies less than what is assumed for a wind farm in [23]. The hybrid cluster also needs the VSC to control the total cluster voltage.

For providing frequency support to the grid, the control of the whole multi-rotor

system is of paramount importance. On a system level, the control of the multi-rotor system can be compared with the control of wind farms, or wind farm control (WFC). In literature, different wind farm control methods are evaluated, mainly centralised or decentralised/distributed control [57, 58, 59, 60]. These concepts can also be adapted to yield for a multi-rotor system, in order to provide support to the grid.

The conventional centralised control is described as having an upper level, centralised control in addition to the lower level, individual wind turbine controllers. This centralised control obtains references from the TSO and computes reference points for the desired values, such as active power and reactive power. A heavy computational effort is used at this centralised controller to provide and send these set points to each turbine controller.

Because of the amount of needed computational effort for large wind farms, other methods such as decentralised and distributed control schemes have also more recently been studied [59, 60]. For these methods, the central controller is either completely removed or is present with limited requirements. Instead, the individual turbines get their reference points from their controllers.

When dealing with a multi-rotor system, the disadvantages that usually rises with centralised control is not present, as the number of individual turbines is not that large compared to large wind parks, and the distances are a lot shorter. Also, according to [60], in terms of performance, the centralised control cannot do worse than the distributed, as all information is better than local information. Therefore, a centralised control scheme can be proposed for the multi-rotor system. However, when dealing with wind farms of multi-rotor wind turbines, a more distributed scheme of these controllers can be discussed, as this contains several hundreds of individual wind turbines and clusters that need to be controlled.

The objective for the centralised controller is to control the active and reactive power from the multi-rotor wind turbine (or from a whole wind farm) and into the grid [61]. In this way, the system can contribute to controlling tasks such as conventional power plants. The controllers get requirements from the TSO, measurements from the power common coupling, and the available power from the individual turbines. Furthermore, reference signals to the lower level controller are elaborated based on these inputs. For the multi-rotor system and proposed topologies in this study, this will either be sent to each turbine (for the AC cluster VSR and VSI, and DC cluster VSR controllers) or the controllers for the whole cluster (for the DC cluster VSI and hybrid cluster VSR and VSI). How these differences in control approaches affect the performance, must be further studied.

The control functions for the central controller are summarised here and can be studied more in detail in [61] and [62]. The active power control must provide *balance control*, which can adjust the production up or down and *delta control*,

which makes the system operate with a power reserve in case of immediate need of extra power. In addition, a *power gradient limiter* which limits how fast the production can change up or down is required, as well as the *automatic frequency control*, which makes the system able to produce more or less power to compensate for changes in the frequency. Meanwhile, the reactive power control must be able to produce or absorb a constant amount of reactive power, in addition, be able to increase or decrease the amount of produced or absorbed, to compensate for deviations in the voltage.

How these requirements should be maintained for a multi-rotor system using the studied topologies in this work, must be thoroughly investigated in future work, to prove its capability to provide these ancillary services.

Bibliography

[1] WindEurope, "Wind in power 2017 annual combined onshore and offshore wind energy statistics." [Online]. Available: https://windeurope.org/wp-content/uploads/files/about-wind/statistics/WindEurope-Annual-Statistics-2017.pdf

[2] ——, "Wind energy in europe in 2018 trends and statistics." [Online]. Available: https://windeurope.org/wp-content/uploads/files/about-wind/statistics/WindEurope-Annual-Statistics-2018.pdf

[3] ——, "Wind energy in europe: Outlook to 2020." [Online]. Available: https://windeurope.org/about-wind/reports/wind-energy-in-europe-outlook-to-2020/

[4] GE Renewable Energy, "Haliade-x offshore wind turbine platform," accessed: 08.05.2019. [Online]. Available: https://www.ge.com/renewableenergy/wind-energy/offshore-wind/haliade-x-offshore-turbine

[5] R. McKenna, P. O. vd Leye, and W. Fichtner, "Key challenges and prospects for large wind turbines," *Renewable and Sustainable Energy Reviews*, vol. 53, pp. 1212–1221, 2016.

[6] P. Jamieson and G. Hassan, *Innovation in wind turbine design.* Wiley Online Library, 2011, vol. 2, no. 2.4.

[7] etipwind.eu, "Strategic research and innovation agenda." [Online]. Available: https://etipwind.eu/wp-content/uploads/2018-Strategic-Research-Innovation-Agenda.pdf

[8] P. Jamieson, M. Branney, K. Hart, S. Voutsinas, P. Chasapogiannis, P. Chaviaropoulos, G. Sieros, and J. Prospathopoulos, "Innovative turbine concepts - multi-rotor system," Tech. Rep. [Online]. Available: http://www.innwind.eu/-/media/Sites/innwind/

Publications/Deliverables/INNWIND-Deliverable-1-33-Revised.ashx?la=da&hash=161DF48B74627F19B1068644CF741A79A5FFCD0D

[9] P. Jamieson and M. Branney, "Multi-rotors; a solution to 20 mw and beyond?" *Energy Procedia*, vol. 24, pp. 52–59, 2012.

[10] M. P. v. d. Laan, S. J. Andersen, N. Ramos García, N. Angelou, G. R. Pirrung, S. Ott, M. Sjöholm, K. H. Sørensen, J. X. Vianna Neto, M. Kelly *et al.*, "Power curve and wake analyses of the vestas multi-rotor demonstrator," *Wind Energy Science*, vol. 4, no. 2, pp. 251–271, 2019.

[11] P. Chasapogiannis, J. M. Prospathopoulos, S. G. Voutsinas, and T. K. Chaviaropoulos, "Analysis of the aerodynamic performance of the multi-rotor concept," in *Journal of Physics: Conference Series*, vol. 524, no. 1. IOP Publishing, 2014, p. 012084.

[12] I. H. Sunde, O. Anaya-Lara, and R. E. Torres-Olguin, "Power losses in electrical topologies for a multi-rotor wind turbine system," in *Journal of Physics: Conference Series*. IOP Publishing, In press 2019.

[13] P. Pirrie, O. Anaya-Lara, and D. Campos-Gaona, "Electrical collector topologies for multi-rotor wind turbine systems," 2018, unpublished.

[14] I. H. Sunde, O. Anaya-Lara, and R. E. Torres-Olguin, "Power losses in electrical topologies for a multi-rotor wind turbine system," Poster presentation. [Online]. Available: https://www.sintef.no/globalassets/project/eera-deepwind-2019/posters/a_sunde.pdf

[15] Danmarks Vindkrafthistoriske Samling (DVS), "Vindmøller ved saltbæk vig 1873-1923." [Online]. Available: http://www.vindhistorie.dk/userfiles/downloads/faktablade/Faktablad_2a.pdf

[16] P. Verma, "Multi rotor wind turbine design and cost scaling," Master's thesis, 2013.

[17] K. Givaki, "Different options for multi-rotor wind turbine grid connection," in *The 9th International Conference on Power Electronics, Machines and Drives*, 2018.

[18] F. Blaabjerg and K. Ma, "Wind energy systems," *Proceedings of the IEEE*, vol. 105, no. 11, pp. 2116–2131, 2017.

[19] P. Lakshmanan, J. Liang, and N. Jenkins, "Assessment of collection systems for hvdc connected offshore wind farms," *Electric Power Systems Research*, vol. 129, pp. 75–82, 2015.

[20] C. Meyer, M. Hoing, A. Peterson, and R. W. De Doncker, "Control and design of dc-grids for offshore wind farms," in *Conference Record of the 2006 IEEE Industry Applications Conference Forty-First IAS Annual Meeting*, vol. 3. IEEE, 2006, pp. 1148–1154.

[21] M. Mogorovic and D. Dujic, "100 kw, 10 khz medium-frequency transformer design optimization and experimental verification," *IEEE Transactions on Power Electronics*, vol. 34, no. 2, pp. 1696–1708, 2019.

[22] M. De Prada, C. Corchero, O. Gomis-Bellmunt, A. Sumper *et al.*, "Hybrid ac-dc offshore wind power plant topology: optimal design," *IEEE Transactions on Power Systems*, vol. 30, no. 4, pp. 1868–1876, 2014.

[23] D. Elliott, S. Finney, and C. Booth, "Single converter interface for a cluster of offshore wind turbines," in *IET Conference on Renewable Power Generation (RPG 2011)*. IET, 2011.

[24] R. Barrera-Cardenas, "Meta-parametrised meta-modelling approach for optimal design of power electronics conversion systems: Application to offshore wind energy conversion systems," Ph.D. dissertation, 06 2015.

[25] K. Fischer, K. Pelka, S. Puls, M.-H. Poech, A. Mertens, A. Bartschat, B. Tegtmeier, C. Broer, and J. Wenske, "Exploring the causes of power-converter failure in wind turbines based on comprehensive field-data and damage analysis," *Energies*, vol. 12, no. 4, p. 593, 2019.

[26] J. H. Van Sickel, P. Venkatesh, and K. Y. Lee, "Analysis of the pareto front of a multi-objective optimization problem for a fossil fuel power plant," in *2008 IEEE Power and Energy Society General Meeting-Conversion and Delivery of Electrical Energy in the 21st Century*. IEEE, 2008, pp. 1–8.

[27] Canaero, "Pareto front," accessed: 21.03.2019. [Online]. Available: http://www.cenaero.be/Page.asp?docid=27103&

[28] I. Batarseh and A. Harb, *Power Electronics*. Springer, 2018.

[29] D. Fewson, *Introduction to power electronics*. Butterworth-Heinemann, 1998.

[30] I. Colak and E. Kabalci, "Developing a novel sinusoidal pulse width modulation (spwm) technique to eliminate side band harmonics," *International Journal of Electrical Power & Energy Systems*, vol. 44, no. 1, pp. 861–871, 2013.

[31] S. K. Peddapelli, *Pulse width modulation: analysis and performance in multilevel inverters*. Walter de Gruyter GmbH & Co KG, 2016.

[32] H. Doraya, R. Parmer, M. C. Sharma, and B. Kumar, "Space vector pulse width modulation: A technique to mitigate the total harmonic distortion," *International journal of advanced research in electrical electronics instrumentation engineering*, vol. 3, 2014.

[33] R. Teodorescu, M. Liserre, and P. Rodriguez, *Grid converters for photovoltaic and wind power systems.* John Wiley & Sons, 2011, vol. 29.

[34] M. Morisse, A. Bartschat, J. Wenske, and A. Mertens, "Converter lifetime assessment for doubly-fed induction generators considering derating control strategies at low rotor frequencies," in *Journal of Physics: Conference Series*, vol. 753, no. 11. IOP Publishing, 2016, p. 112003.

[35] S. Safari, A. Castellazzi, and P. Wheeler, "Experimental and analytical performance evaluation of sic power devices in the matrix converter," *IEEE Transactions on Power Electronics*, vol. 29, no. 5, pp. 2584–2596, 2013.

[36] N. Instruments, "Sources of loss," adapted from:. [Online]. Available: http://zone.ni.com/reference/en-XX/help/375482B-01/multisim/sourcesofloss/

[37] Üwe Schäfer, "Skript zur vorlesung "Elektrische Antriebe für Strassenfahrzeuge": 4. Leistungselektronik," 2017, unpublished.

[38] L. Helle, "Modeling and comparison of power converters for doubly fed induction generators in wind turbines," Ph.D. dissertation, Aalborg University, 2007.

[39] J. W. Kolar, H. Ertl, and F. C. Zach, "Influence of the modulation method on the conduction and switching losses of a pwm converter system," *IEEE Transactions on Industry Applications*, vol. 27, no. 6, pp. 1063–1075, 1991.

[40] C. Du, "Vsc-hvdc for industrial power systems," Ph.D. dissertation, Chalmers University of Technology, 2007.

[41] H. E. Tacca and C. Sullivan, "Extended steinmetz equation," 2002. [Online]. Available: https://www.aacademica.org/hernan.emilio.tacca/2.pdf

[42] B. Backlund, M. Rahimo, S. Klaka, and J. Siefken, "Topologies, voltage ratings and state of the art high power semiconductor devices for medium voltage wind energy conversion," in *2009 IEEE Power Electronics and Machines in Wind Applications.* IEEE, 2009, pp. 1–6.

[43] ABB, "Insulated gate bipolar transistor (igbt) and diode modules with spt and spt+ chips," accessed: 21.05.2019. [Online]. Available: https://new.abb.com/semiconductors/igbt-and-diode-modules

[44] Infineon Technologies, "Datasheet FZ1500R33HE3," 2018. [Online]. Available: https://www.infineon.com/dgdl/Infineon-FZ1500R33HE3-DS-v03_01-en_de.pdf?fileId=db3a304314dca389011527dfc61411c3

[45] ——, "Datasheet FZ3600R17KE3," 2013. [Online]. Available: https://eu.mouser.com/datasheet/2/196/Infineon-FZ3600R17KE3-DS-v02_00-en_cn-465139.pdf

[46] S. Singh and A. N. Tiwari, "Simulation and comparison of spwm and svpwm control for two level inverter," *2017 First International Conference on Smart Technologies in Computer and Communication (SmartTech-2017)*, 2017.

[47] R. Srikakulapu and U. Vinatha, "Electrical collector topologies for offshore wind power plants: A survey," in *2015 IEEE 10th International Conference on Industrial and Information Systems (ICIIS)*. IEEE, 2015, pp. 338–343.

[48] H. J. Bahirat, B. A. Mork, and H. K. Høidalen, "Comparison of wind farm topologies for offshore applications," in *2012 IEEE power and energy society general meeting*. IEEE, 2012, pp. 1–8.

[49] K. Musasa, N. I. Nwulu, M. N. Gitau, and R. C. Bansal, "Review on dc collection grids for offshore wind farms with high-voltage dc transmission system," *IET Power Electronics*, vol. 10, no. 15, pp. 2104–2115, 2017.

[50] C. Shan, "Harmonic analysis of collection grid in offshore wind installations," Master's thesis, NTNU, 2018.

[51] H. Brantsæter, Ł. Kocewiak, A. R. Årdal, and E. Tedeschi, "Passive filter design and offshore wind turbine modelling for system level harmonic studies," *Energy Procedia*, vol. 80, pp. 401–410, 2015.

[52] Vestas Wind Systems A/S, "Datasheet vestas v29," accessed: 22.05.2019. [Online]. Available: https://en.wind-turbine-models.com/turbines/273-vestas-v29#datasheet

[53] The Switch, "PMG vs. DFIG – the big generator technology debate," accessed: 06.05.2019. [Online]. Available: https://theswitch.com/2014/03/20/pmg-vs-dfig-the-big-generator-technology-debate/

[54] M. Henriksen and B. B. Jensen, "Induction generators for direct-drive wind turbines," in *2011 IEEE International Electric Machines Drives Conference (IEMDC)*, May 2011, pp. 1125–1130.

[55] B. Béchir, B. Faouzi, and M. Gasmi, "Wind energy conversion system with full-scale power converter and squirrel cage induction generator," *International Journal of Physical Sciences*, vol. 7, no. 46, pp. 6093–6104, 2012.

[56] A. D. Hansen, M. Altin, and F. Iov, "Provision of enhanced ancillary services from wind power plants–examples and challenges," *Renewable energy*, vol. 97, pp. 8–18, 2016.

[57] Q. Wu, Y. Sun, and J. Wiley, *Modeling and Modern Control of Wind Power*. Wiley Online Library, 2018.

[58] B. Karthikeya and R. J. Schütt, "Overview of wind park control strategies," *IEEE Transactions on Sustainable Energy*, vol. 5, no. 2, pp. 416–422, 2014.

[59] S. Asadollah, R. Zhu, M. Liserre, and C. Vournas, "Decentralized reactive power and voltage control of wind farms with type-4 generators," in *2017 IEEE Manchester PowerTech*. IEEE, 2017, pp. 1–6.

[60] T. Knudsen, T. Bak, and M. Soltani, "Distributed control of large-scale offshore wind farms," in *European Wind Energy Conference and Exhibition (EWEC) 2009*. Citeseer, 2009.

[61] A. D. Hansen, P. Sørensen, F. Iov, and F. Blaabjerg, "Centralised power control of wind farm with doubly fed induction generators," *Renewable Energy*, vol. 31, no. 7, pp. 935–951, 2006.

[62] J. Aho, A. Buckspan, J. Laks, P. Fleming, Y. Jeong, F. Dunne, M. Churchfield, L. Pao, and K. Johnson, "A tutorial of wind turbine control for supporting grid frequency through active power control," in *2012 American Control Conference (ACC)*. IEEE, 2012, pp. 3120–3131.

Appendix A

Used component parameters

A.1 Inductor and Capacitor parameters

The following parameters in Table A.1 were gathered from [24] and used to model the inductor and capacitor.

Table A.1: Capacitor and inductor regression coefficients and parameters [24].

DC Capacitor parameters	3-AC Inductor parameters
TDK MKP-B256xx	Siemens 4EUXX Cu, Fe
K_{VC0} = 2.00734e-5	K_{VL0} = 3.4353e-5
K_{VC1} = 0.7290	K_{VL1} =0.6865
K_{VC2} = 1.3796	$K_{\rho L0}$ = 4129.2244
$K_{\rho C0}$ = 1.3428e3	$K_{\rho L1}$ = 1.0768
$K_{\rho C1}$ = 1.0543	$K_{\rho w0}$= 9412.0118
$tan(\delta_0)$ = 2e-4	$K_{\rho w1}$=0.85361
$K_{\Omega C0}$ = 4.069e-3	f_{Lref}=50
$K_{\Omega C1}$ = -0.3211	$K_{\rho C0}$=8242.2998
$K_{\Omega C2}$ = -0.4661	$K_{\rho C1}$=0.99926
-	α_L = 1.1
-	β_L = 2.0

A.2 IGBT parameters

The following table in Figure A.1 show the different parameters and regression coefficients, found from the datasheet of the presented modules. They are gotten from [24].

General Info.	Ratings	(1700Vx3600A)		(3300Vx1500A)	
	Reference	FZ3600R17KE3		FZ1500R33HE3	
	$Vol_{mod}\,[dm^3]$	1.0108		1.0108	
	Mass $[Kg]$	1.5		1.2	
		IGBT	DIODE	IGBT	DIODE
Cond. losses model	V_{sw00}	0.964	0.959	1.436	1.359
	$\alpha_{Vsw0}[\frac{1}{C}]$	-0.89e-3	-1.36e-3	-0.237e-3	-3.19e-3
	$R_{C0}[m\Omega]$	0.401	0.249	1.130	0.804
	$\alpha_{Rc}[\frac{1}{C}]$	3.47e-3	2.54e-3	3.26e-3	0.62e-3
	$T_{j0}[C]$*	125		150	
Switching ON losses model	$K_{Eon0}[\frac{mJ}{V}]$	0.158	—	0.4895	—
	$K_{Eon1}[\frac{mJ}{VA}]$	6.36e-5	—	3.873e-5	—
	$K_{Eon2}[\frac{mJ}{VA^2}]$	3.44e-8	—	4.626e-7	—
	$\alpha_{Eon}[\frac{1}{C}]$	3.10e-3	—	2.7586e-3	—
Switching OFF losses model	$K_{Eoff0}[\frac{mJ}{V}]$	0.037	0.328	0.116	0.314
	$K_{Eoff1}[\frac{mJ}{VA}]$	4.04e-4	3.34e-4	7.31e-4	7.28e-4
	$K_{Eoff2}[\frac{mJ}{VA^2}]$	7.73e-9	-2.68e-8	4.53e-8	-1.35e-7
	$\alpha_{Eoff}[\frac{1}{C}]$	3.28e-3	4.25e-3	2.44e-3	5.33e-3
Parallel Connect.	$\triangle V_{sw}[V]$	0.45	0.40	0.55	0.75
	$\delta_{CI}[\%]$	18.48	28.72	19.36	26.16
Static thermal model	$R_{thJC}[\frac{K}{kW}]$	6.3	14	7.35	13
	$R_{thCH}[\frac{K}{kW}]$	8.7	19.5	10	11
	N_{isxm}	3		3	
	$T_{j,max}[C]$	125		150	

Figure A.1: Parameters and coefficients for the IGBT modules [24].

Appendix B

Case 2 Results

The following plots show the power losses, volume and mass for the three configurations studied, using both SVPWM and SFTM.

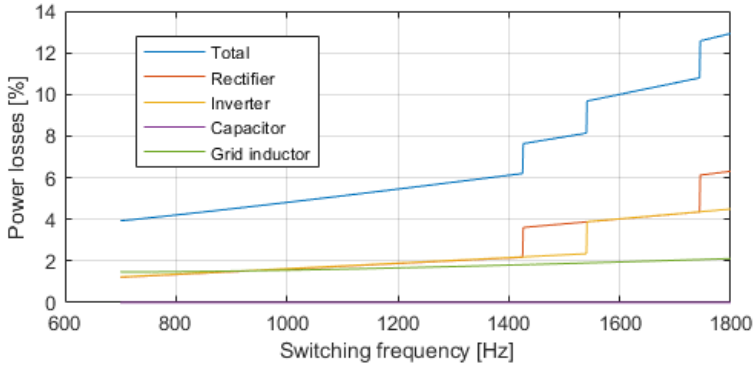

(a) AC cluster

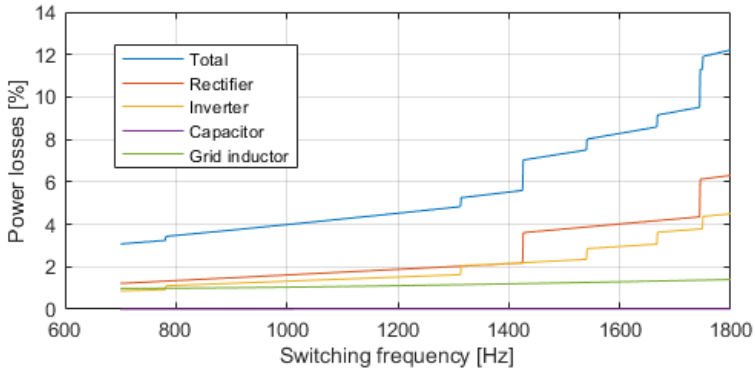

(b) DC cluster

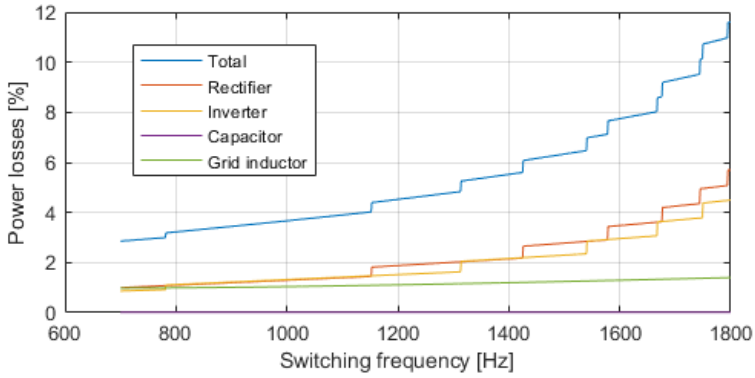

(c) Hybrid cluster

Figure B.1: Power losses for the AC, DC and hybrid cluster using SVPWM.

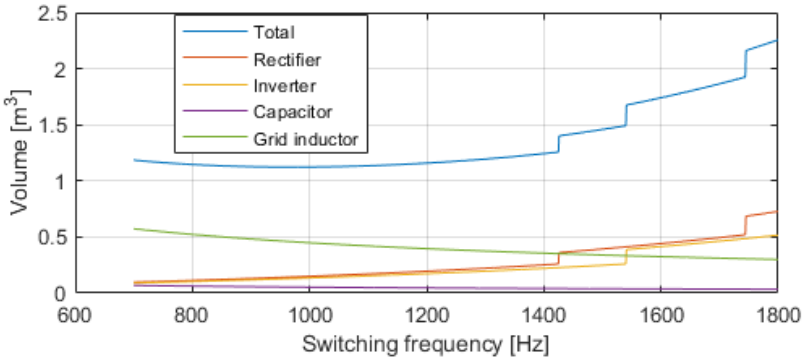

(a) AC cluster

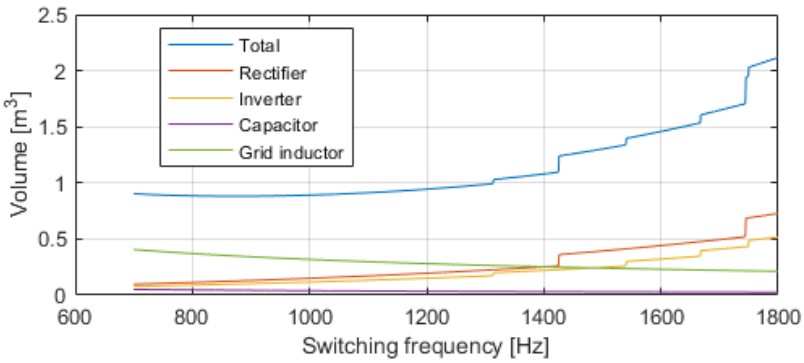

(b) DC cluster

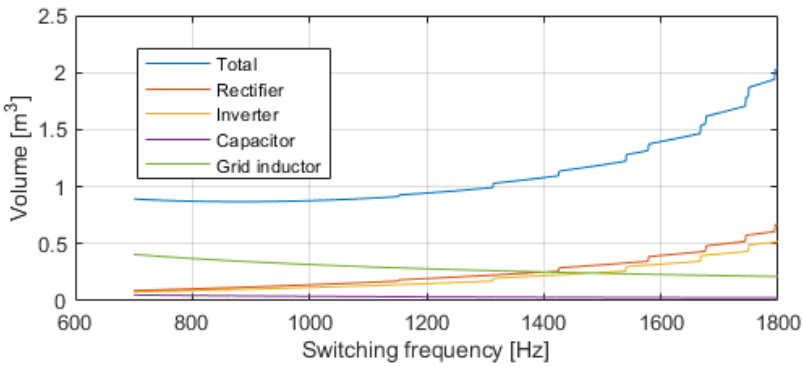

(c) Hybrid cluster

Figure B.2: Volume for the AC, DC and hybrid cluster using SVPWM.

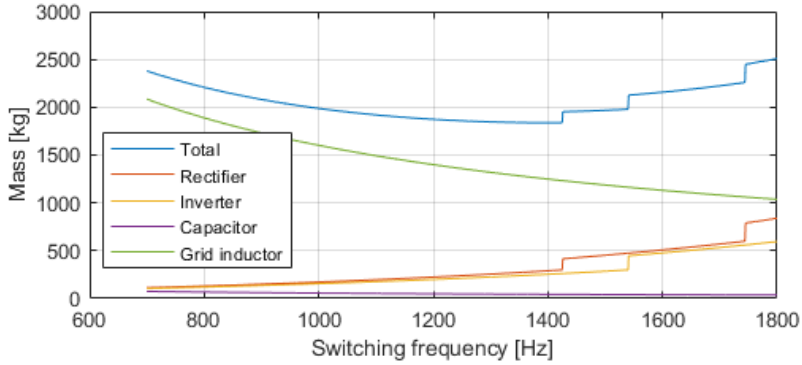

(a) AC cluster

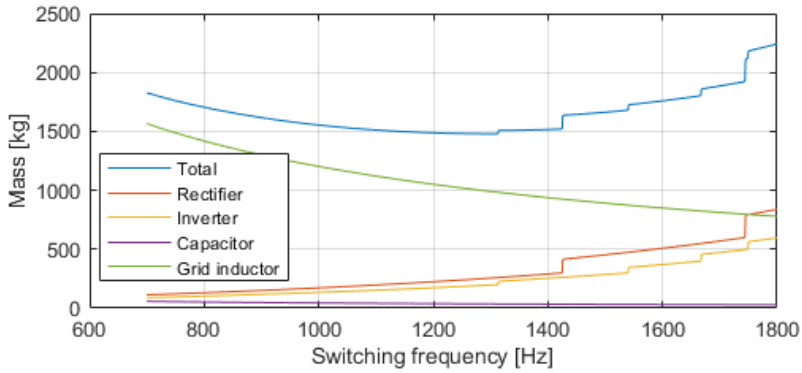

(b) DC cluster

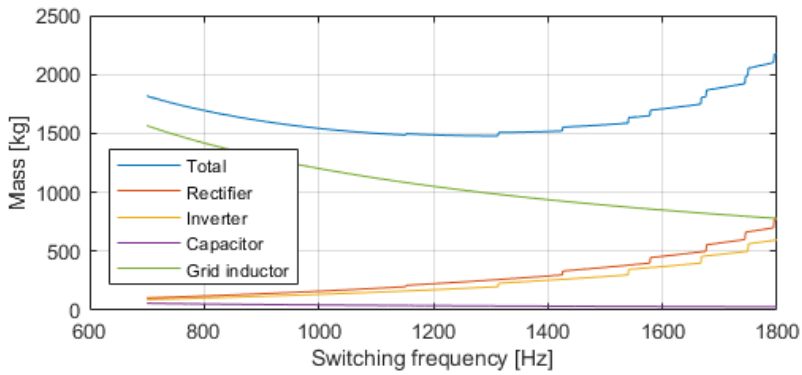

(c) Hybrid cluster

Figure B.3: Mass for the AC, DC and hybrid cluster using SVPWM.

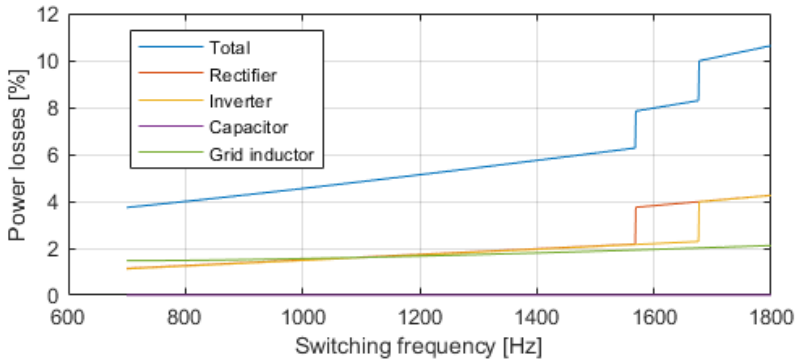

(a) AC cluster

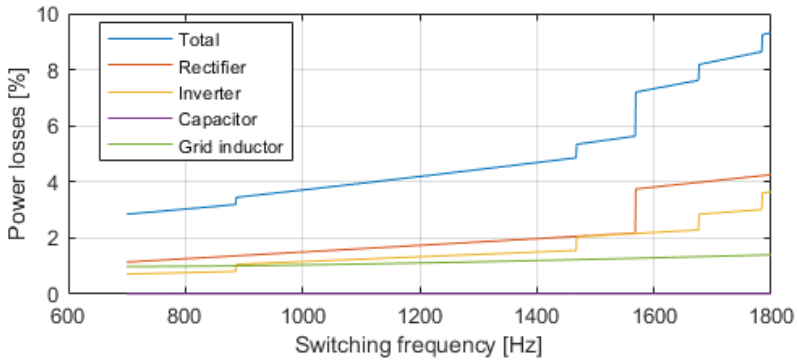

(b) DC cluster

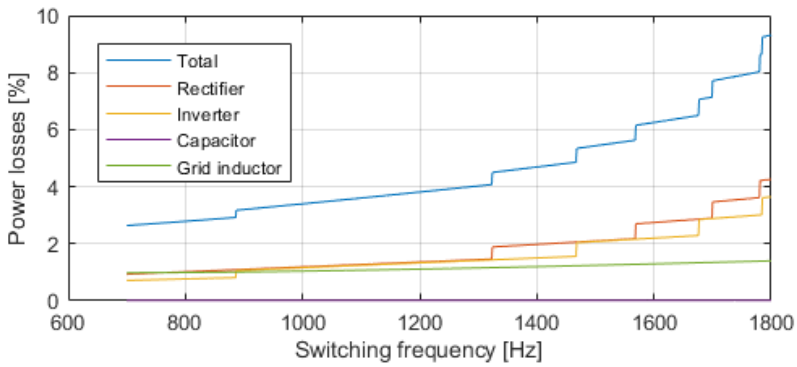

(c) Hybrid cluster

Figure B.4: Power losses for the AC, DC and hybrid cluster using SFTM.

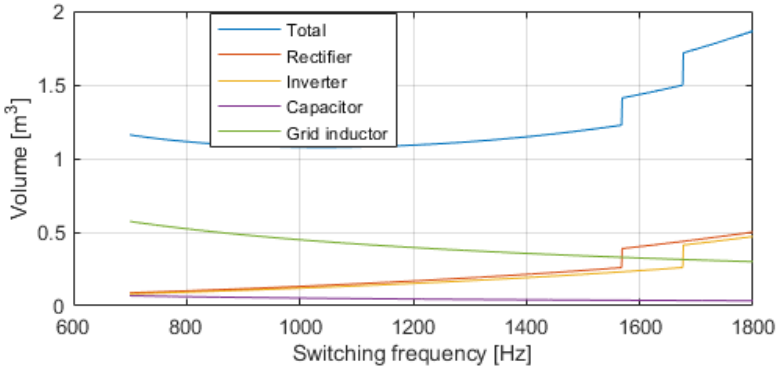

(a) AC cluster

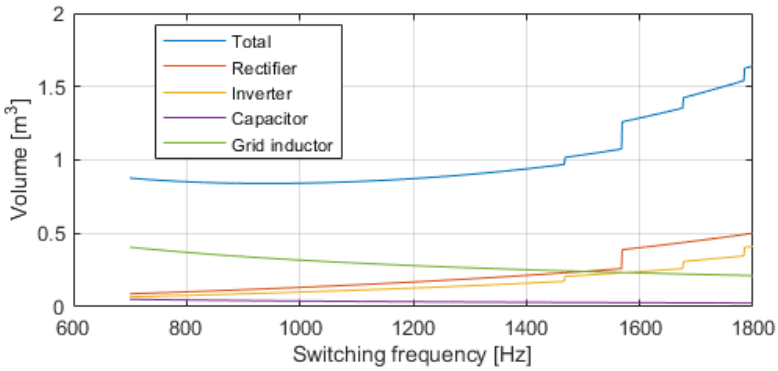

(b) DC cluster

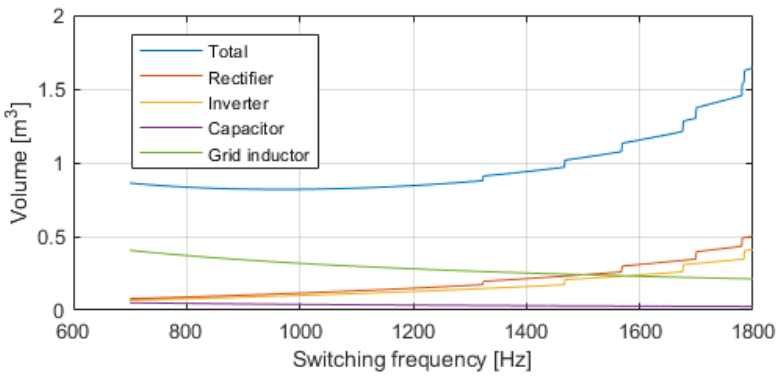

(c) Hybrid cluster

Figure B.5: Volume for the AC, DC and hybrid cluster using SFTM.

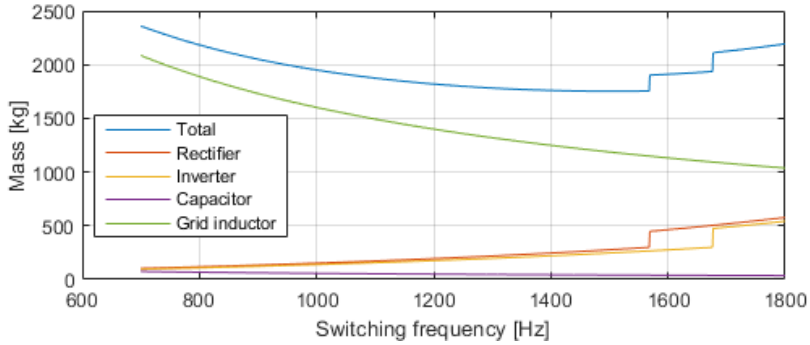

(a) AC cluster

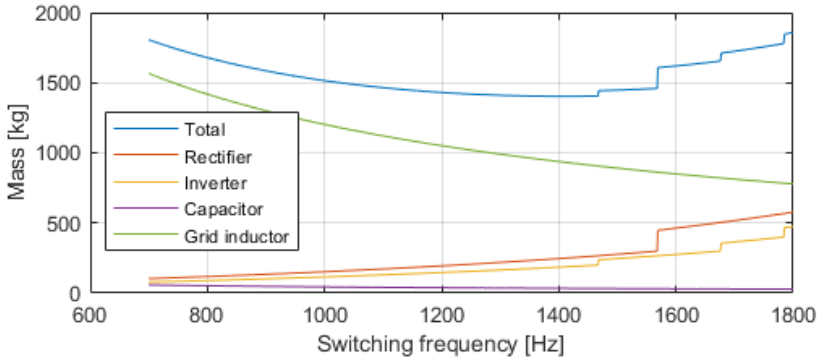

(b) DC cluster

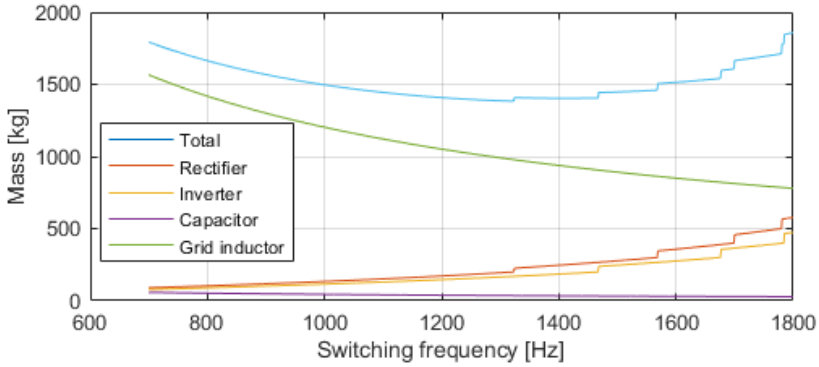

(c) Hybrid cluster

Figure B.6: Mass for the AC, DC and hybrid cluster using SFTM.

Appendix C

Matlab Codes

In this chapter, the Matlab codes developed to obtain the results presented are displayed. In C.1, the main file is displayed. Here, parameters such as number of turbines and nominal machine power can be set. It further calls other function to perform necessary calculations, using loops. This code yields for the AC cluster, using SPWM. To limit the space needed, only this is included here. The other modulation methods and configurations have minor changes.

In C.2 and C.3, the initialisation of the capacitor and inductor used as well as calculations of the relevant parameters are displayed. In C.4, the parameters of the converter together with the cooling system are initialised and calculated.

C.1 AC cluster SPWM

```
%% ==========================================
% Script: Parameters and calculations for the AC cluster using SPWM
% Author: Ingvar Hinderaker Sunde
% Description: Finds and sets the key parameters for one cluster
% ------------------------------------------
clc            %deletes the command window
close all      %closes windows/figures
clear          %clears workspace
% ==========================================
f_sw=700:10:1600;       %switching frequency Hz
n_c=3;                  %number of turbines per cluster
```

```
%% System parameters
V_LLnom = 690;          % nominal RMS line-to-line voltage [V]
P_nom = 444e3;          % nominal power [W]
f = 50;                 % frequency [Hz]
pf = 0.85;              % displacement factor, cos(phi)
M_Snom = 0.99;          % modulation index at nominal operation (0.90-1.00)
T_j = 150;              % junction temperature [C]

Z_b = V_LLnom^2/(P_nom*pf); % Base impedance
K_mod = sqrt(2) / 4;            % modulation correction factor for SPWM
I_a = P_nom/(sqrt(3)*V_LLnom*pf); %nominal current [A]
V_DCnom = V_LLnom/(sqrt(3)*K_mod*M_Snom); %nominal DC voltage [V]

%% Capacitor parameters
% Design parameters:
delta_Vdc=0.02; %ratio of peak-to-peak voltage ripple to DC voltage
k_ovf = 1.15; %over voltage factor for VDC > 1kV
k_ovf = 1.1;  %over voltage factor for V_DC < 1 kV
k_vp = 0.8;   %safety factor for peak voltage
k_vdc = 0.7;  %safety factor for DC voltage
delta_Iin = 0.30 ;%relative input DC-link current ripple
%minimum blocking voltage required:
if delta_Vdc <= 2*(k_vp/k_vdc -1)
    V_blockmin = V_DCnom*k_ovf/k_vdc;
else
    V_blockmin = V_DCnom*k_ovf*(1+delta_Vdc/2)/k_vdc;
end
% Calculated design parameters:
C = P_nom./(V_DCnom^2 *(delta_Vdc + 0.5*delta_Vdc^2)*f_sw); %DC capacitor [F]
I_vscAC_RMS = sqrt( sqrt(6)*K_mod*M_Snom/pi*...
    (1+(4-(3*sqrt(6)*pi*K_mod*M_Snom)/2)*pf^2)*I_a^2); % vsc rms current [A]
I_inAC_RMS = delta_Iin * 3*K_mod*M_Snom*pf*I_a; %rms dc link in-current [A]
```

```
I_C =sqrt(I_vscAC_RMS^2 + I_inAC_RMS^2); %capacitor rms current [A]
capacitor=open('DC_Capacitor.mat'); %Open file for implemented DC capacitor

%% Inductor parameters
delta_iL =0.20; % Max. relative AC current ripple
%Grid side inductance [H]:
L = (1-3/2*K_mod*M_Snom)* V_LLnom^2 * pf./(sqrt(2)*delta_iL *f_sw*P_nom);
I_L = sqrt(1+delta_iL.^2/6)*I_a; % Inductor current [A]
%Machine side inductance: No machine inductor needed, due to machine ind.
inductor=open('3_AC_Inductor.mat'); %Open file for desired AC inductor

%% Semiconductor parameters
k_olf = 0.3; % overload factor!
I_psw=sqrt(2/3)*P_nom*(1+delta_iL/2)*(1+k_olf)/(V_LLnom*pf);%Peak current
semiconductor=open('module_3300V_1500A.mat');%Open desired semicond. module
I_n=1500; %nominal current of one semiconductor, decided from the module [A]
delta_CI=0.225; %current imbalance rate
n_p_min = ((I_psw/(1.6*I_n)-1)*...
    ((1+delta_CI)/(1-delta_CI))+1);%number of parallel connected devices
n_p_inv=ceil(n_p_min); %number for the inverter
n_p_rect=ceil(n_p_min); %number for the rectifier
n_s=1; %number of series connected devices, assumes 1
V_bk=V_blockmin; %blocking voltage of the application [V]

%% Calculation loop
for i = 1:length(f_sw) % repeat for each step in switching frequency
% Function calculating volume,mass and losses for the capacitor:
[V_ol_C(i),M_ass_C(i),P_epsilonC(i),P_omega_C(i)] =...
```

```
    capacitorCalc_struct(capacitor.parameter,V_DCnom,C(i),...
    f_sw(i),delta_Vdc,I_C);

% Calculations of the volume,mass and losses for grid side inductor:
[V_olL(i),M_ass_L(i),P_wL(i),P_coreL(i)] =...
    inductorCalc_struct(inductor.parameters,L(i),I_L,f_sw(i),delta_iL);

% Calculations of the volume, mass and losses for the semiconductor,
% including thermal limit conditions:
         a=1; %loop condition
           nprect(i)=n_p_rect; %store number in vector
           npinv(i)=n_p_inv;  %store number in vector
     while a == 1

    %Functions for the desired parameters from the inverter and rectifier:
    %Inverter:
[P_igbt_inv(i),P_diode_inv(i),R_thHS_inv(i),R_thHSmin,...
    M_ass_valve_inv(i),V_ol_valve_inv(i)]=inverterCalc_struct...
   (semiconductor.module,n_p_inv,n_s,V_bk,f_sw(i),K_mod,M_Snom,pf,I_a,T_j);
    %Rectifier
[P_igbt_rect(i),P_diode_rect(i),R_thHS_rect(i),R_thHSmin,...
   M_ass_valve_rect(i),V_ol_valve_rect(i)]=rectifierCalc_struct...
  (semiconductor.module,n_p_rect,n_s,V_bk,f_sw(i),K_mod,M_Snom,pf,I_a,T_j);

%Conditions to increase the number of parallel connected devices:
%If thermal resistance lower than min. limit, increase n_p
    if ((R_thHS_rect(i) <= R_thHSmin) && (R_thHS_inv(i) <= R_thHSmin))
```

```
        n_p_rect = n_p_rect +1;
        n_p_inv = n_p_inv +1;
    elseif (R_thHS_rect(i) <= R_thHSmin)
          n_p_rect = n_p_rect +1;
     elseif (R_thHS_inv(i) <= R_thHSmin)
          n_p_inv = n_p_inv +1;

      else
          a=0;
    end %end if
     end %end while
%% Total losses, volume and mass
% Losses
P_CDC(i) = n_c*(P_epsilonC(i) + P_omega_C(i)); % total capacitor losses [W]
P_LF(i) = n_c*(P_wL(i) + P_coreL(i)); %total filter inductor losses [W]
P_valve_inv(i) = n_c*n_p_inv*n_s*...
    (P_igbt_inv(i) + P_diode_inv(i)); %total inverter valve losses [W]
P_valve_rect(i) = n_c*n_p_rect*n_s*...
    (P_igbt_rect(i) + P_diode_rect(i)); %totalrectifier valve losses [W]
%Total losses for the system [W]:
P_loss_VSC(i) = 6 * (P_valve_inv(i)+P_valve_rect(i)) + P_LF(i) + P_CDC(i);

% Volume
C_PV = 0.7;        %Volume utilization factor
V_ol_vsc(i) =n_c* (1/C_PV *(6*(V_ol_valve_inv(i)+V_ol_valve_rect(i))...
    + V_olL(i)+V_ol_C(i))); %total system volume [m^3]

%Mass
M_ass_vsc(i) =n_c* (6*(M_ass_valve_inv(i)+M_ass_valve_rect(i)) +...
    M_ass_L(i)+ M_ass_C(i)); %total system mass [kg]
end %end for

%% Optimisation of switching frequency
```

```
% Function providing optimum Lambda, switching frequency
    , eta, rho, gamma
[Y,sw_f,n,p,y] = optfreq(P_nom,P_loss_VSC,M_ass_vsc,
    V_ol_vsc,f_sw,n_c);

eta=((n_c*P_nom)-P_loss_VSC)/(n_c*P_nom) *100; %
    efficiency [%]
rho=1*10^-6*((n_c*P_nom)-P_loss_VSC)./V_ol_vsc; %power
    density [MW/m^3]
gamma=1*10^-3*((n_c*P_nom)-P_loss_VSC)./M_ass_vsc; %
    power-to-mass ratio [MW/t]

%%
```

C.2 Capacitor calculations

```
%% Parameters DC Capacitors TDK MKP-B256xx
clear;
clc;
%Proportionality regression coefficients found by taking
     data from
%reference capacitor technology:
    parameter.K_VC0=2.0734e-5;
    parameter.K_VC1=0.7290;
    parameter.K_VC2=1.3796;
    parameter.K_pC0=1.3428e3;
    parameter.K_pC1=1.0543;
    parameter.K_OmegaC0=4.069e-3;
    parameter.K_OmegaC1=-0.3211;
    parameter.K_OmegaC2=-0.4661;
    parameter.tandelta_0=2*10^-4; %dissipation factor of
        the dielectric (tan(delta_0)) polypropylene

    save('DC_Capacitor.mat')
```

```
function [V_ol_C,M_ass_C,P_epsilonC,P_omega_C] =
    capacitorCalc_struct(parameter,V_CN,C,f_sw,delta_Vdc,
     I_C)
```

```

%% Parameters DC Capacitors TDK MKP-B256xx
% Setting parameters
    K_VC0=parameter.K_VC0;
    K_VC1=parameter.K_VC1;
    K_VC2=parameter.K_VC2;
    K_pC0=parameter.K_pC0;
    K_pC1=parameter.K_pC1;
    K_OmegaC0=parameter.K_OmegaC0;
    K_OmegaC1=parameter.K_OmegaC1;
    K_OmegaC2=parameter.K_OmegaC2;
    tandelta_0=parameter.tandelta_0; %dissipation factor
        of the dielectric (tan(delta_0)) polypropylene
%% Volume and mass
    V_ol_C = K_VC0 * C.^K_VC1 * V_CN^K_VC2; %overall
       capacitor volume [m^3]
    M_ass_C = K_pC0 *V_ol_C.^K_pC1; %capacitor total
       mass [kg]

%% Power losses
    P_epsilonC = sqrt(3)/2 * f_sw .* C*tandelta_0*
       delta_Vdc^2*V_CN^2;
    %total dielectric losses [W]

    R_sC=K_OmegaC0*C.^K_OmegaC1*V_CN^K_OmegaC2; %
       predicted series resistance at maximum hot-spot
       temperature [Ohm];

    P_omega_C = R_sC *I_C^2; %total capacitor resistive
       losses [W]

end
```

C.3 Inductor calculations

```
%% Parameters 3-AC Inductor, copper conductor Siemens
   series 4EUXX
clear;
```

```
clc;
% %proportionality regression coefficients found by taking data from
% reference inductor technology:
    parameters.K_VL0=3.4353e-3;
    parameters.K_VL1=0.6865;
    parameters.K_rhoL0=4129.2244;
    parameters.K_rhoL1=1.0768;
    parameters.K_pw0=9412.0118;
    parameters.K_pw1=0.85361;
    parameters.K_pc0=8242.2998;
    parameters.K_pc1=0.99926;
    parameters.f_Lref = 50; % reference frequency
    parameters.f_L1 =50; %fundamental frequency
    %Steinmetz coefficients, related to the material of the core:
    parameters.alpha_L=1.1;
    parameters.beta_L=2.0;


save('3_AC_Inductor.mat','parameters')
```

```
function [V_ol_C,M_ass_C,P_epsilonC,P_omega_C] = capacitorCalc_struct(parameter,V_CN,C,f_sw,delta_Vdc,I_C)

%% Parameters DC Capacitors TDK MKP-B256xx
% Setting parameters
    K_VC0=parameter.K_VC0;
    K_VC1=parameter.K_VC1;
    K_VC2=parameter.K_VC2;
    K_pC0=parameter.K_pC0;
    K_pC1=parameter.K_pC1;
    K_OmegaC0=parameter.K_OmegaC0;
    K_OmegaC1=parameter.K_OmegaC1;
    K_OmegaC2=parameter.K_OmegaC2;
    tandelta_0=parameter.tandelta_0; %dissipation factor of the dielectric (tan(delta_0)) polypropylene
%% Volume and mass
    V_ol_C = K_VC0 * C.^K_VC1 * V_CN^K_VC2; %overall
```

```
        capacitor volume [m^3]
    M_ass_C = K_pC0 *V_ol_C.^K_pC1; %capacitor total
        mass [kg]

%% Power losses
    P_epsilonC = sqrt(3)/2 * f_sw .* C*tandelta_0*
        delta_Vdc^2*V_CN^2;
    %total dielectric losses [W]

    R_sC=K_OmegaC0*C.^K_OmegaC1*V_CN^K_OmegaC2; %
        predicted series resistance at maximum hot-spot
        temperature [Ohm];

    P_omega_C = R_sC *I_C^2; %total capacitor resistive
        losses [W]

end
```

C.4 Converter calculations

C.4.1 Module parameters

```
%% Parameters 1700Vx3600A IGBT module by Infineon
    FZ3600R17KE3
clear;
clc;
%% General module parameters
parameters.V_ol_mod=0.0010108; %semiconductor module
    volume, found in datasheet m^3
parameters.rho_mod=1483.97; %power module density [kg/m
    ^3]
parameters.N_isxm=3; %number of internal IGBTs/diodes
    per module
parameters.T_max=  125+273; %maximum temperature [K]
parameters.T_amb = 40+273; %ambient temperature [K]
parameters.T_j0 = 125; %fixed reference junction
    temperature [C]
parameters.delta_HS_max = 8; % max allowable ratio
    between module and HS volume
```

```
12
13 module.GenParameters=parameters;
14
15 %% IGBT parameters
16 igbt.R_th_igbt = (6.3+8.7)*10^-3; %thermal resistance,
      junction to heatsink [K/W]
17 % Conduction
18 igbt.R_C0i=0.401*10^-3; %on-state resistance igbt [Ohm]
19 igbt.V_sw00i=0.964; %threshold voltage igbt [V]
20 igbt.alpha_V_sw0i=-0.89*10^-3; %temp coef. of threshold
      voltage igbt [1/C]
21 igbt.alpha_R_Ci=3.47*10^-3; %temp coef. of resistance
      voltage igbt [1/C]
22 % Switching
23 igbt.K_Eon0i=0.158*10^-3; %on-losses igbt [J/V]
24 igbt.K_Eon1i=6.36*10^-8; %on-losses igbt [J/VA]
25 igbt.K_Eon2i=3.44*10^-11; %on-losses igbt  [J/VA^2]
26 igbt.alpha_Eoni=3.10*10^-3; %on-losses igbt [1/C]
27 igbt.K_Eoff0i=0.037*10^-3; %off-losses igbt [J/V]
28 igbt.K_Eoff1i=4.04*10^-7; %off-losses igbt [J/VA]
29 igbt.K_Eoff2i=7.73*10^-12; %off-losses igbt [J/VA^2]
30 igbt.alpha_Eoffi=3.28*10^-3; %off-losses igbt [1/C]
31
32 module.IGBT=igbt;
33
34 %% Diode parameters
35 diode.R_th_diode = (14+19.5)*10^-3; %thermal resistance,
       junction to heatsink [K/W]
36 % Conduction
37 diode.R_C0d=0.249*10^-3; %on-state resistance diode [Ohm
      ]
38 diode.V_sw00d=0.959; %threshold voltage igbt [V]
39 diode.alpha_V_sw0d=-1.36*10^-3; %temp coef. of threshold
       voltage diode [1/C]
40 diode.alpha_R_Cd=2.54*10^-3; %temp coef. of resistance
      voltage diode [1/C]
41 % Swtiching
42 diode.K_Eoff0d=0.328*10^-3; %off-losses diode [J/V]
43 diode.K_Eoff1d=3.34*10^-7;%off-losses diode [J/VA]
44 diode.K_Eoff2d=-2.68*10^-11;%off-losses diode [J/VA^2]
```

```
diode.alpha_Eoffd=4.25*10^-3; %off-losses diode [1/C]

module.Diode=diode;

%% Cooling system parameters
    HS.rho_H_Sal=1366; %heat sink density [kg/m^3]
    HS.rho_fan=769.23; %fan density [kg/m^3]
    HS.K_HS0=9.322*10^-6; %Proportionality coefficient,
        10 m/s [m^3]
    HS.K_HS1=1.4321; %Proportionality coefficient 10 m/s
    HS.K_fan0=0.1992;
    HS.K_fan1=0.7467;
    HS.K_fan2=0.1966e-3; %[m^3]

    module.HeatSink=HS;

%%
save('module_1700V_3600A.mat')
```

```
%% Parameters 3300Vx1500A IGBT module by Infineon
    FZ1500R33HE3
clear;
clc;
%% General module parameters
parameters.V_ol_mod=0.0010108; %semiconductor module
    volume, found in datasheet m^3
parameters.rho_mod=1187.2; %power module density [kg/m
    ^3]
parameters.N_isxm=3; %number of internal IGBTs/diodes
    per module
parameters.T_max= 150+273; %maximum temperature [K]
parameters.T_amb = 40+273; %ambient temperature [K]
parameters.T_j0 = 150; %fixed reference junction
    temperature [C]
parameters.T_j = 150; %Junction temperature [C]
parameters.delta_HS_max = 8; % max allowable ratio
    between module and HS volume

module.GenParameters=parameters;

```

```
%% IGBT parameters
igbt.R_th_igbt = (7.35+10)*10^-3; %thermal resistance, junction to heatsink [K/W]
% Conduction
igbt.R_C0i=1.130*10^-3; %on-state resistance igbt [Ohm]
igbt.V_sw00i=1.436; %threshold voltage igbt [V]
igbt.alpha_V_sw0i=-0.237*10^-3; %temp coef. of threshold voltage igbt [1/C]
igbt.alpha_R_Ci=3.26*10^-3; %temp coef. of resistance voltage igbt [1/C]
% Switching
igbt.K_Eon0i=0.4895*10^-3; %on-losses igbt [J/V]
igbt.K_Eon1i=3.873*10^-8; %on-losses igbt [J/VA]
igbt.K_Eon2i=4.626*10^-10; %on-losses igbt  [J/VA^2]
igbt.alpha_Eoni=2.7586*10^-3; %on-losses igbt [1/C]
igbt.K_Eoff0i=0.116*10^-3; %off-losses igbt [J/V]
igbt.K_Eoff1i=7.31*10^-7; %off-losses igbt [J/VA]
igbt.K_Eoff2i=4.53*10^-11; %off-losses igbt [J/VA^2]
igbt.alpha_Eoffi=2.44*10^-3; %off-losses igbt [1/C]

module.IGBT=igbt;

%% Diode parameters
diode.R_th_diode = (13+11)*10^-3; %thermal resistance, junction to heatsink [K/W]
% Conduction
diode.R_C0d=0.804*10^-3; %on-state resistance diode [Ohm]
diode.V_sw00d=1.359; %threshold voltage igbt [V]
diode.alpha_V_sw0d=-3.19*10^-3; %temp coef. of threshold voltage diode [1/C]
diode.alpha_R_Cd=0.62*10^-3; %temp coef. of resistance voltage diode [1/C]
% Swtiching
diode.K_Eoff0d=0.314*10^-3; %off-losses diode [J/V]
diode.K_Eoff1d=7.28*10^-7;%off-losses diode [J/VA]
diode.K_Eoff2d=-1.35*10^-10;%off-losses diode [J/VA^2]
diode.alpha_Eoffd=5.33*10^-3; %off-losses diode [1/C]

module.Diode=diode;
```

```
%% Cooling system parameters
    HS.rho_H_Sal=1366; %heat sink density [kg/m^3]
    HS.rho_fan=769.23; %fan density [kg/m^3]
    HS.K_HS0=9.322*10^-6; %Proportionality coefficient,
        10 m/s [m^3]
    HS.K_HS1=1.4321; %Proportionality coefficient 10 m/s
    HS.K_fan0=0.1992;
    HS.K_fan1=0.7467;
    HS.K_fan2=0.1966e-3; %[m^3]

    module.HeatSink=HS;

%%
save('module_3300V_1500A.mat')
```

C.4.2 Calculations for the Rectifier

```
function [P_igbt,P_diode,R_thHS,R_thHSmin,M_ass_valve,
    V_ol_valve] = rectifierCalc_struct(module,n_p,n_s,
    V_bk,f_sw,K_mod,M_S,pf,I_a,T_j)

%% Parameters IGBT module
    % Module parameters
    V_ol_mod=module.GenParameters.V_ol_mod; %
        semiconductor module volume, found in datasheet [
        m^3]
    rho_mod=module.GenParameters.rho_mod; %power module
        density [kg/m^3]
    R_th_igbt = module.IGBT.R_th_igbt; %thermal
        resistance, junction to heatsink [K/W]
    R_th_diode = module.Diode.R_th_diode; %thermal
        resistance, junction to heatsink [K/W]
    N_isxm=module.GenParameters.N_isxm; %number of
        internal IGBTs/diodes per module

    % Conduction parameters
    R_C0i=module.IGBT.R_C0i; %on-state resistance igbt [
        Ohm]
```

```
13      R_C0d=module.Diode.R_C0d; %on-state resistance diode
            [Ohm]
14      V_sw00i=module.IGBT.V_sw00i; %threshold voltage igbt
            [V]
15      V_sw00d=module.Diode.V_sw00d; %threshold voltage
            igbt [V]
16      alpha_V_sw0i=module.IGBT.alpha_V_sw0i; %temp coef.
            of threshold voltage igbt [1/C]
17      alpha_V_sw0d=module.Diode.alpha_V_sw0d; %temp coef.
            of threshold voltage diode [1/C]
18      alpha_R_Ci=module.IGBT.alpha_R_Ci; %temp coef. of
            resistance voltage igbt [1/C]
19      alpha_R_Cd=module.Diode.alpha_R_Cd; %temp coef. of
            resistance voltage diode [1/C]
20
21      % Switching parameters
22      K_Eon0i=module.IGBT.K_Eon0i; %on-losses igbt [J/V]
23      K_Eon1i=module.IGBT.K_Eon1i; %on-losses igbt [J/VA]
24      K_Eon2i=module.IGBT.K_Eon2i; %on-losses igbt  [J/VA
            ^2]
25      alpha_Eoni=module.IGBT.alpha_Eoni; %on-losses igbt
            [1/C]
26      K_Eoff0i=module.IGBT.K_Eoff0i; %off-losses igbt [J/V
            ]
27      K_Eoff1i=module.IGBT.K_Eoff1i; %off-losses igbt [J/
            VA]
28      K_Eoff2i=module.IGBT.K_Eoff2i; %off-losses igbt [J/
            VA^2]
29      alpha_Eoffi=module.IGBT.alpha_Eoffi; %off-losses
            igbt [1/C]
30      K_Eoff0d=module.Diode.K_Eoff0d; %off-losses diode [J
            /V]
31      K_Eoff1d=module.Diode.K_Eoff1d;%off-losses diode [J/
            VA]
32      K_Eoff2d=module.Diode.K_Eoff2d;%off-losses diode [J/
            VA^2]
33      alpha_Eoffd=module.Diode.alpha_Eoffd; %off-losses
            diode [1/C]
34
35      % Cooling system parameters
```

```
    rho_H_Sal=module.HeatSink.rho_H_Sal; %heat sink density [kg/m^3]
    rho_fan=module.HeatSink.rho_fan; %fan density [kg/m^3]
    K_HS0=module.HeatSink.K_HS0; %Proportionality coefficient, 10 m/s [m^3]
    K_HS1=module.HeatSink.K_HS1; %Proportionality coefficient, 10 m/s
    K_fan0=module.HeatSink.K_fan0; %Fan constants
    K_fan1=module.HeatSink.K_fan1;
    K_fan2=module.HeatSink.K_fan2; %[m^3]

    % Device temperature and thermal resistance requirements
    T_max= module.GenParameters.T_max; %maximum temperature [K]
    T_amb =module.GenParameters.T_amb; %ambient temperature [K]
    T_j0 = module.GenParameters.T_j0; %fixed reference junction temperature [C]
    delta_HS_max = module.GenParameters.delta_HS_max;
    R_thHSmin = (K_HS0/(delta_HS_max*V_ol_mod))^(1/K_HS1); % minimum allowable thermal resistance [Ohm]
    %% Semicondutor currents
% Conduction current
I_dAVG = (sqrt(2)/(2*pi) + K_mod/2 *M_S*pf)*I_a; %avg igbt current [A]
I_tAVG = (sqrt(2)/(2*pi) - K_mod/2 *M_S*pf)*I_a; %avg diode current [A]
I_dRMS = sqrt((3*pi + 8*M_S*pf)/(12*pi))*I_a; %rms igbt current [A]
I_tRMS = sqrt((1/2 - (I_dRMS/I_a)^2)) * I_a;       %rms diode current [A]

% Swtiching current
I_swaAVG = sqrt(2)/pi * I_a; % avg switching current [A]
I_taAVG = I_swaAVG;          % avg igbt current right after turn-on [A]
I_tbAVG = I_swaAVG;          % avg igbt current right before turn-off [A]
```

```
I_dbAVG = I_swaAVG;          % avg diode current right
    before turn-off [A]
I_swaRMS = 1/sqrt(2) * I_a;  % rms switching current [A]
I_taRMS = I_swaRMS;          % rms igbt current right
    after turn-on [A]
I_tbRMS = I_swaRMS;          % rms igbt current right
    before turn-off [A]
I_dbRMS = I_swaRMS;          % rms diode current right
    before turn-off [A]

%% Power losses
    K_SFT = 0.85; %Safety factor of thermal design
    T_jAVG = T_j*K_SFT; % Average junction temperature[C
        ]
    % Conduction losses calculated parameters
    V_sw0i=V_sw00i*(1+alpha_V_sw0i*(T_j-T_j0));%
        Threshold voltage (T) igbt [V]
    V_sw0d=V_sw00d*(1+alpha_V_sw0d*(T_j-T_j0));%
        Threshold voltage (T) diode [V]
    R_Ci =R_C0i*(1+alpha_R_Ci *(T_j - T_j0)); %on-state
        resistance(T) igbt [Ohm]
    R_Cd =R_C0d*(1+alpha_R_Cd *(T_j - T_j0)); %on-state
        resistance(T) diode [Ohm]

    P_cond_igbt = V_sw0i * I_tAVG./n_p + R_Ci *(I_tRMS./
        n_p).^2; %igbt conduction losses pr module [W]
    P_cond_diode = V_sw0d * I_dAVG./n_p + R_Cd *(I_dRMS
        ./n_p).^2; %diode conduction losses pr module [W]

    % Switching loses calculated Parameters
    E_sw0oni = V_bk/n_s * (K_Eon0i + K_Eon1i * I_taAVG./
        n_p + K_Eon2i*(I_taRMS./n_p).^2);%on switching
        dissipated energy igbt [J]
    E_sw0offi = V_bk/n_s * (K_Eoff0i + K_Eoff1i *
        I_tbAVG./n_p + K_Eoff2i*(I_tbRMS./n_p).^2);%off
        switching dissipated energy igbt [J]
    E_sw0offd = V_bk/n_s * (K_Eoff0d + K_Eoff1d *
        I_dbAVG./n_p + K_Eoff2d*(I_dbRMS./n_p).^2);%off
        switching dissipated energy diode [J]

```

```
    P_sw_on_igbt = f_sw * E_sw0oni*(1+alpha_Eoni*(T_jAVG
        -T_j0)); %igbt on-loss [W]
    P_sw_off_igbt = f_sw * E_sw0offi*(1+alpha_Eoffi*(
        T_jAVG-T_j0)); %igbt off-loss [W]
    P_sw_off_diode = f_sw * E_sw0offd*(1+alpha_Eoffd*(
        T_jAVG-T_j0)); %diode off-loss [W]

    % Total summarised losses
    P_igbt=P_cond_igbt+P_sw_on_igbt+P_sw_off_igbt; %
        Total igbt losses [W]
    P_diode = P_cond_diode + P_sw_off_diode; %Total
        diode losses [W]

    % Thermal resistance requirement
    DeltaT_mod = max(R_th_igbt*P_igbt/N_isxm,R_th_diode*
        P_diode/N_isxm); %[K]
    DeltaT_HS = K_SFT*T_max -DeltaT_mod-T_amb; %maximum
        allowable heatsink to ambient T difference [K]
    R_thHS = DeltaT_HS./(P_igbt+P_diode); %[K/W]

%% Volume and mass
    %Volume
    V_ol_H_Sal=K_HS0 * (1./R_thHS).^K_HS1; %volume of
        alumimun/copper structure [m^3]
    V_ol_fan=K_fan0 * (V_ol_H_Sal-K_fan2).^K_fan1; %fan
        volume [m^3]
    V_ol_HS = V_ol_H_Sal + V_ol_fan; %heat sink volume,
        given by V_ol_HSal and V_ol_fan [m^3]
    delta_HS=V_ol_H_Sal/V_ol_mod; %maximum 8
    %Total mass
    M_ass_valve = n_p * n_s .*(rho_mod * V_ol_mod +
        rho_H_Sal*V_ol_H_Sal +...
    rho_fan * V_ol_fan); % Mass of valve [kg]

    %Total volume
    V_ol_valve = n_p * n_s .* (V_ol_mod + V_ol_HS);%
        Volume of power switch valve [m^3]
end
```

Appendix D

Related work

D.1 Paper for EERA DeepWind'19 - 16th Deep Sea Offshore Wind R&D conference

The following pdf-file is the paper submitted in correlation with the EERA DeepWind'19 - 16th Deep Sea Offshore Wind R&D conference, 16.-18. January 2019, Trondheim, Norway. The paper was reviewed by a scientific comitee and is accepted for publishing. This will be in the *Journal of Physics: Conference series* and expected publication is in the 2nd quarter of 2019.

Power Losses in Electrical Topologies for a Multi-Rotor Wind Turbine System

Ingvar Hinderaker Sunde [1], Raymundo E. Torres-Olguin [2], Olimpo Anaya-Lara [3]

[1] Department of Electric Power Engineering, Norwegian University of Science and Technology, Trondheim, Norway
[2] Department of Energy Systems, SINTEF Energy Research, Trondheim, Norway
[3] University of Strathclyde, Glasgow, United Kingdom

E-mail: `ingvarhs@stud.ntnu.no`

Abstract. Multi-rotor wind turbine systems are proposed as an additional technology to the future of wind energy, and a way of achieving wind turbines generating 20 MW or more. Research regarding the electrical connections of such a system is lacking, and this is key parts of the system. The controllability and power losses are important factors in the different topology options. In this study, three different electrical topologies are proposed and their controllers are implemented respectively. The systems are fairly simplified. Further, ways to measure the power losses within the power converters are researched, and a way of doing so is implemented on the three systems. The simulations performed on the system show the validity of the controllers as well as the power loss calculation method. In this study, the power losses found in the different topologies in total are quite similar to each other, right above 1%, so it is hard to prefer on of the topologies based on this. However, this serves as a tool that can be adjusted and used on more complex systems, and in this way contribute to finding an optimal electrical collector topology for a multi-rotor wind turbine system.

1. Introduction

Wind power is one of the most important energy resources worldwide. In 2017, 55 % of the new installed power capacity was wind power, and the offshore wind energy increased with 101 % [1]. Moreover, it is likely that the cumulative installed wind power will exceed 200 GW by the end of 2020 and, that of this, offshore wind will account for 25% [2].

Together with this increasing cumulative installed capacity, also the turbine sizes are increasing. In 2017, the average installed turbine rating was 2.7 MW for onshore applications, and 5.8 for offshore applications [1], the latter an increase of 39% from the year before [2]. Based on this, the development is expected to continue, which can turn out to be challenging for several reasons [3, 4]. The mechanical stress on the structure will increase with increasing blade size. Mechanical problems are anticipated and installation and maintenance may be more challenging. In addition, the high amount of material needed for the whole structure with these dimensions may be challenging to obtain. The raw materials and rare earth minerals used for production are getting more and more scarce due to the increasing demand [5]. It will also increase the costs, making it difficult to keep reducing the levelized cost of energy (LCOE).

As a suggested solution to this challenge, P. Jamieson proposed the *Multi-Rotor Wind Turbine*-system as a part of the FP7 INNWIND.EU project [6, 7], which consists of several rotors connected all together at the same platform. Such a system can be visualized in Fig. 1. The multi-rotor concept is stated to be beneficial in many ways, in terms of reduced weight in the nacelle and blade, easier installation, transport and maintenance due to smaller components, as well as higher reliability in case of faults, because a fault does not require the whole device to shut down [8]. However, the complexity of the whole system may be extensive and challenging.

In this study, three possible electrical topologies are presented. These are implemented in Simulink, together with a loss calculation method which is also presented here. Further, the results from the simulations are presented and briefly discussed.

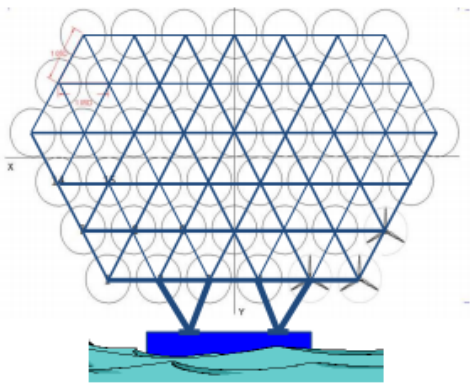

Fig. 1: Model of a multi-rotor wind turbine system, consisting of 45 rotors [6].

2. Proposed Topologies

A theory review of electrical configurations was performed. The published literature regarding offshore wind farm collector systems [9, 10, 11] were used, as this can be considered as similar to a multi-rotor system. Some key differences are however present, such as much shorter interconnected cables and the needlessness for subsea cables.

Some qualitative analysis regarding collector systems for multi-rotor systems were also performed in [3] and [4], confirming the possibility to draw clear parallels between the two offshore and multi-rotor collector systems. [3] and [4], as well as [12], discussed the benefits of

collecting the rotors in clusters, which is are also regarded as beneficial in this study. Three topologies were then selected and are further presented here.

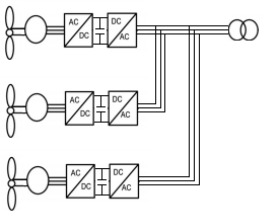

Fig. 2: AC cluster

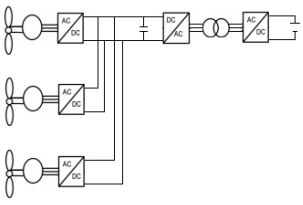

Fig. 3: DC cluster

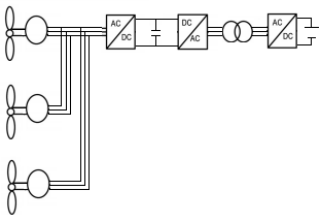

Fig. 4: Hybrid cluster

2.1. AC cluster

The cluster consisting of a back-to-back converter for each turbine is here called the AC cluster. This can be seen in Fig. 2. The back-to-back converters allow individual control of each turbine, making it possible for each of them to operate in the optimal point of operation. Therefore, the machine side converter is controlling the active and reactive power of the turbine, while the grid-side converter is controlling the reactive power and the voltage of the DC link. The implementation and control are based on the model used in [4]. The three turbines present in this specific configuration are connected together in parallel, while in AC, and is meant to represent one cluster of a larger system. The collection is performed at a voltage level of 690 V, so a transformer is needed to further step up the voltage before connecting to other cluster and transmission.

2.2. DC cluster

The cluster consisting of just one AC-to-DC converter for each turbine is here called the DC cluster. This can be seen in Fig. 3. Also here, these converters allow individual control of each turbine, making it possible for each of them to operate in the optimal point of operation, thus it is controlling the active and reactive power. The control implementation of this converter is the same as used for the machine converter in the AC cluster. Further, the three turbines are connected together in parallel, while in DC. This keeps the voltage constant at 690 V. Also a series connection, or a combination could be used. This makes it possible to step up the voltage without the use of a transformer but increases the complexity and requires the use of by-passing techniques.

Further, a DC-to-DC converter is used to step up the voltage. This converter consists of a DC-to-AC converter, a medium-frequency transformer, and an AC-to-DC converter. The first converter uses the same control as the grid side controller in the AC cluster, while the latter is designed with other objectives. An aim is to reduce the size of the needed transformer, so a medium-frequency transformer is desired. Thus, the converter is controlling the frequency as well as the AC voltage, a so-called island mode. The control scheme of this controller can be seen in Fig. 5 After this, other clusters can be connected and further the power can be transmitted.

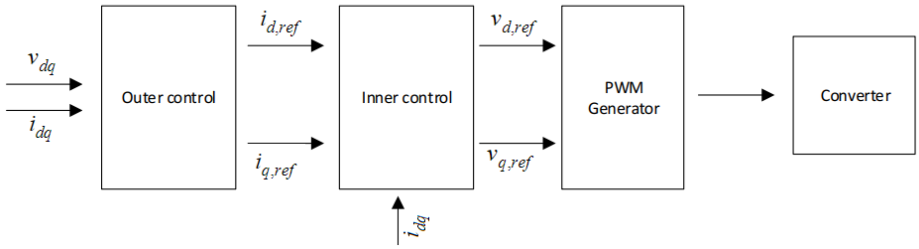

Fig. 5: Overall scheme for AC voltage control

2.3. Hybrid cluster

The cluster consisting of connecting in AC without any individual converters is here called the hybrid cluster. This can be seen in Fig. 4. This is proposed in order to investigate how the reduced number of converters trades off with the reduced control abilities. The first converter, controlling the active and reactive power as in the AC and DC cluster, now needs to control three turbines. Further, the same DC-to-DC converter as in the DC cluster is used, with its same control. The idea is that the wind conditions may not vary too much within the distances these rotors are apart. Then it could be possible to have all the three turbines operate equal, reducing the efficiency, but also the size and weight of the system.

If this can be beneficial may be questionable, but this topology is still included for investigation. As this study is limited to quite simplified systems and stationary conditions, the challenges in this topology will probably not be that visible but will be further analysed in future studies.

3. Power loss calculation

The power converters used in wind power application, consist mostly of IGBTs and diodes, so-called freewheeling diodes, in pairs. Therefore, the total losses are the sum of the losses in the IGBTs and in the diodes are according to

$$P_{loss} = P_{IGBT} + P_{diode} \tag{1}$$

where P_{IGBT} is the power losses in the IGBT and P_{diode} the power losses in the diode. The semiconductor can either be conducting or blocking and has two possible transition states, the turn-on and turn-off. All of these cause power losses which can be found based on the derivations done in [13, 14].

3.1. Conduction losses

The voltage-current characteristics can be linearly approximated, obtaining the on state voltage of the device using the threshold voltage $V_{sw,o,}$ and i_C, the instantaneous current through the on state resistance R_C for the IGBT, yielding

$$v_{sw}(i_C) = V_{sw,o,} + R_C \cdot i_C \tag{2}$$

The same yields for the freewheeling diode, giving

$$v_D(i_D) = V_{D,o,} + R_D \cdot i_D \tag{3}$$

These values can normally be found in the datasheet of a device. As can be seen from typical datasheets for IGBTs and diodes, the on-state diode and collector-emitter voltages, as well as the on-state resistors are dependent on the junction temperature. Normally, datasheets include data for different temperatures, so also these parameters can be found by the help of linear approximations

$$V_{sw,0}(T_j) = V_{sw,00} \cdot (1 + \alpha_{Vsw0} \cdot (T_j - T_{j0})) \tag{4}$$

$$R_C(T_j) = R_{C0} \cdot (1 + \alpha_{R_C} \cdot (T_j - T_{j0})) \tag{5}$$

where α_{Vsw0} and α_{R_C} are the temperature coefficients of the threshold voltage and on-state resistance, $V_{sw,00}$ and R_{C0} are the threshold voltage and on state resistance at a fixed reference junction temperature T_{j0}. Further, the instantaneous values of the power losses for an IGBT can be found to be

$$p_{cond,igbt}(t) = v_{sw}(t) \cdot i_C(t) = V_{sw,o,}(T_j) \cdot i_C(t) + R_C(T_j) \cdot i_C^2(t) \tag{6}$$

which can further can be expressed to find the average losses as

$$P_{cond,igbt} = \frac{1}{T_{sw}} \int_0^{T_{sw}} p_{cond,igbt}(t)dt = V_{swo,0}(T_j) \cdot I_{C,avg} + R_C(T_j) \cdot I_{C,rms}^2 \tag{7}$$

where $I_{C,avg}$ and $I_{C,rms}$ are the average and RMS currents in the IGBT and T_{sw} the time of a switching period. In the diode, the same can be found, hence

$$p_{cond,D}(t) = u_D(t) \cdot i_D(t) = u_{D,o,}(T_j) \cdot i_D(t) + R_D(T_j) \cdot i_D^2(t) \tag{8}$$

$$P_{cond,D} = \frac{1}{T_{sw}} \int_0^{T_{sw}} p_{cond,D}(t)dt = u_{D,o,}(T_j) \cdot I_{D,avg} + R_D(T_j) \cdot I_{D,rms}^2 \tag{9}$$

where the IGBT parameters are replaced with the diode parameters.

3.2. Switching losses

The switching losses are found on the dissipated energy due to the commutation for both turn-on and turn-off. For diodes, the turn-on energy mostly consists of the reverse recovery energy, while the turn-off energy is mostly neglected. However, the IGBTs have significant energy dissipation in both the turn-on and turn-off phases. In general, the switching energy in turn-on can be written as

$$E_{sw,on} = E_{sw0,on} \cdot (1 + \alpha_{Eon} \cdot (T_j - T_{j0})) \tag{10}$$

where α_{Eon} is the temperature coefficient of commutation energy loss at turn on and the term $E_{sw0,on}$ can be found as

$$E_{sw0,on} = v_{swb} \cdot (K_{Eon0} + K_{Eon1} \cdot i_{swa} + K_{Eon2} \cdot i_{swa}^2) \tag{11}$$

where $E_{sw0,on}$ is the commutation energy loss at turn on, v_{swb} is the voltage in the device right before turn on, i_{swa} is the current in the device right after the turn on and $K_{Eon0}, K_{Eon1}, K_{Eon2}$ are polynomial regression coefficients, which can be found from the datasheet of the device. This

energy related to the switching can be turned to power by multiplying the number of switching per second, the switching frequency f_{sw}. The same procedure is followed to find the turn-off losses, and this results in the two equations

$$P_{sw,on} = f_{sw} \cdot E_{sw,on} = f_{sw} E_{sw0,on} \cdot (1 + \alpha_{Eon} \cdot (T_j - T_j 0)) \tag{12}$$

$$P_{sw,off} = f_{sw} \cdot E_{sw,off} = f_{sw} E_{sw0,off} \cdot (1 + \alpha_{Eoff} \cdot (T_j - T_j 0)) \tag{13}$$

where $E_{sw,on}$ and $E_{sw,off}$ are found from equation 11 and the equivalent equation for the turn off for the IGBT respectively. For the diode, $E_{sw,off}$ is neglected, and $E_{sw,on}$ is claimed to consist of mostly the reverse-recovery energy, which is found by

$$E_{sw,on,D} = \frac{1}{4} Q_{rr} U_{Drr} \tag{14}$$

where Q_{rr} represents the recovered charge and U_{Drr} is the voltage across the diode during reverse recovery.

3.3. Total power electronic losses

In total, equations can be set up to show the total losses in both the IGBTs and the diodes. To get the losses for the whole converter, the equations must be multiplied with the number N of IGBTs and diodes in the actual converter. Then the total losses will be

$$P_{IGBT} = N(V_{sw0}(T_j) \cdot I_{C,av} + R_C(T_j) I_{C,rms}^2 + (E_{sw,on} + E_{sw,off}) f_{sw}) \tag{15}$$

$$P_D = N(V_{D,0}(T_j) \cdot I_{D,av} + R_D(T_j) I_{D,rms}^2 + E_{sw,on} f_{sw}) \tag{16}$$

3.4. Implemented loss calculation method

In order to quantify the power losses inside of the converters, the models from [15] were used and modified to fit a two-level converter. This model obtains the signal measurements of both IGBT and diode pair in one half-bridge. These signals are used to specify the voltage and the current in the IGBTs and in the diodes. Further, these signals are divided into loss calculations blocks for the IGBT and diode respectively. A simplification done is using just one IGBT and diode module for each part of the half bridge. Normally in these types of devices, there are several modules connected in series, in order to increase the possible voltage level. The tests are therefore kept within limits where they can operate with just one module.

The IGBT losses are separated into switching and conduction losses. The different losses are found, based on the parameters presented in their respective equations. These values are used to find the dissipated turn-on energy by interpolation with the help of look-up tables. The look-up tables is linked with datasheet of a specified IGBT module, defined in Matlab. From this, the dissipated energy from the switching is found and is transformed into power. For the conduction losses, the loop-up table finds the saturation voltage, which is multiplied with the current to obtain the power losses. The power is further injected into the thermal model which obtains the IGBT temperature.

The same yields for the diode losses. They are separated into conduction and reverse recovery losses. Interpolations based on the parameters presented in the equations are used together with look-up tables. These are linked with the diode specifications from a Matlab file. The reverse recovery energy loss found is converted into power. For the conduction losses, the loop-up table finds the on-state voltage, which is multiplied with the current to obtain the power losses. The power is further injected into the thermal model which obtains the diode temperature

4. Simulation results

Simulations for the different topologies were carried out. Due to the different voltage and current level in the different topologies as well as also within one topology, different IGBT and diode modules needed to be defined in Matlab. From the loss calculation blocks [15], three IGBT and diode-modules had been implemented in Matlab, based on their available datasheets. These were a 600V/150A module [16] from Fuji Electric, a 1700V/800A module [17] from ABB and a 3300V/250A module [18], also from ABB. A combination of these was sufficient to deal with the currents of the different systems but problematic for the voltage level after the step-up transformers. Therefore, another IGBT and diode module was implemented in Matlab, with the help of the datasheet of the module. This was a 6500V/600A module [19] from ABB, their single module with the highest voltage capability.
An important simplification in order to calculate these losses is that just one single IGBT and diode module is used for each switch. Hence in the three-phase bridge with 6 pulses, there are only six of these modules. In reality, multiple modules may be connected in series to increase the voltage level instead of using modules with a very high rating. This may influence the result, but was a necessity for limiting the complexity of the scope of this study.

The losses in the three topologies are presented below.

4.1. AC cluster

Since the turbines are operating equally and ideally, without any dynamic differences, the power losses in the different corresponding converters are equal. Therefore only one of each, the machine side and grid side converter are presented here. The machine side converter losses are presented in Fig. 6 and the grid side converter in Fig. 7.

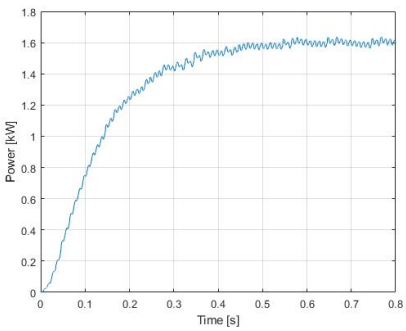

Fig. 6: Machine side losses

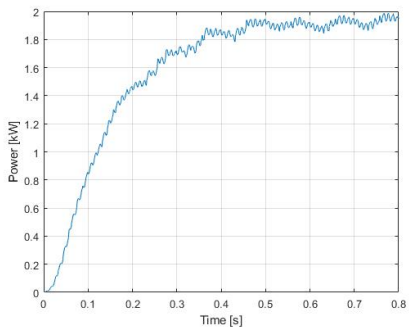

Fig. 7: Grid side converter

The power losses for one machine side converter are found to be stabilising at 1.6 kW, giving the percentage losses of

$$P_{loss[\%]} = \frac{P_{loss}}{P_{in}} \cdot 100\% \approx \frac{1.6\text{kW}}{300\text{kW}} \cdot 100\% = 0.53\% \tag{17}$$

The total losses for one grid side converter are stabilising at 1.9 kW. This gives the percentage losses of

$$P_{loss[\%]} = \frac{P_{loss}}{P_{in}} \cdot 100\% \approx \frac{1.9\text{kW}}{300\text{kW}} \cdot 100\% = 0.64\% \tag{18}$$

4.2. DC cluster

In the three machine side converters, the losses are equal due to their equality. Therefore, only one of the converter losses is presented here, in Fig. 8. The losses in the DC-to-AC and AC-to-DC converters are presented in Fig. 9 and Fig. 10 respectively.

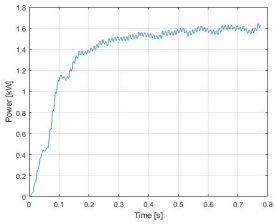

Fig. 8: Machine side converter

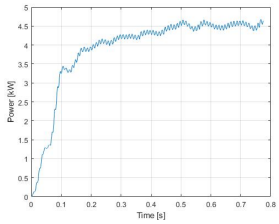

Fig. 9: DC-to-AC converter

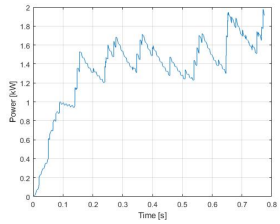

Fig. 10: DC-to-AC converter

The total power losses in one machine side converter are found to be stable at 1.6 kW, giving a percentage of losses of

$$P_{loss[\%]} = \frac{P_{loss}}{P_{in}} \cdot 100\% \approx \frac{1.6\text{kW}}{300\text{kW}} \cdot 100\% = 0.53\% \tag{19}$$

The losses for the DC to AC side are found to be stable at around 4.5 kW, giving the percentage losses of

$$P_{loss[\%]} = \frac{P_{loss}}{P_{in}} \cdot 100\% \approx \frac{4.5\text{kW}}{900\text{kW}} \cdot 100\% = 0.50\% \tag{20}$$

The module information in the 6500V/600A module used in the AC to DC side was implemented without the same precision level as the other three. Therefore, the curve showing the power losses are not as smooth. However, the losses are found to be stable at around 1.8 kW, giving the losses in percentage as

$$P_{loss[\%]} = \frac{P_{loss}}{P_{in}} \cdot 100\% \approx \frac{1.8\text{kW}}{900\text{kW}} \cdot 100\% = 0.20\% \tag{21}$$

The last converter is experiencing very low current due to the step-up transformer. This, as it can be seen, has a big impact on the losses.

4.3. Hybrid cluster

Only one machine side converter is present, consisting of the power from three turbines. Thus the losses for this converter is presented in Fig. 11. The losses in the DC-to-AC and AC-to-DC converters are presented in Fig. 12 and Fig. 13 respectively. The total summarised losses stabilise at about 4.0 kW. This gives the percentage losses of

$$P_{loss[\%]} = \frac{P_{loss}}{P_{in}} \cdot 100\% \approx \frac{4.0\text{kW}}{900\text{kW}} \cdot 100\% = 0.44\% \tag{22}$$

From the first part, the losses are found to be stable at a value of about 4.5 kW, giving the percentage losses of

$$P_{loss[\%]} = \frac{P_{loss}}{P_{in}} \cdot 100\% \approx \frac{4.5\text{kW}}{900\text{kW}} \cdot 100\% = 0.50\% \tag{23}$$

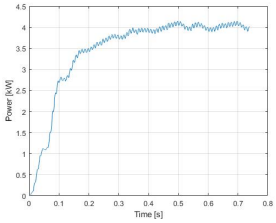

Fig. 11: Machine side converter

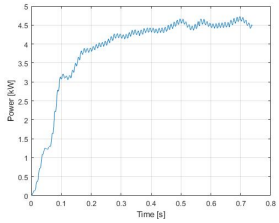

Fig. 12: DC-to-AC converter

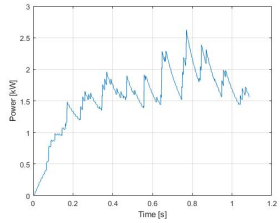

Fig. 13: AC-to-DC converter

The module information in the 6500V/600A module used in the AC to DC side is implemented without the same precision level as the other three. Therefore, also in the curve shown here, the power losses are not as smooth. However, the losses are found to be stable at around 1.9 kW, giving the losses in percentage as

$$P_{loss[\%]} = \frac{P_{loss}}{P_{in}} \cdot 100\% \approx \frac{1.9\text{kW}}{900\text{kW}} \cdot 100\% = 0.21\% \tag{24}$$

Also here, as in the DC cluster, the converter losses are low due to the much lower current after the transformer.

5. Conclusion

From the results, it is observed that the power losses are at a low, and expected level. Summarised, they are also quite similar to each other. The machine and converter losses are similar in each topology, due to their similar output. The high voltage side in the DC-to-DC converter experiences low losses and can be because of low current.

This study excludes the transformer losses. These are expected to increase with frequency [20], so the use of a medium-frequency transformer in the DC-to-DC converter will probably give higher total power losses in the DC cluster and hybrid cluster topologies than the total power losses in the AC cluster, which is using a grid-frequency transformer. However, the trade-off between how much space and weight this may save and how much the losses are increased is of interested and need further investigation. This will be performed in further studies, together with increasing the complexity of the system in terms of the number of rotors, but also by investigating dynamic conditions and varying wind profiles. Then it can be more visible the challenges regarding the control of the different topologies. However, a way of obtaining the power losses within the power converters are obtained and proved to provide meaningful results. This can therefore also be used in future work on this topic, in order to find a suitable topology for the electrical configurations of a multi-rotor wind turbine system.

References

[1] WindEurope, *Wind in power 2017 Annual combined onshore and offshore wind energy statistics*, 2018
[2] WindEurope, *Wind energy in Europe: Outlook to 2020*, 2017
[3] Givaki K *Different Options for Multi-Rotor Wind Turbine Grid Connection*, The 9th International Conference on Power Electronics, Machines and Drives, 2018
[4] Pirrie P, Anaya-Lara O and Campos-Gaona D *Electrical collector topologies for multi-rotor wind turbine systems*, 2018
[5] etipwind.eu, *Strategic Research and Innovation Agenda*, 2018

[6] Jamieson P, et al *Innovative Turbine Concepts Multi-Rotor System* INNWIND.EU, 2015
[7] Jamieson P and Branney M *Multi-Rotors; A Solution to 20 MW and Beyond?*Energy Procedia, Volume 24, 2012, Pages 52-59
[8] Verma P *Multi Rotor Wind Turbine Design And Cost Scaling*, 2014
[9] Lakshmanan P, Liang J and Jenkins N S *Assessment of collection systems for HVDC connected offshore wind farms*, Electric Power Systems Research Volume 129, 2015, Pages 75-82
[10] Quinonez-Varela G, Ault G W, Anaya-Lara O and McDonald J R *Electrical collector system options for large offshore wind farms*IET Renewable Power Generation Volume 1, Issue: 2, 2007, Pages 107 - 114
[11] Srikakulapu R and U V *Electrical Collector Topologies for Offshore Wind Power Plants: A Survey* 2015 IEEE 10th International Conference on Industrial and Information Systems (ICIIS), 2015, page 338-343.
[12] Gksu , Sakamuri J N, Rapp A C, Srensen P E, Sharifabadi K *Cluster Control of Offshore Wind Power Plants Connected to a Common HVDC Station*, Energy Procedia Volume 94, 2016, Pages 232-240
[13] Barrera-Cardenas R A *Meta-parametrised meta-modelling approach for optimal design of power electronics conversion systems: Application to offshore wind energy* Doctoral thesis, 2015
[14] Graovac D and Prschel M *IGBT Power Losses Calculation Using the Data-Sheet Parameters*, 2009
[15] Mathworks *Loss Calculation in a 3-Phase 3-Level Inverter Using SimPower-Systems and Simscape* `https://www.mathworks.com/help/physmod/sps/examples/loss-calculation-in-a-three-phase-3-level-inverter.html`
[16] Fuji Electric *Datasheet:IGBT Module U-Series 600V/150A 2 in one-package 2MBI150U2A-060*
[17] ABB *Datasheet: ABB HiPak IGBT Module 1700V/800A 5SNE 0800M170100*
[18] ABB *Datasheet: ABB HiPak IGBT Module 3300V/250A 5SNG 0250P330305*
[19] ABB *Datasheet: ABB HiPak IGBT Module 6500V/600A 5SNG 0250P330305*
[20] Meier S, Kjellqvist T, Norrga S and Nee H P *Design Considerations for Medium-Frequency Power Transformers in Offshore Wind Farms*, 2009 13th European Conference on Power Electronics and Applications, 2009, pages 1-12

D.2 Poster for DeepWind'19 - 16th Deep Sea Offshore Wind R&D conference

The following pdf-file is the poster presented in correlation with the EERA DeepWind'19 - 16th Deep Sea Offshore Wind R&D conference, 16.-18. January 2019, Trondheim, Norway.

EERA DeepWind'19, Trondheim, 16.-18. January 2019

Electrical Collector Topologies for Multi-Rotor Wind Turbine Systems

Power Loss Calculations

Ingvar Hinderaker Sunde[1], Raymundo E. Torres-Olguin[2], Olimpo Anaya-Lara[3]

[1]Department of Electric Power Engineering, Norwegian University of Science and Technology (NTNU), Trondheim, Norway. E-mail: ingvarhs@stud.ntnu.no
[2]Department of Energy Systems, SINTEF Energy Research, Trondheim, Norway
[3]University of Strathclyde, Strathclyde, United Kingdom

Introduction

- Increasing demand for new innovations in the wind power industry
- P. Jamieson proposed the Multi.-Rotor Wind Turbine System (MRWTS) [1]
- Vestas has already installed a 4-rotor system in Denmark [2]

Objectives:

- Propose different electrical collector topologies for a MRWTS
- Develop appropriate control systems
- Develop a way of calculating power electronic losses

Vestas 4-rotor demonstrator turbine. Source: Vestas (www.vestas.com)

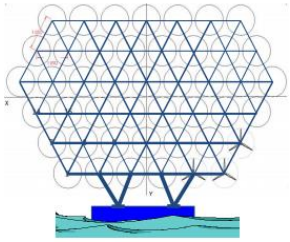

Proposed MRWTS in the FP7 INNWIND.EU project. Source: Innwind (www.innwind.eu)

Methodology

- Perform a literature search in order to propose three different collector topologies
- Implement the topologies in Matlab/Simulink
- Implement controllers for the power converters used in the topologies
- Perform a literature search on power losses in power converters and implement a way of calculating power losses in Simulink
- Perform simulations and make comparisons of the topologies

Proposed topologies

Design considerations:

- Limit number of heavy transformers/power electronics
- Remain stable operation in case of fault in one rotor
- Compromise between controllability, efficiency and costs
- Be scalable, in terms of reaching 20 MW or more

AC Cluster

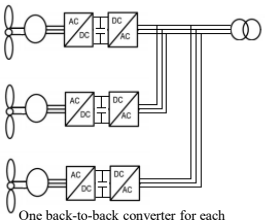

- One back-to-back converter for each turbine
- Allows individual optimised operating point
- High number of power electronics and large AC transformers

DC Cluster

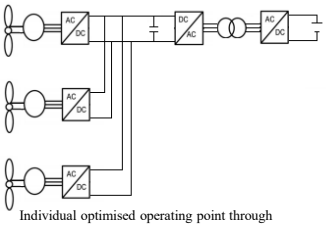

- Individual optimised operating point through individual converters
- DC-to-DC converter using medium frequency power converters may save space and weight
- High power DC-to-DC converters still not commercially available

Hybrid Cluster

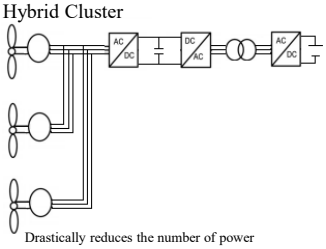

- Drastically reduces the number of power converters needed
- Issues regarding the controllability, one converter must control several turbines
- High power DC-to-DC converters needed

Control

Machine side controller:

- Control active and reactive power
- Compares measured power to reference values
- PI controller in inner and outer loop

Grid side controller:

- Control DC link voltage
- Compare measured DC voltage to reference values
- PI controller in inner and outer loop

AC voltage and frequency controller:

- Frequency controlled through customised PLL
- PI controller in inner and outer loop

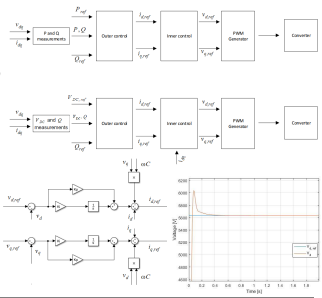

Loss calculation

Power electronic losses found by [3]:

Conduction losses / Switching/ Reverse recovery losses

- IGBT losses $P_{IGBT} = N\left(V_{sw0}(T_j)\cdot I_{C,av} + R_C(T_j)I_{C,rms}^2\right) + \left(E_{sw,on} + E_{sw,off}\right)f_{sw}$
- Diode losses $P_D = N\left(V_{D,0}(T_j)\cdot I_{D,av} + R_D(T_j)I_{D,rms}^2\right) + E_{sw,on}f_{sw}$

Simulink loss calculation method [4]:

1. Define IGBT/Diode module specifications in Matlab from datasheet
2. Obtain current and voltage measurement from the Simulink module
3. Divide signals in to IGBT and diode power loss calculation blocks
4. Compute desired energy or voltage Based on current and voltages, and the temperature in the devide
5. Convert energy to power
6. Input power to the thermal model to obtain the temperature in the device

Simulation results

AC Cluster

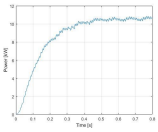

Power converter losses of 1.22 %

DC Cluster

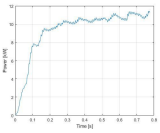

Power converter losses of 1.23 %

Hybrid Cluster

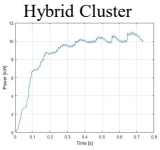

Power converter losses of 1.14 %

Conclusion and future work

Conclusion

- Similar results at a reasonable level
- Controllers work
- Power loss calculation method works
- Higher complexity needed to favour a topology

Future work

- Increase complexity in terms of number of turbines
- Develop controllers for dynamic conditions
- Investigate the use of medium frequency transformers

References

[1] P. Jamieson, et.al., (20015) , INNWIND.EU, Innovative Turbine Concepts – Multi-Rotor System
[2] Vestas Wind Systems A/S, (2016)), News release, Vestas challenges scaling rules with multi-rotor concept demonstration turbine
[3] R.A. Barrera-Cardenas, (2015), Doctoral thesis, Meta-parametrised meta-modelling approach for optimal design of power electronics conversion systems: Application to offshore wind energy
[4] Mathworks, Loss Calculation in a 3-Phase 3-Level Inverter Using SimPowerSystems and Simscape, https://www.mathworks.com/help/physmod/sps/examples/loss-calculation-in-a-three-phase-3-level-inverter.html

NTNU
Norwegian University of Science and Technology

Ingvar Hinderaker Sunde

Design and Optimisation of Electrical Collectors for a Multi-Rotor Wind Turbine System

NTNU

Kunnskap for en bedre verden